UNIVERSITÀ
DEGLI STUDI
FIRENZE

SCUOLA DI SCIENZE
MATEMATICHE
FISICHE E NATURALI
Corso di Laurea Magistrale in
Scienze Fisiche e Astrofisiche

Towards the production of ultracold mixtures of Lithium and Chromium atoms

Verso la produzione di miscele ultrafredde di atomi di Litio e Cromo

Advisor
Dr. Matteo Zaccanti

Co-Advisor
Prof. Marco Fattori

Candidate
Irene Goti

Academic Year 2018/2019

Contents

Introduction **1**

1 Laser cooling and trapping: basic principles **5**
1.1 Lithium 6
1.2 Chromium 8
1.3 Principles of laser cooling 9
1.3.1 Optical molasses 11
1.3.2 Zeeman slower 12
1.4 Magneto-optical trap 14
1.5 Sub-Doppler cooling 16
1.5.1 Gray molasses 17
1.5.2 Optical dipole trap 20
1.5.3 Evaporative and sympathetic cooling 22

2 Compensation coils setup: design, test and applications **25**
2.1 Realization and implementation 26
2.2 Calibration of the coils on the Li cloud 30
2.3 Simulation of optical dipole potential and gravitational sag 34
2.3.1 Optical dipole potential 34
2.3.2 Gravitational sag 36

3 Lithium cooling: MOT and D_1 gray molasses **41**
3.1 Optical setup 42
3.2 Experimental routine and results of MOT and CMOT stages 45
3.2.1 Absorption imaging 45
3.2.2 MOT and compressed MOT 47
3.3 D_1 gray molasses 49
3.3.1 Experimental results 51
3.3.2 Optimization of D_1 cooling with compensation coils 53

4 Chromium MOT and simultaneous loading of double-species ^{6}Li-^{52}Cr MOT **57**
4.1 Experimental setup 58
4.2 Experimental results 60
4.2.1 Characterization of Cr metastable state $|D_3\rangle$ and $|D_4\rangle$ 61
4.2.2 Simultaneous loading of ^{6}Li and ^{52}Cr MOT 64

5 Compensation of thermal lensing effects in the optical trapping setup **69**
5.1 Theory of thermal lensing 70
5.2 Source of thermal lensing in optical setup 72
5.3 Compensation of the thermal lensing effect 74
5.3.1 Thermal lensing on atoms 78

Conclusions **81**

Bibliography **83**

Introduction

My Master thesis work has been carried out at the Department of Physics of the University of Florence under the supervision of Dr. Matteo Zaccanti within the PoLiChroM lab.
The first ambitious goal for our research group is the realization of a new apparatus allowing the production of the first ultracold Fermi-Fermi mixture of ^{6}Li and ^{53}Cr atoms worldwide.
The study of interacting ultracold Fermi gases is of great interest with respect to both few- and many-body phenomena: low particle densities and simple contact interactions make such systems exquisite platforms for quantum simulation experiments [1, 2]. With these prospects, during the last twenty years this research field has experienced an impressive progress, both from the theoretical and experimental point of view. The continuous improvement of laser cooling and trapping techniques, together with the development of ultra-sensitive spectroscopic methods, allow to realize quantum gases samples and to monitor their properties with unprecedented precision. Moreover, the availability of magnetic Feshbach resonances enables to tune inter-particle interactions, thereby opening the way to explore a variety of regimes of quantum matter, such as superfluity (for attractive interactions) and magnetism (for repulsive ones).
In this context, a new appealing scenario is represented by two-component Fermi mixtures of different atomic species. Indeed, the mass-imbalance combined with resonant interactions is expected to enable the access to elusive and exotic many-body phases, unattainable with equal mass systems.
Among few other possibilities, the choice of ^{53}Cr and ^{6}Li is motivated by their specific mass ratio of about $M/m = 8.8$, predicted to feature very peculiar few-body properties. On the one hand, in the strong coupling regime, recent studies predict the existence of weakly-bound or quasi-bound three- and four-body cluster states [3, 4], which are expected to be collisionally stable. On the other hand, the presence of such trimer states, thanks to a pure quantum interference phenomenon, is predicted to fundamentally suppress inelastic losses in the regime of strong Cr-Li repulsion [5]: this makes the Cr-Li system an ideal candidate for the experimental investigation of the phenomenon of itinerant ferromagnetism [6].

At the beginning of my thesis work, the experimental apparatus for the realization of the ultracold Li-Cr mixtures was already devised and its construction almost completed.
During my thesis work I participated in the implementation of new parts of the PoLiChroM machine: the setup of a high-power optical dipole trap (ODT) free from thermal lensing effects, and the whole set of compensation coils and relative control electronics. Moreover, I took part in the optimization of the Li gray molasses stage operating on the D_1 line, and in the characterization of the bosonic ^{52}Cr cloud, both in absence and presence of the ^{6}Li atoms.
This thesis is organized as it follows:

- Chapter 1 briefly recalls the main laser trapping and cooling techniques, especially focusing on those employed for the production of cold Li-Cr mixtures. After a schematic overview of the whole experimental routine, the major properties of the Li and Cr atoms are discussed. Then, I briefly explain from a theoretical point of view the main laser cooling and trapping techniques implemented in our laboratory. In particular, I describe the working principles of the Zeeman slower (ZS), the Magneto-optical trap (MOT), the gray molasses and the optical dipole trap (ODT).

- Chapter 2 reports the design and the realization of a compensation coils setup, and the experimental characterization of the effects arising from the application of a magnetic field on the atoms. First, the main design parameters of the coils and their electronic control are described. Then, I discuss the results of the calibration of the produced magnetic fields. In the second part of the chapter I present a simulation of a bichromatic optical potential experienced by Li and Cr atoms. In particular, I focus on the gravitational sag effect experienced by the two species and discuss how a magnetic field gradient can be employed to balance it.

- In Chapter 3 I discuss the experimental routine and the results attained for what concerns the Lithium laser cooling stages. After a description of the optical setup devised and of the routine strategies, I report the results provided by the application of the MOT and the compressed MOT stages. The chapter also presents the characterization of the gray molasses operating on the D_1 atomic line, and the optimization of this process by means of the compensation coils.

- Chapter 4 presents the characterization of the cold cloud of ^{52}Cr. Here I briefly describe the optical setup employed to produce a MOT, which was already implemented at the start of my thesis. I therefore report the main

results and the analysis of the lifetime of the metastable D states. This characterization has been carried out both for the single species Cr MOT and for the double-species ^{6}Li-^{52}Cr MOT.

- Chapter 5 is dedicated to the implementation of a high power optical dipole trap in our apparatus and in particular to the strategy we devised in order to cancel thermal lensing effects (TL). Thermal lensing is first theoretically described. Then I discuss how its effects can be experimentally observed and quantified. In particular, in this chapter I report the characterization of the TL associated to the optical components employed within the ODT setup. Finally, a strategy to cancel TL is presented and tested by monitoring a small sample of cold Li atoms captured in the trapping beam. The outcome of this investigation is summarized in a work recently published on Optic Express [7].

Chapter 1

Laser cooling and trapping: basic principles

In this chapter I provide a theoretical overview of the cooling and trapping techniques that allow to realize a degenerate Fermi-Fermi mixture of Lithium and Chromium atoms.
In the case of fermions, the degenerate regime is reached when the particles are cooled below their Fermi temperature T_F. This corresponds to the condition $n\lambda^3_{dB} > 1$, where λ_{dB} is the thermal de Broglie wavelength ($\lambda_{dB} \propto T^{-1/2}$) and n is the particle density. By considering an experimentally attainable maximum density of about 10^{14} cm^{-3}, temperatures of less than $100nK$ are needed to reach quantum degeneracy.
In order to achieve this ultracold regime, Li and Cr atoms are initially laser cooled and trapped independently and, only afterwards, they are mixed and further cooled within an optical dipole trap (ODT).
While laser cooling and trapping techniques are well established and relatively easily implementable for Li atoms, the very rich electronic structure of Cr atoms requires a more challenging optical scheme, especially when the fermionic isotope (^{53}Cr) is concerned.
Our experiments are performed with atomic species that are found in nature in solid state at room temperature, hence an oven to sublimate the metals is required. Once heated and brought to the gaseous state, atoms are in a thermal state and they are cooled and trapped by the cooperative action of laser lights and magnetic fields. A schematic view of the whole cooling process is given in Fig. 1.1.
Both Lithium and Chromium atoms are first decelerated by means of a Zeeman slower (ZS) technique and then they are cooled and collected in the science chamber through a magneto-optical trap (MOT). Lithium atoms are further cooled below sub-Doppler temperatures through a gray optical molasses based on the D_1

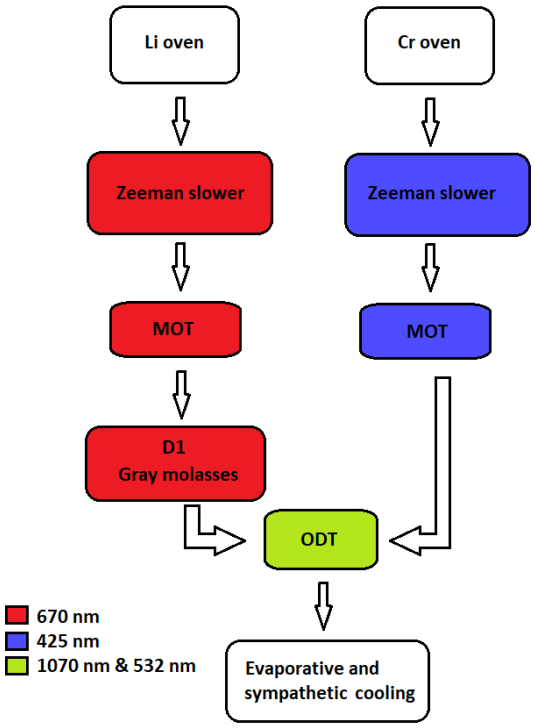

Figure 1.1: *Scheme for the realization of a Cr-Li mixture in the degenerative regime.*

atomic line. At this point Cr and Li are simultaneously trapped in a bichromatic ODT where the degenerate regime is accomplished by means of evaporative and sympathetic cooling techniques.
This chapter is organized as follows. In Section 1.1 and 1.2, I introduce the spectroscopic properties of the Li and Cr isotopes considered in this work: the fermionic isotope ^{6}Li and the bosonic and fermionic Cr isotopes, ^{52}Cr and ^{53}Cr respectively. After that, a brief description of the laser cooling principle is provided (Sec. 1.3) focusing on two major applications, i.e. optical molasses (1.3.1) and the Zeeman slower technique (1.3.2). In Section 1.4 the MOT operating principle is described, Section 1.5 is dedicated on sub-Doppler mechanism, in particular gray molasses (1.5.1), optical dipole trap (1.5.2) and evaporative and sympathetic cooling processes (1.5.3).

1.1 Lithium

Lithium presents, in nature, two stable isotopes, ^{6}Li and ^{7}Li, with abundance of 7.6% and 92.4% respectively. Lithium is the lightest alkali element, so it has only one electron in the external open shell and its electronic spin is $|\vec{S}| = 1/2$. Thus, having ^{6}Li (^{7}Li) a total nuclear spin value of $|\vec{I}| = 1(1/2)$ [8], this isotope

has a semi-integer (integer) total spin, given by $|\vec{I}| + |\vec{S}|$, that is associated with a fermionic (bosonic) character.

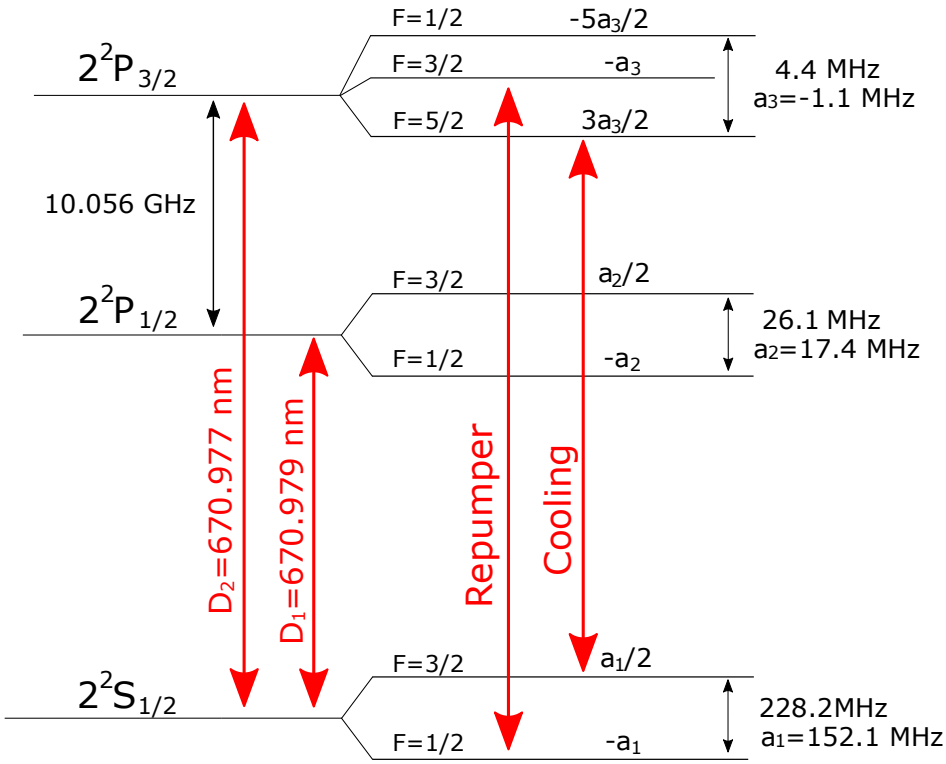

Figure 1.2: *Lithium transitions scheme, adapted from [8], not to scale: fine (left) and hyperfine (right) levels. The D_1 and D_2 lines and the cooling and repumper transition, the meaning of which will be clarified in the following sections (1.4), are marked in red.*

In our experiment we are interested in cooling and trapping the ^{6}Li isotope, whose level scheme is reported in Fig. 1.2: on the left side it is shown the fine structure, associated with different $\vec{J} = \vec{L} + \vec{S}$ values, where $\vec{L}$ is the electron angular momentum. Additionally, the non zero nuclear spin yields a hyperfine structure (shown on the right side in Fig. 1.2) with different energy levels classified according to their total momentum $\vec{F} = \vec{J} + \vec{I}$.
The transition exploited for the initial cooling stage is the so-called D_2 line, from $^2S_{1/2}$ to $^2P_{3/2}$ characterized by a wavelength of $\lambda = 670.977nm$ and a natural width $\Gamma = 2\pi \times 5.87MHz$. In particular, the main transition of interest for the ZS and the MOT stages is $|F = 3/2\rangle \rightarrow |F' = 5/2\rangle$. The importance of an additional repumper light (red marked in Fig 1.2) will be better explained in Section 1.4.

1.2 Chromium

The Chromium has four stable isotopes: ^{50}Cr, ^{52}Cr, ^{53}Cr and ^{54}Cr. In our experiment we are mainly interested in the bosonic ^{52}Cr and fermionic ^{53}Cr isotopes, that are found in nature with abundance of 83.8% and 9.5%, respectively. The atomic level structure of these two isotopes is shown in Fig. 1.3.

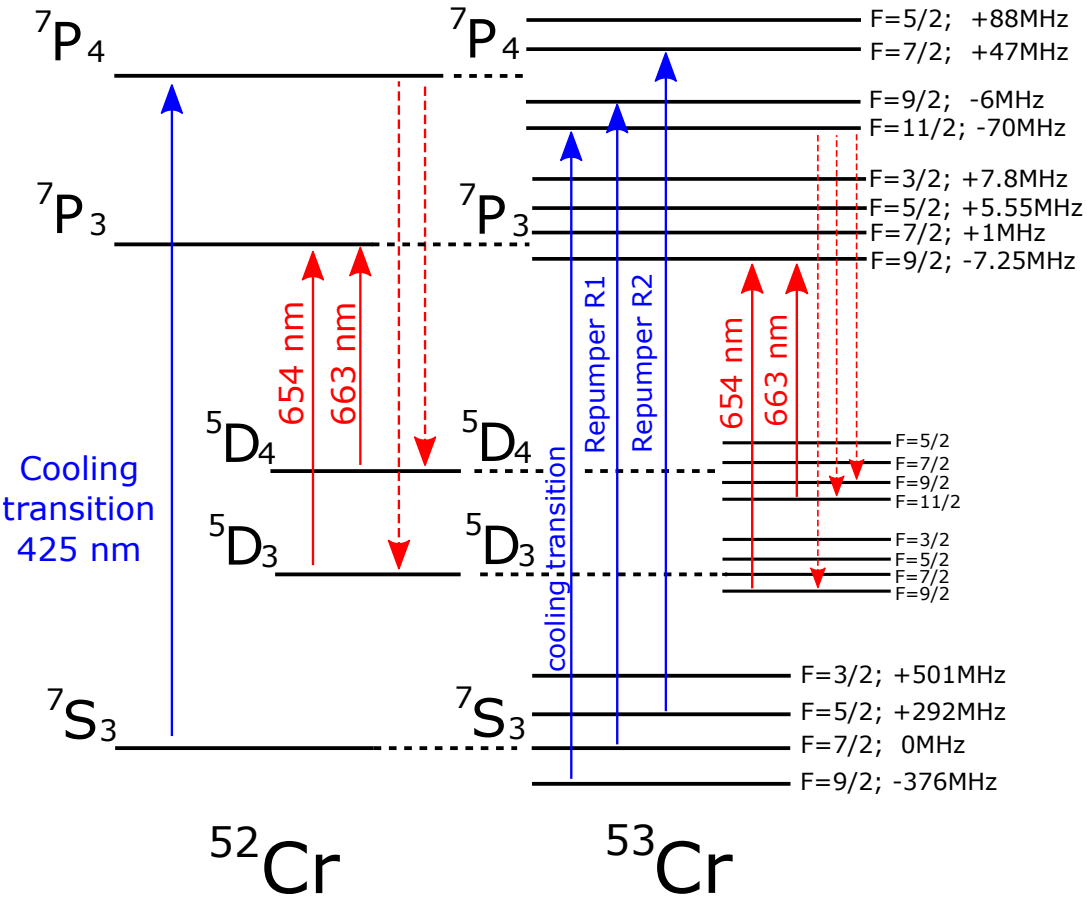

Figure 1.3: *Schematic sketch, not to scale, of the atomic levels structure of bosonic ^{52}Cr (left) and fermionic ^{53}Cr (right).*

Chromium is a transition metal with electron configuration [Ar]3d^{5}4s^1, which leads to a total electron spin $|\vec{S}| = 3$ [9]. For this reason ^{52}Cr, having total nuclear spin $|\vec{I}| = 0$ is a boson, while ^{53}Cr, that has $|\vec{I}| = 3/2$, is a fermion. Similarly to the ^6Li case described above, the non zero nuclear spin of the fermion leads to a hyperfine splitting of the energy levels: each fine state is spit into four hyperfine states. The transition used for the cooling process is ^{7}S$_3 \rightarrow {}^7$P$_4$ at $\lambda = 425.5nm$ for both ^{52}Cr and ^{53}Cr, in particular for the fermionic isotope the specific hyperfine cooling transition is $|F = 9/2\rangle \rightarrow |F' = 11/2\rangle$. This transition has a natural linewidth $\Gamma = 2\pi \times 5.06MHz$, comparable with the D_2 line of Lithium.

As shown in Figure 1.3, the hyperfine splitting is less than 1 GHz in the ground state, and less than 200 MHz in the excited state. On one hand this small splitting, combined with an appropriate tuning in frequency by means of acusto-optic modulators (AOM), allows to exploit the same laser sources for cooling both isotopes. On the other hand, it requires at least two additional blue repumpers to make the MOT stage working, owing to a non-zero probability to populate excited hyperfine states during the cooling cycle.
In addition to the usual transitions exploited within a MOT (marked by the blue arrows in Fig. 1.3), it is important to note the presence of red repumper lights (marked in red). Indeed, atoms from the $^7P_4$ state can spontaneously decay in the metastable states $^5D_4$ and $^5D_3$ that feature a very small decay rate γ_D of about 42 s^{-1} and 127 s^{-1} respectively. Hence, two other separate laser sources at about 663 and 654 nm are needed to repump them back into the cooling cycle.

1.3 Principles of laser cooling

The temperature of an atomic gas is directly related to the spread in the particle velocities[1]. Here I briefly recall how to cool an atomic cloud by means of an optical control of the atomic motion. Laser cooling and trapping rely on the interaction between the laser light and the atoms, in particular they are based on the fact that the absorption and emission processes alters the velocity of the atoms.
By following the description given in [10] and without going into detail, through a semiclassical approach of the interaction of a light field with a two-level atom is possible to derive the optical force experienced by the atom. By considering a monochromatic field described by

$$\vec{E}(\vec{r},t) = E_0(\vec{r})cos(\omega_L t + \phi(\vec{r}))\hat{e} \tag{1.1}$$

and deriving the stationary solution of the optical Bloch equations[2] (U_{st} and V_{st}), after averaging in time, we find that the atom experiences the force:

$$\vec{F} = -\frac{\hbar}{2}\vec{\nabla}\Omega(\vec{r})U_{st} - \frac{\hbar\Omega}{2}\vec{\nabla}\phi(\vec{r})V_{st} \tag{1.2}$$

where $\Omega(\vec{r}) = \sqrt{\left(\frac{(-e\vec{r})\cdot\vec{E}(\vec{r})}{\hbar}\right)^2 + \delta^2}$ is the generalized Rabi frequency and $\delta = \omega_L - \omega_A$ is the detuning between the laser frequency and the resonant atomic frequency ω_A.
While the first term in Eq. 1.2 is related to absorption and stimulated emission

[1] An atomic gas in thermodynamic equilibrium has a velocity distribution described by a Maxwell-Boltzmann curve, whose width determines the gas temperature.
[2] Calculated assuming the formalism of the density matrix [10].

processes and leads to the conservative dipole force (more details in Sec. 1.5.2), the second produces the radiation pressure and it is connected to spontaneous emission processes. Additionally, from the explicit expression of U_{st} and V_{st} (Appendix A of [11])

$$U_{st} = \frac{\Omega\delta}{\delta^2 + \Gamma^2/4 + \Omega^2/2} = \frac{2\delta}{\Omega}\frac{s}{1+s} \tag{1.3a}$$

$$V_{st} = \frac{\Omega\Gamma/2}{\delta^2 + \Gamma^2/4 + \Omega^2/2} = \frac{\Gamma}{\Omega}\frac{s}{1+s} \tag{1.3b}$$

one can deduce that the dipole force dominates for big detuning $|\delta| \gg \Gamma$ (decreasing as $1/\delta$) whereas the radiative pressure is relevant for small detuning (where U_{st} goes to zero) and decreases rapidly (as $1/\delta^2$) if the detuning increases. For convenience, the expression for U_{st} and V_{st} in Eq. 1.3a and 1.3b are given also in terms of the saturation parameter $s = \frac{\Omega^2/2}{\delta^2+\Gamma^2/4}$, which at zero detuning becomes $s_0 = I/I_s$. In the latter expression $I_s = \frac{\hbar\Gamma\omega_A^3}{12\pi c^2}$ is the saturation intensity.
Let us focus on the radiation pressure force: every time an atom absorbs or emits a photon, due to momentum conservation, it recoils in the same direction of the absorbed photon and in opposite direction with respect to the emitted one (see sketch in Fig. 1.4). The energy recoil is $E_r = \frac{\hbar^2 k_L^2}{2M}$, where k_L is the photon momentum and M is the mass of the atom.

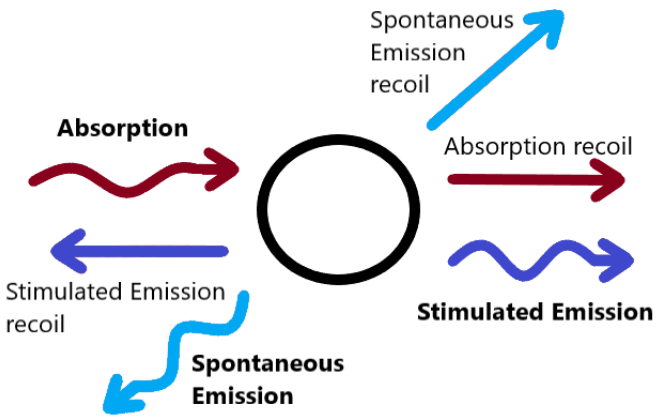

Figure 1.4: *Schematic sketch of absorption (red arrows) and emission phenomena (light blue arrows for spontaneous emission and purple for the stimulated one) and relative recoils.*

By considering a process of absorption and stimulated emission, the incoming and absorbed photon is re-emitted along the same direction and the two recoils are equal and opposite (see Fig. 1.4): the resulting force is, on average, zero. If instead we consider a number of absorption (all the photons have the same propagating direction) and spontaneous emission processes, then photons are emitted isotropically and the total force points along the incoming photons direction [12].

If we now consider a moving atom with velocity $\vec{v}$, we have to take into account the Doppler shift that modifies the detuning as $\delta' = \delta - \vec{k}\cdot\vec{v}$, where $\vec{k}$ is the radiation wave vector, and the radiation pressure force becomes

$$\vec{F}_{rad} = \hbar\vec{k}\frac{\Gamma}{2}\frac{\Omega^2/2}{(\delta - \vec{k}\cdot\vec{v})^2 + \Gamma^2/4 + \Omega^2/2} \tag{1.4}$$

From Equation 1.4 one can notice that if $\delta > 0$ the atom absorbs photons which propagate along the same direction, and it is accelerated. Otherwise, when $\delta < 0$, the atom interacts with those photons that are moving opposite to its $\vec{v}$ direction and, consequently, it is slowed down. Furthermore, the radiation pressure has a Lorentzian behavior as a function of both the detuning and velocity.
It is also easy to see that the force at resonance ($\delta = \vec{k}\cdot\vec{v}$) increases with the field intensity up to its maximum value, that, for $\Omega \gg \Gamma$, is $\vec{F}_{max} = \hbar\vec{k}\Gamma/2$.
The radiation pressure force has many applications in the field of laser cooling. In particular it lays the ground for the optical molasses (1.3.1) and the Zeeman slower (1.3.2) techniques, which are summarized in the following sections.

1.3.1 Optical molasses

The optical molasses is an experimental configuration in which radiative pressure combined with the Doppler effect is used to slow and cool atoms.
Let us consider a one-dimensional configuration in which an atom moves with velocity $\vec{v}$ and two laser beams of the same frequency, intensity and polarization are directed opposite one to the other. If the two beams have small intensity ($s \ll 1$), the total force experienced by the atom is found by adding the radiative force (Eq. 1.4) generated by each of the two laser beams, so that for atoms at rest the total force is null. Both beams are assumed to be equally red detuned with respect to the atomic transition ($\delta < 0$). Owing to the Doppler effect, counter-propagating photons get closer to the atomic resonance. Therefore, atoms will have a higher probability of absorbing (and emitting) photons from the counter-propagating beam, rather than from the co-propagating one. As a result, a net force opposite to their motion will slow them down.
The total force profile given by [10]

$$\vec{F} = \hbar\vec{k}\frac{\Gamma}{2}\Big[\frac{s}{1+4(\delta - kv)^2/\Gamma^2} - \frac{s}{1+4(\delta + kv)^2/\Gamma^2}\Big] \tag{1.5}$$

is shown as a function of atoms velocity in Fig. 1.5.
In the limit of low velocities, the total force can be approximated as

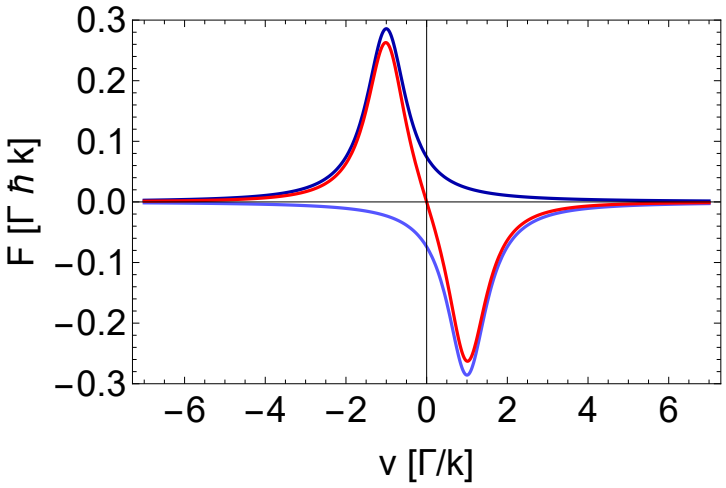

Figure 1.5: *Total force (Eq. 1.5) in unit of* $\hbar\Gamma k$ *as a function of the atom velocity in unit of* Γ/k *for a one-dimensional optical molasses. The two blue lines show the force from each beam and the red one is their sum. All the three curves are obtained with* $s = 0.4$ *and* $\delta = -\Gamma$.

$\vec{F} = -\beta\vec{v} + o(\vec{v}^3)$, that represents a friction force with damping coefficient

$$\beta = -8\hbar k^2 s \frac{\delta/\Gamma}{(1+4\delta^2/\Gamma^2)^2} \tag{1.6}$$

whose maximum value is reached for $\delta \simeq -0.3\Gamma$.
The lowest temperature attainable with an optical molasses is the Doppler temperature, which is defined as

$$k_B T_D = \frac{\hbar\Gamma}{2} \tag{1.7}$$

Actually, pioneering experiments on optical molasses revealed temperatures significantly lower than T_D [13] as I will better discuss in Sec. 1.5.

1.3.2 Zeeman slower

Typically the first experimental step to decrease the velocity of thermal atoms emitted by a heated solid source is the Zeeman slower technique[3]. We have already seen that a resonant laser beam, counter-propagating against the atoms, slow them down thanks to momentum transfer during several absorption and spontaneous emission cycles. Because of the Doppler effect, atoms that initially interact with the laser beam are slowed down and rapidly get off resonance and they cannot be further slowed. To maintain the resonant condition an external inhomogeneous magnetic field along the direction of the atomic beam is ap-

[3]The ZS is not needed only if the velocity of atoms emitted by the oven is lower than the capture-velocity of the MOT.

plied. Indeed the magnetic field introduces a spatially-dependent Zeeman shift that can compensate the variation of the Doppler effect:

$$\delta_{eff}(x) = \delta + kv(x) - \frac{\Delta\mu B(x)}{\hbar} = 0 \tag{1.8}$$

where δ_{eff} is the total effective detuning and $\Delta\mu$ is the difference in magnetic moment between the two atomic states coupled by the laser light.
Imposing a constant deceleration along the whole ZS length, the atom velocity is $v(x) = \sqrt{v_0^2 - 2ax}$, v_0 denoting the initial atoms velocity. Therefore, the magnetic field profile must be of the kind [14]:

$$B(x) = \frac{\hbar}{\Delta\mu}\left(\delta + k\sqrt{v_0^2 - 2ax}\right) \tag{1.9}$$

where L is the solenoid length. In this way all the atoms with v_0 lower than the ZS capture velocity[4] v_{max} are slowed down to a final v_f, whose value is upper bounded by the maximum MOT capture velocity. In our experimental setup $v_f \sim 40 m/s$ for both Lithium and Chromium atoms.
The choice of various parameters, such as the laser detuning δ, the solenoid length L and the maximum magnetic field B_{max}, depends on the desired ZS capture velocity v_c and the output velocity.
There are two main configurations for designing a Zeeman slower: the first one is the non-spin flip configuration, in which the magnetic field has the same sign over the whole ZS length, with $B(L) = 0$. The second is the spin-flip configuration that provides, at some spatial position within the ZS, a zero crossing of magnetic field. The ideal magnetic field in both configurations is shown in Fig. 1.6. The "normal" ZS configuration avoids low field regions along the ZS path, where

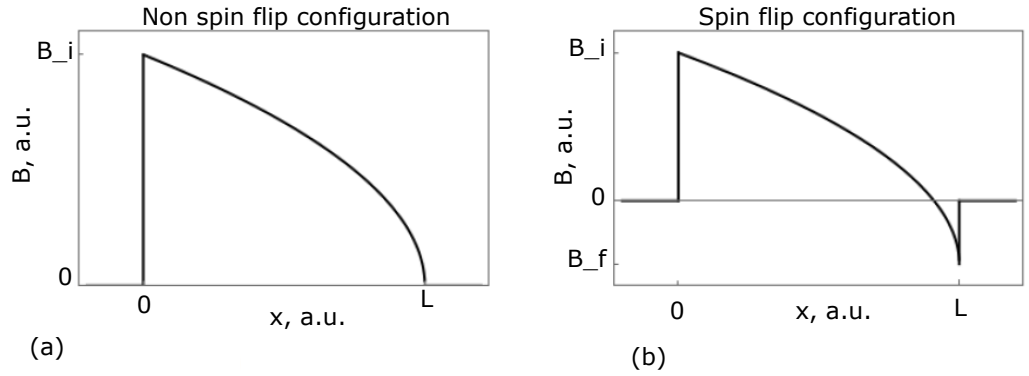

Figure 1.6: *Shape of the ideal Zeeman Slower field in the non-spin flip configuration (a) and in the spin flip one (b) [15].*

[4]The maximum capture velocity of a ZS is defined by $\delta_{eff} = \delta + kv_{max} - \frac{\Delta\mu B_{max}(x)}{\hbar} = 0$.

spin-flipping events can occur. Indeed, when $B = 0$ there is no more Zeeman splitting of the levels and atoms can occupy an off-resonant state and get out of the cooling cycle. On the other hand, the non spin-flip configuration requires a high initial value of magnetic field to ensure a large value of v_{max}. Moreover, the condition $B = 0$ at the end of the ZS makes the ZS light resonant with the atoms, perturbing the collected cloud in the MOT. On the contrary, in the spin-flip configuration, a non-zero magnetic field at the end of the ZS path perturbs the MOT position, modifying the location of the quadrupole field.
Both Cr and Li ZS implemented on our setup have a non-spin flip design.

1.4 Magneto-optical trap

Once an atomic beam has been slowed down, it is important to spatially confine atoms in an efficient way. The most common trap for neutral atoms is the magneto optical trap (MOT), that combines the optical molasses technique (Sec. 1.3.1) with a magnetic quadrupole field: this generates a force that depends on both the atom position and velocity.
Let us consider the one-dimensional case of two counter-propagating beams, red detuned with respect to the atomic transition $|J = 0\rangle \rightarrow |J' = 1\rangle$, plus a linear magnetic field $B(z) = bz$ as shown in Fig. 1.7. Because of the Zeeman effect, two of the three sublevels of the excited state ($M_j = 0, \pm 1$) have an energy shift that depends linearly on the position: $\Delta E = g'_f \mu_B M'_j bz$, where g'_f is the Landé factor, μ_B the Bohr magneton and M'_j is the angular momentum projection of the electronically excited state. If we suppose a polarization σ_+ for the co-propagating beam and σ_- for the counter-propagating one (see Fig 1.7) and a magnetic field gradient such that $bg'_f > 0$, then atoms moving along $+\hat{z}$ have higher probability to interact with the counter-propagating σ_- beam. Analogously, atoms moving along $-\hat{z}$ have a higher probability to absorb a photon from the σ_+ beam. This, combined with the viscous force provided by the optical molasses mechanism, leads to a total force that, in the limit of small intensities, reads as [16]:

$$F = \hbar k \frac{\Gamma}{2} \left[\frac{s}{1 + 4(\delta - kv - g_f \mu_B bz/\hbar)^2/\Gamma^2} - \frac{s}{1 + 4(\delta + kv + g_f \mu_B bz/\hbar)^2/\Gamma^2} \right] \quad (1.10)$$

If both the Doppler and the Zeeman shifts are small with respect to Γ, then the force can be written as

$$F \simeq -\beta v - \kappa z \quad (1.11)$$

that represents a damping term β, like the one found for the optical molasses mechanism (Eq. 1.6), and a harmonic term characterized by a spring constant $\kappa = \frac{g'_f \mu_B b}{\hbar k} \beta$.

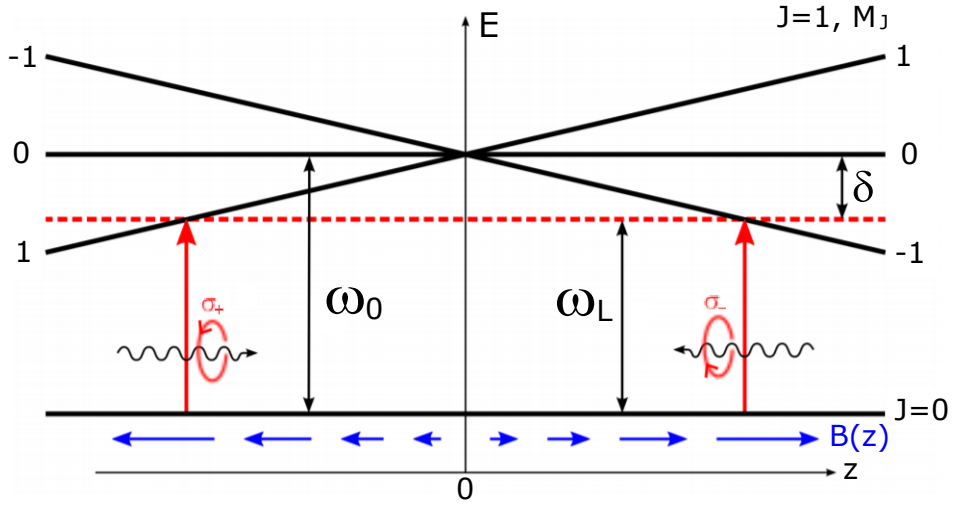

Figure 1.7: *The working principle of a MOT, considering an atomic transition* $|J=0\rangle \rightarrow |J=1\rangle$. *The figure is taken from [17].*

Figure 1.8 shows the dynamics of the atoms in the capture process: atoms moving slower than the capture velocity are trapped in the center of the MOT (in Figure represented as the 0-position). For a given cooling transition and atomic species, it is possible to describe the capture velocity as a function depending on the detuning and on the beam intensity [16]: $v_c = \frac{\hbar k^2}{2M}\frac{\Gamma}{|\delta|} r \frac{s}{1+s}$, where r is the radius of the beams. Both trapping times and capture velocity are limited by losses of atoms from the trap due to collision with the high-temperature background gas. Therefore, high vacuum conditions are needed to ensure long MOT lifetimes in experiments.

These results can be generalized to the three-dimensional case, by considering three pairs of counter-propagating beams, and to different total momentum of atomic levels, $J_g \rightarrow J_e = J_g + 1$.

As we have seen when discussing Fig. 1.2, a Lithium MOT operates on the cooling transition $|F = 3/2\rangle \rightarrow |F' = 5/2\rangle$. Anyway, owing to the very small hyperfine structure of the electronically excited state $2^2P_{3/2}$ of less than the natural width Γ, the cooling light, when not perfectly polarized, can also drive the undesired $|F = 3/2\rangle \rightarrow |F' = 3/2\rangle$ transition. From the $|F' = 3/2\rangle$ state, atoms can decay both in $|F = 3/2\rangle$, i.e. falling back within the cooling cycle, and in the $|F = 1/2\rangle$ state, 228MHz detuned from the $|F = 3/2\rangle$ manifold. In order to reintroduce these atoms in the cooling cycle an additional repumper light, resonant with the $|F = 1/2\rangle \rightarrow |F' = 3/2\rangle$ transition, is applied.

A similar scenario concerns also the fermionic ^{53}Cr for which two repumper lights are needed (see Fig. 1.3), differently from the bosonic ^{52}Cr isotope. Indeed, in the latter case, the absence of a hyperfine structure makes the cooling

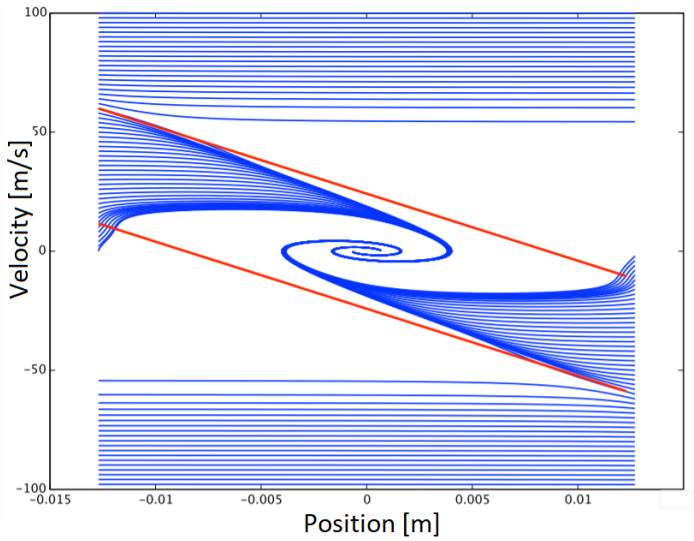

Figure 1.8: *Typical atom trajectories in the position-velocity plane for the small intensities regime, taken from [16]. In red are shown the lines along which the confining force is highest, i.e.* $\delta \pm kv \pm g_f \mu_B bz = 0$.

transition closed.

1.5 Sub-Doppler cooling

Already during the very first cooling experiments [13,18] temperatures below the Doppler limit were unveiled, because of the Sisyphus effect. This results from a non-negligible interference between two counter-propagating beams. Indeed, as explained in Ref. [19], if we consider two beams with orthogonal linear polarizations, and with same frequency and intensity, the polarization of the total field changes from σ_+ to σ_- and vice versa every $\lambda/4$ (see Fig. 1.9a), whereas in between it is elliptical or linear. Bearing in mind the simple case where the atomic ground state has an angular momentum $|J = 1/2\rangle$, the two Zeeman sublevels $M_g = \pm 1/2$ experience different light shifts, depending on the laser polarization (Fig. 1.9b).
A cycle of absorption and emission that involves the excited state results into an optical pumping between the sublevels of the ground state. Where the polarization is $\sigma_+(\sigma_-)$ the optical pumping is $|M_g = -1/2\rangle \rightarrow |M_g = 1/2\rangle (|M_g = 1/2\rangle \rightarrow |M_g = -1/2\rangle)$. Therefore, the spatial modulation of the polarization causes an analogous modulation of the optical pumping. The correlation between the modulation of the light shifts and of the optical pumping results in the Sisyphus cooling: an atom that moves from left to right, starting from the bottom of a valley, climbs up the potential losing its kinetic energy. If the sign of the detuning is

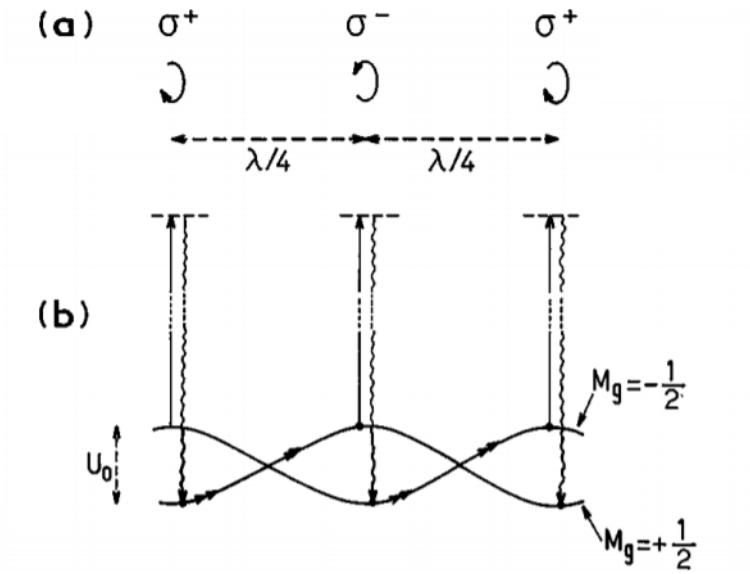

Figure 1.9: *a) The resulting polarization of the electric field is spatially modulated with a period $\lambda/2$. b) Spatially modulation of the light shift associated to the Zeeman sublevels $|M_g = \pm 1/2\rangle$ of the ground state. Figure taken from [19].*

properly chosen, the optical pumping transfers the atoms from the higher Zeeman sublevel to the lower one, the emitted photon having an energy higher than the absorbed one. After a number of Sisyphus cycles the atom is significantly cooled down.
Despite sub-Doppler cooling mechanisms allow to overcome the Doppler limit, there is anyway another restriction represented by the recoil velocity. For this reason, the lower attainable temperature within sub-Doppler processes is the recoil temperature [10]: $k_B T_r = \frac{\hbar^2 k^2}{2M}$, where k is photon wavevector and M is the atom mass.
As the Li D_2 cooling transition is concerned, the splitting between the hyperfine levels of the electronically excited state $2^2P_{3/2}$ is too small to allow any close transition and, consequently, the sub-Doppler mechanism is inefficient. For this reason, in order to further cool Li atoms below the Doppler limit, we use a gray-molasses technique (discussed in the next section) based on the D_1 line, whose excited state $2^2P_{1/2}$ features a significantly more resolved hyperfine structure (as we can see Fig. 1.2).

1.5.1 Gray molasses

The gray molasses process results from a combination of velocity selective coherent population trapping (VSCPT) and Sisyphus cooling [20]. While we have already examined the working principle of the Sisyphus effect, in order to explain

the VSCPT process, we have to consider a Λ three-level system (see Fig. 1.10).

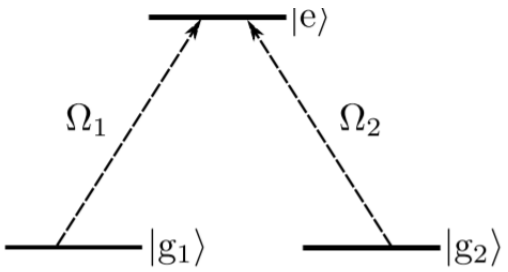

Figure 1.10: *Atomic Λ three-level scheme coupled by two light fields. Ω_1 and Ω_2 are the Rabi frequencies of the two beams. Figure taken from Ref. [21].*

The two ground-states[5] $|g_1\rangle$ and $|g_2\rangle$ are coupled with the excited one $|e\rangle$ by two laser beams characterized by a Rabi frequency Ω_1 and Ω_2 respectively. This problem can be studied by introducing a new basis for the ground state: in this case the new eigenstates are the so-called dressed states (the bright state $|\Psi_B\rangle$ and the dark one $|\Psi_D\rangle$), both defined as a linear combination of $|g_1\rangle$ and $|g_2\rangle$. Let us consider a Hamiltonian of the kind $\hat{H} = \hat{H}_{at} + \hat{V}$ where $\hat{H}_{at}$ is the atomic hamiltonian and $\hat{V}$ is the operator representing the interaction of the atom with the laser lights. While $\hat{V}$ couples the bright state to the excited one, the $\hat{V}$ operator is such that $\hat{V}|\Psi_D\rangle = 0$ for the dark state and, consequently, the transition $|\Psi_D\rangle \rightarrow |e\rangle$ does not occur.
However, if we now consider a moving atom and add to $\hat{H}$ the kinetic term $\frac{\hat{p}^2}{2m}$, treated as a perturbation, we find a non zero coupling probability between $|\Psi_D\rangle$ and $|\Psi_B\rangle$ that depends on the atom velocity squared [21]:

$$P = \left| \frac{\langle \Psi_B(p)| \frac{\hat{p}^2}{2m} |\Psi_D(p)\rangle}{E_B - E_D} \right|^2 \tag{1.12a}$$

$$\langle \Psi_B(p)| \frac{\hat{p}^2}{2m} |\Psi_D(p)\rangle = -\frac{2\Omega_1\Omega_2}{\Omega^2} \hbar k \frac{p}{m} \tag{1.12b}$$

where $\Omega = \sqrt{\Omega_1^2 + \Omega_2^2}$ is the generalized Rabi frequency and p/m is the atomic speed. Therefore, the VSCPT mechanism consists on the fact that atoms with low speed are kept in $|\Psi_D\rangle$, whereas fast atoms are transferred to the bright state, from which they can undergo $|\Psi_B\rangle \rightarrow |e\rangle$ transitions.
The gray molasses technique employs three sets of counter-propagating blue-detuned beams in σ^+/σ^- polarizations that, as we have already seen in the Sisyphus cooling, introduce a modulation of both the light shift and the optical pump-

[5] In this configuration $|g_1\rangle$ and $|g_2\rangle$ are degenerate, but this condition will be abandoned afterwards.

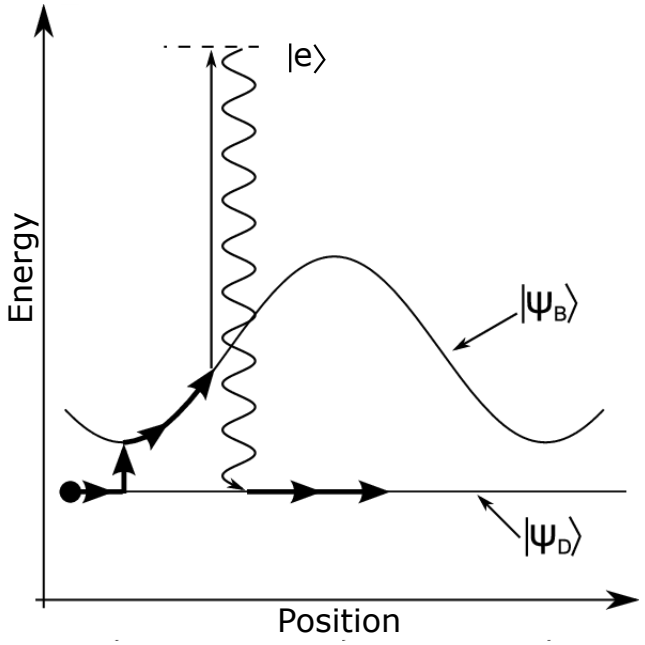

Figure 1.11: *Sketch of gray-molasses mechanism: atoms with enough kinetic energy are transferred from the dark to the bright state according to velocity selective coupling. Then, kinetic energy is transfered to potential energy when an atom climb the potential hill of the bright state before the absorption process [22].*

ing rate for the bright state. Moreover, if both the beams are blue-detuned, then the bright state has a light shift towards higher energy values [22]. The dark state, instead, does not interact with the radiation, so its energy does not present any modulation, as sketched in Fig. 1.11. As a consequence, the coupling from the dark to the bright state will be maximum at the valleys of the bright state potential, where the difference in energy between the bright and the dark state is minimum (see Fig. 1.11). When the atom is transferred in the bright state, it climbs the potential, losing kinetic energy. The transition due to the laser light between $|\Psi_B\rangle$ and the excited state $|e\rangle$ occurs preferentially in correspondence of potential hills [20] and, once in the excited state, the atom can decay into the dark state. After a certain number of this cooling cycles, the probability for the $|\Psi_D\rangle - |\Psi_B\rangle$ coupling decreases, according to the low velocity of the atoms.
Unlike the Sisyphus cooling, within a gray molasses an atom that remain in the dark state does not absorb anymore and, theoretically, temperatures below the single photon recoil can be achieved.
An additional feature of gray molasses, connected with the phenomenon of VSCPT, is the sensitive dependence of the atomic cloud temperature upon the relative detuning of the two laser beams $\Delta = \delta_1 - \delta_2$. In particular, the temperature exhibits a minimum at the Raman condition $\Delta = 0$, with a characteristic Fano profile with sub-natural linewidth [23, 24].

As discussed in Ref. [25] and only briefly mentioned here, such a peculiar trend can be ascribed to the Δ-dependence of the population σ_{ee}^{st} of the excited state involved in the gray molasses cooling cycle, which is zeroed once the Raman condition is fulfilled. Fig. 1.12 shows the stationary population σ_{ee}^{st}, obtained by solving the OBE (Optical Bloch Equations) for the Λ-system for the specific conditions of power and detuning δ_2 of one of the two lasers detailed in the legend.
It is apparent how, around $\delta_1 = \delta_2 = -1.5\Gamma$, σ_{ee}^{st} features a sharp dependence on

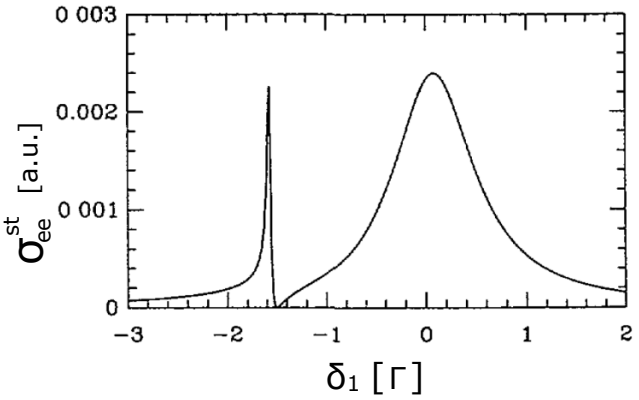

Figure 1.12: *Steady-state population of the excited state σ_{ee}^{st} as a function of δ_1 in units of Γ, where $\Gamma = \Gamma_1 + \Gamma_2$ and Γ_1 (Γ_2) is the spontaneous emission rate from $|e\rangle$ to $|g_1\rangle$ ($|g_2\rangle$). This picture is taken from [25] and the curve is calculated with $\delta_2 = -1.5\Gamma$, $\Omega_2 = 0.7\Gamma$ and $\Omega_1 = 0.025\Gamma$.*

δ_1, with a characteristic Fano profile of typical width $\ll \Gamma$, and a zero at $\delta_1 = \delta_2$, i.e. at the Raman condition.
More details about this behavior, together with its approach based on the scattering theory, can be found in Ref. [25].
During the gray molasses characterization for the ^6Li atoms, we experimentally find a similar behavior in the trend of the atoms temperature as a function of the relative detuning $\Delta = \delta_1 - \delta_2$ (see Sec. 3.3).

1.5.2 Optical dipole trap

As we have already seen in Sec. 1.3 and in particular in Eq. 1.2, the presence of an interaction between the atom and the laser light leads to a force composed by two terms. The term proportional to $\vec{\nabla}\Omega(\vec{r})$ and U_{st} is responsible for the generation of the dipole force. By writing explicitly U_{st}, it is possible to determine the potential associated to the dipole force:

$$\vec{F} = -\vec{\nabla}U \rightarrow U = \frac{\hbar\delta}{2} log\left(1 + \frac{\Omega^2/2}{\delta^2 + \Gamma^2/4}\right) \tag{1.13}$$

If we consider an off-resonance radiation, i.e. $\delta \gg \Omega, \Gamma$, we can expand the logarithm, obtaining $U \simeq \frac{\hbar\Omega^2}{4\delta}$. This means that the potential is proportional to I/δ, where I is the beam intensity. Additionally, the potential behavior depends on the detuning sign, as we can easily see in Fig 1.13: for red detuning (i.e. $\omega_A > \omega_L$), the potential minimum corresponds to the maximum value of the light intensity, and a Gaussian beam traps the atom. On the contrary, if the light is blue detuned, the laser is antitrapping and the potential minimum corresponds to the minimum in intensity.
In order to efficiently trap atoms in a ODT, it is important to have a radiation characterized by a high value of intensity and a large red-detuning. The choice of a high intensity is easy to understand, given that this sets the trap depth. For what concern the detuning requirement, we have to consider that, even though the trapping potential decreases for big detuning as $1/\delta$, the off-resonant scattering rate scales as $1/\delta^2$ [26]. Therefore, in order to keep the scattering rate as low as possible and hence to minimize the associated atom losses, it is convenient to use large detunings.
Let us consider a Gaussian laser beam propagating along the z axis with a focus

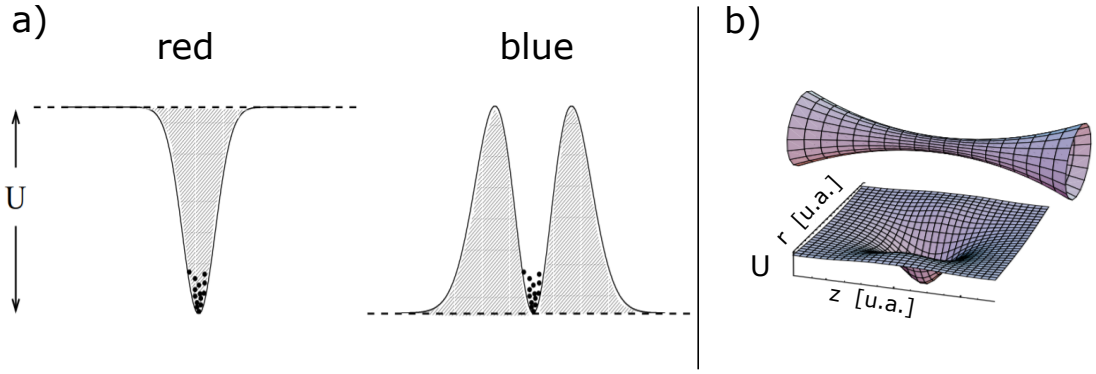

Figure 1.13: *a) illustration of dipole trap with red and blue detuning: while in the first case a simple Gaussian laser beam is considered, in the second is assumed a Laguerre-Gaussian laser beam [26]. b) focused Gaussian red-detuned laser beam and the resulting dipole potential [27].*

at $z = 0$, characterized by a beam waist w_0. Its intensity profile reads:

$$I(z,r) = I_0 \left[\frac{w_0^2}{w(z)^2} \right] e^{-\frac{2r^2}{w(z)^2}} \tag{1.14}$$

where $w(z) = w_0 \sqrt{1 + \left(\frac{z}{z_R}\right)^2}$ is the beam size at the position z and $z_R = \frac{\pi w_0^2}{\lambda}$ is the Rayleigh length. In the limit of small values of r and z (i.e. near the beam focus)

we can expand Eq. 1.14 obtaining the following intensity shape:

$$I(z,r) \simeq I_0\Big(1 - \frac{z^2}{z_R^2} - \frac{2r^2}{w_0^2}\Big) \tag{1.15}$$

that corresponds to a harmonic potential of the kind:

$$U(z,r) \simeq -U_0 + \frac{1}{2}m\omega_r^2 r^2 + \frac{1}{2}m\omega_z^2 z^2 \tag{1.16}$$

where $\omega_z = \sqrt{\frac{2U_0}{mz_R^2}}$ and $\omega_r = \sqrt{\frac{4U_0}{mw_0^2}}$. As one can see, $\omega_z \propto \omega_r \frac{\lambda}{w_0} \ll \omega_r$, hence the potential in the radial directions is much steeper than in the axial direction, as shown in the right side of Fig. 1.13.

1.5.3 Evaporative and sympathetic cooling

The last step required in order to reach the quantum degenerate regime in our experiment relies on evaporative cooling for Lithium and sympathetic cooling for Chromium atoms.
Despite the implementation of these techniques goes beyond my thesis work, I briefly recall the basic working principles of these two cooling methods.
The evaporative cooling is composed by two conceptual steps: i) the selective removal of those atoms that have an energy higher than the average energy of the sample; ii) the rethermalization of the remaining atoms by means of elastic collisions [10].
In order to remove the more energetic atoms there are two different methods depending on the trap typology: within an ODT it is sufficient to decrease the trap depth by reducing the laser beam intensity. In a magnetic trap, instead, a radio-frequency (or micro-wave) radiation is applied in order to induce a spin flip on the highest energy atoms which occupy the outermost region of the trap and to transfer them towards Zeeman sublevels that are not trapped.
After this selective removal, the leftover sample rethermalizes and its velocity distribution turns into a Maxwell-Boltzmann with a smaller width, i.e. with a lower temperature.
Since this thermalization process relies on elastic collisions, a sample composed by fermionic atoms has to be trapped in two different internal states. In fact, the Pauli exclusion principle prohibits identical fermions to collide in s-wave, which is the only relevant scattering channel in the ultracold regime. For this reason, in our ODT we will trap ^{6}Li atoms equally populating the two lowest Zeeman states.
Regarding Chromium atoms, they will be cooled by a sympathetic mechanism: this technique is often employed in order to cool those atomic species that can

not easily thermalize, or when the sample has a low atom number, such that it is desirable to cool it without particle losses. The basic concept of this second cooling mechanism is to mix the atomic species that can not be cooled evaporatively with a second, more abundant one, that instead can be efficiently cooled. If this second species is cooled, then also the first one can thermalize through interspecies collision.
In our case, it is possible to design and realize optical potentials that are deeper for Cr than for Li by means of the combination of high power IR and green laser sources. Provided that we will find favorable interspecies Cr-Li scattering properties, unknown so far, we will then use the Li as a coolant for Cr atoms, without expecting substantial Cr losses.

Chapter 2

Compensation coils setup: design, test and applications

One of my major contributions to the experiment during my thesis period has been the realization of a set of compensation coils. In particular, I designed, produced and tested three pairs of coils that I subsequently installed on the main experimental apparatus along the three spatial directions. Moreover, I soldered and tested their relative electronic control system.
These coils, which adjoin the main MOT and Feshbach coils setups, can be employed for various purposes: first, in the Helmholtz configuration, they allow to controllably adjust the quadrupole center position of the MOT of Li and Cr atoms relative to the ODT, and to eliminate spurious fields that decrease the performances of the gray molasses stage [20, 24]. Second, the z-coils switched in an anti-Helmholtz configuration and combined with the Feshbach and the MOT coils, will enable to produce a controlled magnetic gradient on top of a homogeneous field pointing along the gravity direction. This, in turn, will enable to adjust the gravitational sag experienced by Li and Cr atoms within the ODT, during the evaporation stage [28–31].
This chapter is organized as it follows: in Sec. 2.1 I describe the main characteristics of the coils and of the electronic control circuit. In particular, I report the expected profile of the magnetic field in the Helmholtz and anti-Helmholtz configuration[1] respectively and the characterization of the electronic circuit. Sec 2.2 provides the analysis, both theoretical and experimental, of the cloud shift due to the compensation coils field along the three axes. Finally, in Sec. 2.3 I present a simulation carried out with Wolfram Mathematica of the optical potential experienced by both Li and Cr atoms within the ODT. In particular, I focus on the role played by gravity on determining the barycenters of the two clouds and their

[1] In this thesis I refer to the Helmholtz and anti-Helmholtz configuration even though the relative distance d between the coils is larger than their radius R.

relative position, and discuss how a magnetic field gradient can be employed in order to cancel the relative gravitational sag of the two species.

2.1 Realization and implementation

A set of three pairs of compensation coils, one for each space direction[2], (i.e. x- y- and z-coils) is realized in order to eliminate possible spurious magnetic fields or to create a magnetic gradient[3]. Both their radii and their number of loops, as well as the relative distance between coils of the same axes, are limited by physical constraints, represented by other optical and mechanical components near the science chamber (see right pictures of Fig. 2.1). The coils are all made of copper wire of radius $0.45mm$ (Fig. 2.1) and their main design parameters are listed in Table 2.1.

		x-axes	y-axes	z-axes
Radius	R [cm]	5.9	4.0	7.5
Loops	N	21	34	30
Relative distance	d [cm]	32	32	27
Magnetic field (for I=3.5A)	B_0 [G]	0.65	0.53	2.01

Table 2.1: *Main design parameters of the compensation coils. The magnetic field B_0 is calculated for the two coils in Helmholtz configuration and at half of their relative distance d, i.e. in correspondence of the atomic cloud, where the magnetic field features a constant value.*

By considering a certain value of current flowing in the same direction (clockwise or anticlockwise) in both the coils, which are placed at the position $x = \pm d/2$, a constant magnetic field B_0 is generated at $x = 0$. The B_0 value depends on the distance between the two coils, on their internal radius (R) and on their number of loops (N). For each set of coils the corresponding B_0 calculated for a current value of $I = 3.5A$ is shown in Tab. 2.1. For this configuration the whole calculated magnetic field profile, composed by the sum of the field generated by each coil,

[2]Actually, because of the presence of other optical and mechanical components, the x- and y-coils are not orthogonal, but they make an angle of about 125°, as we will see in the next section.

[3]On the experimental setup are already implemented two pairs of coils to this latter aim: the MOT coils and the Feshbach coils. More detail in Chapter 2 of E. Neri's PhD thesis [15].

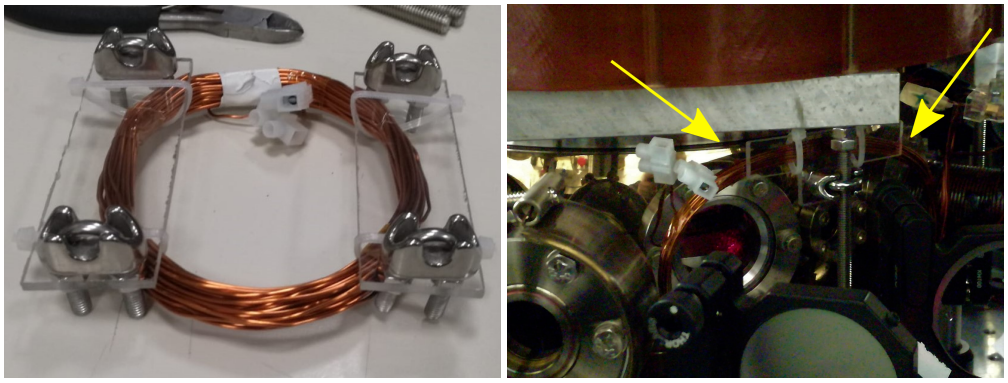

Figure 2.1: *x-axis coil and relative holder stripe (on the left) later implemented on the experimental setup (right side). In the second panel the coil is indicated by the yellow arrows.*

can be expressed as

$$B(x) = \frac{\mu_0 N I R^2}{2(R^2 + (x + d/2)^2)^{3/2}} + \frac{\mu_0 N I R^2}{2(R^2 + (x - d/2)^2)^{3/2}} \tag{2.1}$$

and it is represented on the left side of Fig. 2.2. In the expression above μ_0 is the magnetic permeability.

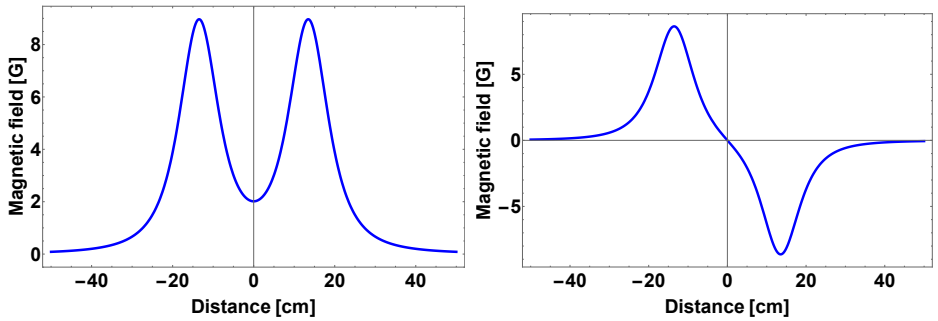

Figure 2.2: *Simulation of the magnetic field profile generated by the compensation coils of the z-axis, by considering a current of $I = 3.5A$, calculated through Wolfram Mathematica. The trend on the left corresponds to the coils in Helmholtz configuration, while in the profile on the right the coils are in anti-Helmholtz configuration.*

By reverting the sign of the current in one coil, the same setup can generate at the center of the coil setup $x = 0$ a magnetic field gradient (right panel of Fig. 2.2). In this case, the total magnetic is given by Eq. 2.1, but with the minus between the single coil contributions. As better explained in Sec. 2.3, this latter configuration will be useful along the vertical direction: indeed a gradient can be employed to compensate a displacement of atomic clouds of different atomic species, due to

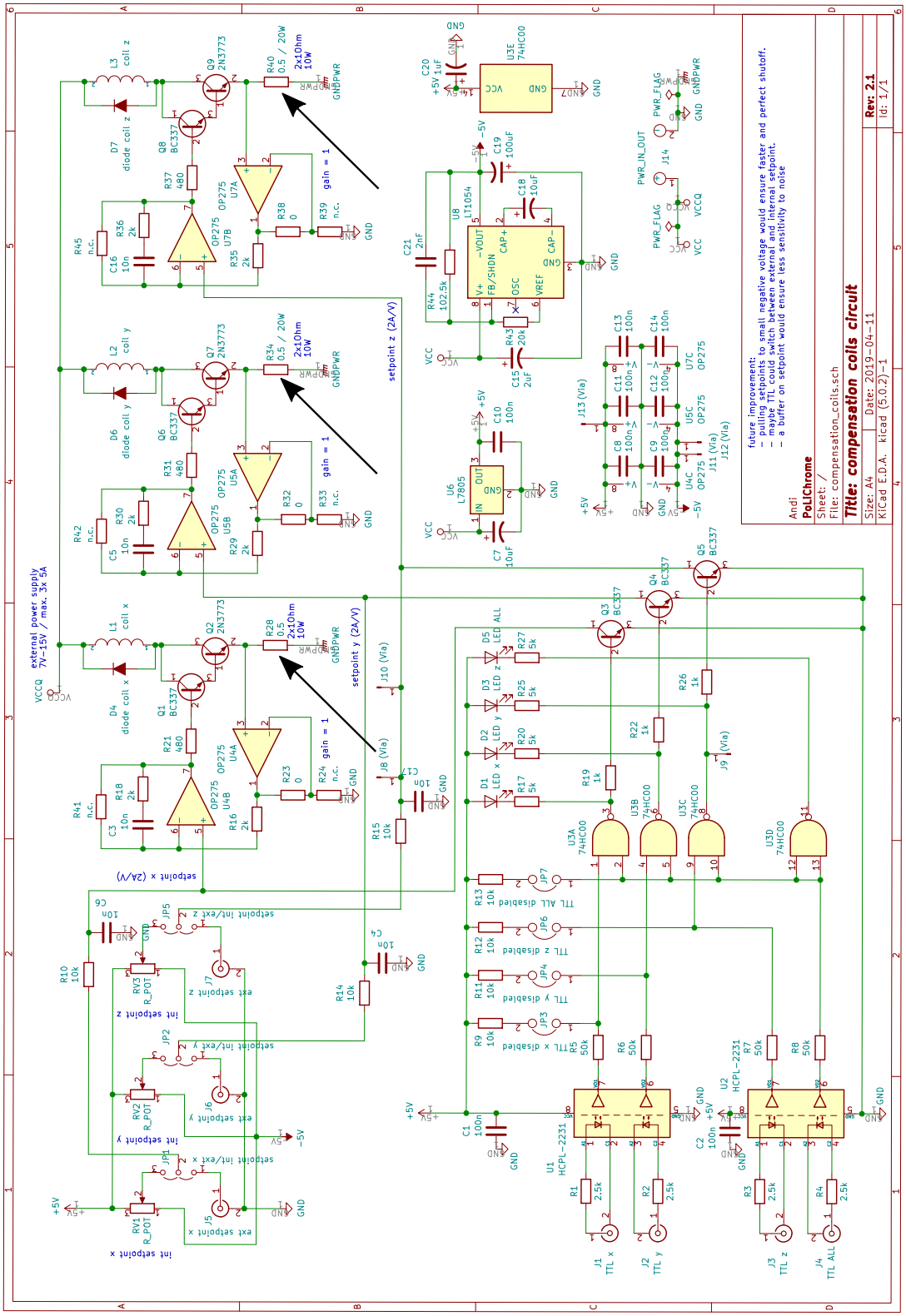

Figure 2.3: *Design of the electronic control of the three pairs of coils.*

gravity. The simulated gradient generated along the z axis by the compensation coils with a current of $3.5A$ is $\frac{\partial B}{\partial z} = 0.34\frac{G}{cm}$.
Fig. 2.3 summarizes the electronic circuit design that employing one single external power supply, allows to independently adjust the current in each set of compensation coils. An image of the actual soldered circuit board is shown in Fig. 2.4.

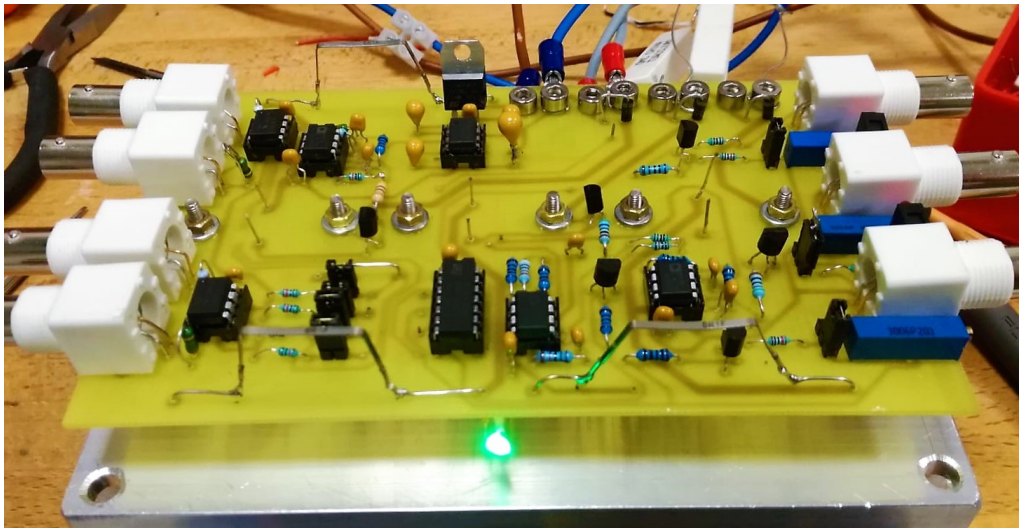

Figure 2.4: *Picture of the realized circuit board used for the electronic control of the three pairs of coils.*

In all the three sets of coils it is possible to maintain a constant current value up to $I = 3.5A$ with no electronic oscillations, nor relevant heating of the coils. The current can be set both manually through three trimmers (variable resistors), and electronically with a digital command in the routine program. The switch on/off can be regulated with a TTL control and the corresponding characterization in time was carried out by monitoring the variation in the voltage on a resistor of about $0.5 - 1\Omega$ (represented by R_{28}, R_{34} or R_{40}, indicated by black arrows in the upper part of Fig. 2.3), that emulates the coils.
The switch on occurs in $750 - 800\mu s$ for all the three sets and almost independently from the set current value. During this time the voltage value jumps from 0 to the 90% of its maximum value.
More interesting is the switch off timescale. Indeed, while for all our purposes we do not envision strong constraints regarding the switching on time of the compensation coils, it is desirable to have the possibility to quickly switch them off.
The switch off time is characterized in Fig. 2.5 for the y-axis coils (but analogous profiles are found by analyzing the response of the other two pairs) at I=2A (left) and I=3.5A (right), respectively.
In both cases, the signal reaches 10% of its initial value in about $100\mu s$. In Fig. 2.5

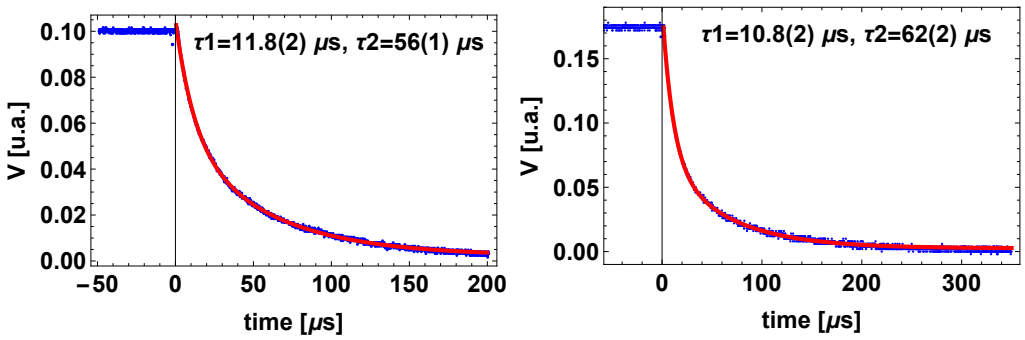

Figure 2.5: *Characterization of the switch off time for the y-axes compensation coils circuit. The two panels show the behavior of the y-axes circuit for two different current values: I=2A (left) and I=3.5A (right). The oscilloscope signal monitoring the voltage signal across R_{34} is represented by blue dots, whereas the fit is the red line. More detail about the fitting function in the main text.*

I also show the best fit of the measured voltage drop, analysed by using a double exponential decay as fitting function: $V = V_0(e^{-(t-t_{01})/\tau_1} + e^{-(t-t_{02})/\tau_2}) + \alpha$. The resulting values of τ_1 and τ_2 and their correspondent uncertainty are listed in Fig. 2.5.
After realizing and testing both the three sets of coils and the electronic circuit, I integrated them within the main experimental apparatus. For the x- and y-axis pairs, I fixed the coils on the bars inserted in the MOT coils resin (more detail in chapter 2 of Ref. [15]) by means of two plexiglas stripes. A picture of one x-coil with its plexiglas holder installed on the setup is shown in Fig. 2.1. Also the z-axis coils are fixed on a plexiglas support and placed above and below the science chamber. In any case, the coils are installed as near as possible to the chamber, at the same distance from its center. In this way, a constant B_0 (or a magnetic field gradient) is produced at the center of the chamber, i.e. where the atoms clouds are formed.

2.2 Calibration of the coils on the Li cloud

As we have already seen in the first chapter and in particular in Sec. 1.4, the MOT working principle is based on the presence of a quadrupole magnetic field gradient. The atoms are trapped in the region where the magnetic field is zero and, consequently, if an offset bias field B_0 is added to the gradient, the zero-field location (thus the cloud of trapped atoms) shifts. Indeed, by considering a magnetic field gradient along the x_i direction ($B(x_i) = b_i x_i$), adding a constant magnetic field B_0 in the same direction leads to a total magnetic field that is zero

in the position $x_{eq} = \frac{B_0}{b_i}$:

$$B(x_i) = b_i x_i \rightarrow B(x_{eq}) = 0 \quad at \quad x_{eq} = 0 \tag{2.2}$$

$$B(x_i) = b_i x_i \pm B_0 \rightarrow B(x_{eq}) = 0 \quad at \quad x_{eq} = \frac{\mp B_0}{b_i} \tag{2.3}$$

This translation, depends linearly upon the B_0 value, thus upon the current flowing within the coils.
For instance, the gradient along the z direction generated by the Feshbach coils in quadrupole configuration, whose characteristics are detailed in E. Neri's PhD thesis [15], is of about $24.4\frac{G}{cm}$ with a current value of $20A$. If to this gradient is added a magnetic field bias $B_0(I = 3.5A) = 2.01G$ produced by the compensation coils along the z direction, one expects a shift of the zero field position of $\Delta z_{eq} = 2.01/24.4cm = 0.824mm$.

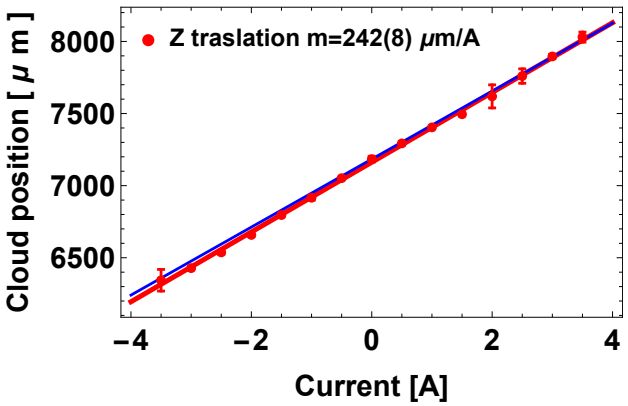

Figure 2.6: *Shift along the z direction caused by the compensation coils. The data (red dots), representing the translation of atoms experimentally observed by varying the current in the z compensation coils, are taken through an absorption imaging at $1ms$ of time of flight (TOF). The lines represent the linear fit of the data (red) and the expected shift previously calculated (blue). The coefficient obtained through the fit is $m = 242(8)\mu m/A$, that corresponds to a maximum measured shift $\Delta z_m^{max} \simeq 1.69(6)mm$, consistent with the theoretical value $\Delta z_t^{max} \simeq 1.64mm$. The uncertainty on data is the maximum deviation from the mean calculated with 6 different data sets. Regarding the coefficient m instead, the uncertainty is evaluated by considering the maximum and minimum slope provided by a linear fit of the data.*

More generally, bearing in mind a bias field $B_0 = \frac{2.01G}{3.5A} I[A] = 0.57\frac{G}{A} I[A]$ I expect, according to a magnetic gradient of $24.4\frac{G}{cm}$, a trend of the position where the atomic cloud is created (z_{eq}) of

$$z_{eq} = \frac{0.57\frac{G}{A} I[A]}{24.4\frac{G}{cm}} = 0.234\frac{mm}{A} I[A] \tag{2.4}$$

Therefore, by considering a maximum current of $I_{comp} = \pm 3.5A$, one expects an overall maximum shift, achievable with the z-coils, of $\Delta z_{max} = 0.234 \times 3.5 \times 2mm = 1.638mm$.
I directly measured the shift of the position of a cloud of ^{6}Li atoms, trapped in a MOT and further cooled by means of a gray molasses stage based on the D_1 line (see Sec.1.5.1 and 3.3), as a function of the current set in each axis of the compensation coils. The outcome of this measurement for the z direction is shown in Fig. 2.6: the red dots represent the experimental data with their statistical uncertainty, while the red line is the best linear fit. The blue line is the linear trend expected theoretically. From the figure one can notice how the translation directly measured on the atoms matches the expected trend.
The choice of monitoring the atoms in the D_1 gray molasses stage is motivated by the fact that this cooling stage does not modify the position of the atoms that remain in the center of the MOT quadrupole even when the MOT coils are switched off. Moreover after the gray molasses the cloud size is smaller and, consequently, it is easier to detect small shifts of its barycenter.

As far as the plane x-y is concerned, the analysis of the cloud shift is a bit different. Indeed, while for the z-axis the imaging is perpendicular to the atoms translation and, therefore, the cloud movement is visible 1:1 on the camera, along the plane it is necessary to take into account the angle between the coils axis and that of the imaging camera (θ_x for the x-coils) which is represented in green in Fig. 2.7.

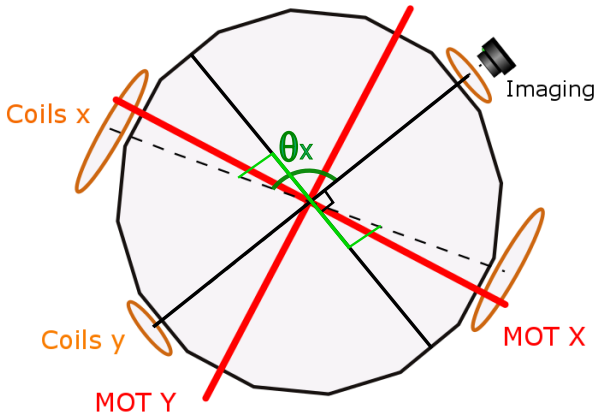

Figure 2.7: *Sketch of the X-Y plane geometry. In red are depicted the X and Y MOT beams, while the black dashed line represents the axes of the x-coils. The black solid lines indicate the direction of the imaging and its orthogonal axes. In green is depicted the angle θ_x formed by the x-coils and the imaging axes. Moreover, the projection of the translation along the x-coils direction is represented in green on the orthogonal axes to that of the imaging.*

In figure it is possible to notice the geometry of the plane: the y-coils are on the same axes of the imaging, while the x coils are centered between the MOT X windows and the adjacent one (on the right), namely at an angle $\theta_x = 124°$ with respect to the imaging axes.
Similarly to what has been done for the z axis, I monitored the position of the ^6Li atoms cloud at different current values flowing within the x-coil pair. A similar calibration of the y-coils is carried out and leads to similar results. After that the y-coils have been placed on the same axis of the imaging (see Fig. 2.7) and, therefore, in this latter configuration the translation due to the y-coils is not detectable with the camera.
The magnetic gradient on the plane is that expected (and experimentally observed) for the Feshbach coils, but reduced of a factor 2 with respect to its value along the vertical direction [32]. By considering the constant magnetic field generated by the x-coils B_{0x} predicted by simulations, it is possible to extract the effective angle at which the coil pair is located. Indeed, the cloud shift observed on the camera is the projection on the imaging axis of the effective translation (see green segment in Fig. 2.7). This approach is justified by the fact that the coils position is the more uncertain parameter of this configuration.
Assuming, therefore, a magnetic field gradient of about $12.2\frac{G}{cm}$ and a maximum current value in the coils $B_{0x}(I = 3.5A) = 0.65G$, one expects a maximum shift of the quadrupole center $\Delta x^{th}_{max} = 1.065mm$.
In Fig. 2.8 is shown the measurement of the translation generated by the x-coils as a function of the current value.

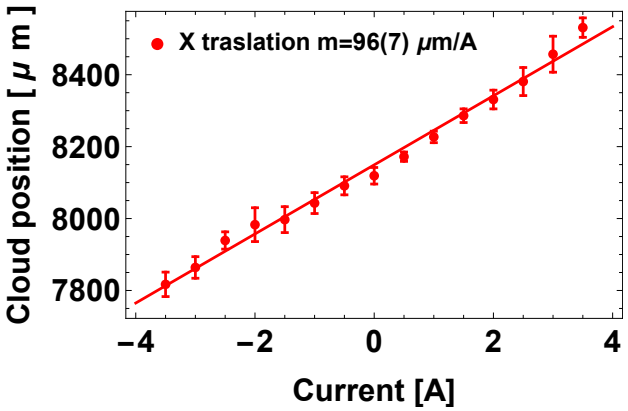

Figure 2.8: *Measure of the translation due to the x-coils as a function of the current. The data (red dots) are taken with an absorption imaging of the ^6Li cloud, after a TOF of 1ms. The linear fit (red line) allows to derive the shift coefficient that is m = $96(7)\frac{\mu m}{A}$. Also in this case the uncertainty on data is the maximum deviation from the mean and that on the m coefficient is evaluated by considering the maximum and minimum slope achievable from data.*

From the slope derived by the linear fit (red line), it is possible to evaluate the total measured shift $\Delta x_{max}^{exp} = 0.672mm$. This value can be related to that previously calculated Δx_{max}^{th} simply through the sine of θ_x: $\Delta x_{max}^{exp} = \Delta x_{max}^{th} \times \sin\theta_x^{exp}$. From this relation it is possible to observe that the experimentally measured shifts correspond to an angle $\theta_x^{exp} = 141°$. The mismatch with the expected $\theta_x = 124°$ is likely due both to an imperfect alignment of the coils and to an eventual displacement between the center of the quadrupole gradient and the position where the coils create the constant B_{0x}.

2.3 Simulation of optical dipole potential and gravitational sag

One of the most delicate steps towards the attainment of the degenerate regime of the Cr-Li mixture is the simultaneous loading in the ODT and the subsequent evaporative and sympathetic cooling stages. As we have explained in Sec 1.5.2, a Gaussian laser beam will trap the atoms if it is red detuned with respect to the relevant atomic transitions. In our experiment a bichromatic trap is needed to efficiently trap both Li and Cr atoms. Indeed, even though an infrared radiation at $1070nm$ will trap both species, it does not allow to create a potential sufficiently deep for Cr atoms, if compared to that experienced by Li atoms. Therefore, an additional green laser at $532nm$, superimposed to the IR one, strongly trapping (antitrapping) for Cr (Li) atoms, is employed to realize an overall potential deeper for Cr than for Li.
At the beginning of the ODT stage, when the lasers have high power, the gravitational sag effects are negligible. But during the evaporative cooling the beam powers are decreased, and the presence of gravity may have relevant and different (for atomic species with different mass) consequences. In particular, as we will see, the gravitational potential tilts the optical potential with a slope that depends on the atoms mass. This effect is known as gravitational sag and it can be balanced by means of a magnetic field gradient.

2.3.1 Optical dipole potential

In order to devise the most appropriate trapping potential for both species, to characterize the relative gravitational sag for Li and Cr, and to understand how to cancel it by means of a controlled magnetic field gradient, I have simulated the bichromatic potential for the two species, scanning different powers and beam waists.
Following the approach described in Ref. [26] and considering a multilevel atom,

the optical potential experienced by the atom in a state $|i, M_{Ji}\rangle$ depends on the magnetic quantum number M_J, on the polarization of the light, and on the coupling strength and detuning of all allowed transitions connected with the $|i, M_{Ji}\rangle$ state. Neglecting corrections due to the presence of an eventual hyperfine structure, the optical dipole potential can be written as [9]:

$$U_{i,M_{Ji}}(\vec{r}) = -3\pi c^2 I(\vec{r}) \sum_n \frac{sign(\omega_{ni})\Gamma_{M_{Ji},n}}{\omega_{ni}^2(\omega_{ni}^2 - \omega^2)} \tag{2.5}$$

where $\omega_{ni} = \omega_n - \omega_i$ is the frequency associated to the transition between the levels i and n, $\Gamma_{M_{Ji},n}$ is the coupling rate between a sublevel (i, J_i, M_{Ji}) and the arrival level (n, J_n, M_{Jn}), ω is the laser frequency and $I(\vec{r})$ is its intensity profile (Eq. 1.14).
While, in practice, the ODT for Li is fully determined by accounting for the D_1 and D_2 transition lines only, the simulation of the optical potential of Cr requires to consider basically the whole atomic spectrum, much richer than that of alkalis. In particular, for this species the ODT simulation, based on a Mathematica code, has been carried out for bosonic ^{52}Cr, but, not considering the hyperfine structure, analogous results are expected for the ^{53}Cr isotope. Fig. 2.9 shows an example of the radial and axial potential experienced by ^{6}Li atoms, calculated for the parameters detailed in the caption, produced by the individual infrared and green lasers (respectively the red and green curve) and their sum (brown curve). The depicted potential profiles are evaluated considering a linear light polarization and $M_J = -1/2$.

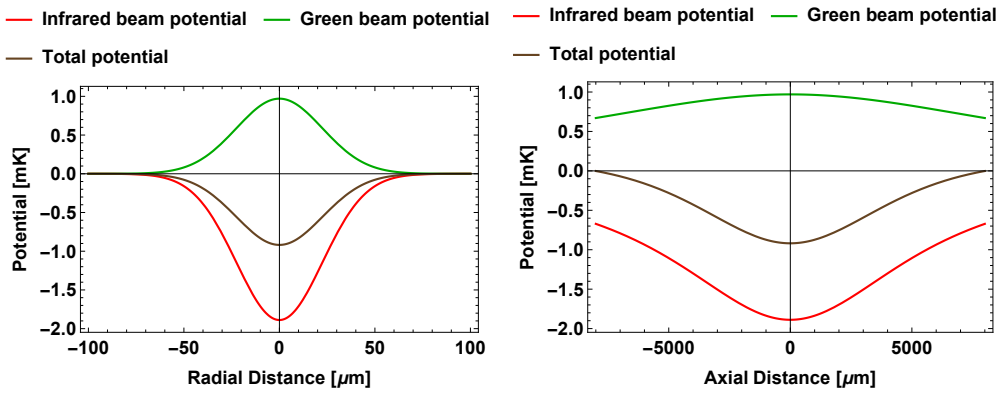

Figure 2.9: *Optical dipole potential experienced by Li atoms expressed in temperature units. The red (green) line is the trapping(antitrapping) potential generated by the infrared (green) beam, while in brown is represented the total potential simply given by their sum. In this image* $P_{IR} = 100W$, $P_G = 50W$, $w_{IR} = w_G = 45\mu m$, $M_J = 1/2$ *and the light polarization is* π.

As anticipated in Sec. 1.5.2, the trap is much steeper along the radial direction

than along the axial one[4].
In Fig. 2.10 I show the results of the potential experienced by Cr atoms in the absolute ground state ($M_{Ji} = -3$) for the same parameters of green and IR lights of Fig. 2.9.

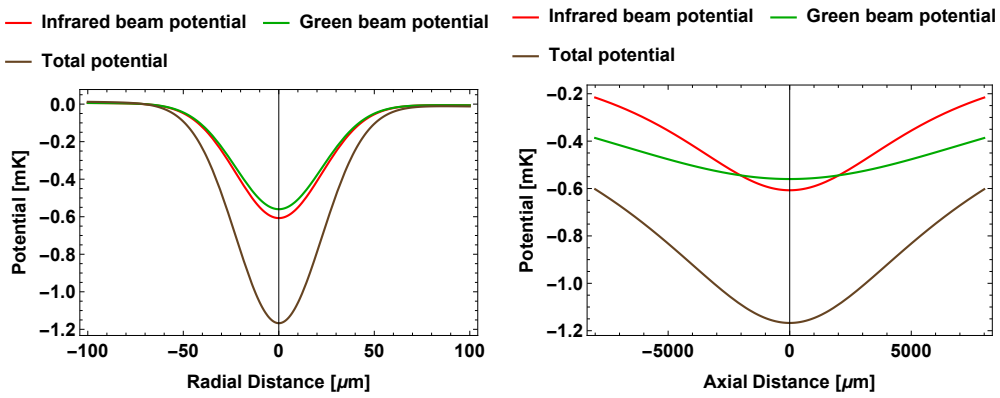

Figure 2.10: *Optical dipole potential experienced by Cr atoms expressed in temperature units. The red (green) line is the trapping potential generated by the infrared (green) beam, while in brown is represented the total potential. As in the other pictures,* $P_{IR} = 100W$, $P_G = 50W$, $w_{IR} = w_G = 45\mu m$ *and the lights are* π *polarized, but the initial level is* $M_J = -3$.

By varying the beams power, the ratio P_{IR}/P_G that allows to generate a dipole trap of the same depth for both Li and Cr atoms is found. Assuming $w_{IR} = w_G$, a π polarization and the initial state $M_J = -1/2$ and $M_J = -3$ for Li and Cr respectively, the ratio $P_{IR}/P_G \simeq 2.9$ provides the same trap depth for the two species. In particular, by considering $P_{IR} = 73W$, $P_G = 25.3W$ and $w_{IR} = w_G = 45\mu m$ the trap depth is about $0.9mK$.
The polarization of the laser light does not introduce relevant changes in the optical potential for the Li atoms, but from the simulation emerges that it plays a quite important role for the Cr atoms. In particular, by considering a σ_- (σ_+) polarization the resulting optical potential for Cr atoms in $M_J = -3$ is deeper (shallower) than that evaluated with a linear polarization of about 10% (20%). However, given that the ODT beam propagates on the xy plane, the presence of the Feshbach field that define the z direction as the quantization axis, allows only a π polarization (or a combination of $\sigma_+ + \sigma_-$) of the beams.

2.3.2 Gravitational sag

As we have already anticipated, when the beam powers are reduced during the evaporative and sympathetic cooling stages, the depth of the optical potential

[4]In the discussion of Sec. 1.5.2, the axial direction was $\vec{z}$. Within this section I prefer to refer to the experimental orientation and, therefore, the ODT axial direction is on the xy plane.

decreases and the effect of gravity becomes progressively more relevant [23, 30]. In particular, the gravitational field tilts the optical potential U_d along the vertical direction and, as a consequence, the effective trap depth is reduced. Moreover, the gravity introduces a shift in the position of the minimum of the potential z_{eq}, where the barycenter of each cloud is located. Indeed, by considering the harmonic approximation of the Gaussian potential, we have, for each species (i = Cr, Li) :

$$\frac{\partial U_d}{\partial z} = \frac{\partial}{\partial z}\left(\frac{1}{2} m_i \omega_i^2 z^2\right) = 0 \rightarrow z_{eq} = 0 \tag{2.6}$$

$$\frac{\partial (U_d + U_g)}{\partial z} = \frac{\partial}{\partial z}\left(\frac{1}{2} m_i \omega_i^2 z^2 + m_i g z\right) = 0 \rightarrow z_{eq} = -\frac{g}{\omega_i^2} \tag{2.7}$$

where m_i and ω_i are the atomic mass and the trap frequency of species i, U_d is the optical potential described as Eq. 2.5, and U_g is the gravitational potential.

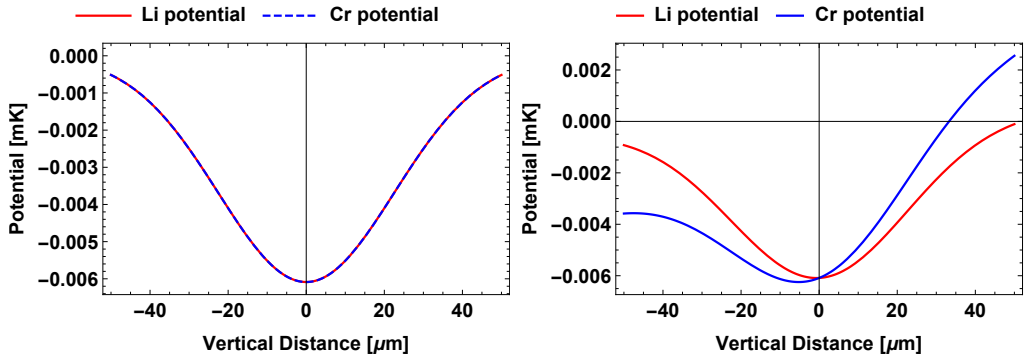

Figure 2.11: *Gravitational effect on the optical dipole potential. In this picture is shown the trend of the potential along the vertical direction by considering the following beam parameters:* $P_{IR} = 0.5W$, $P_G = 0.17W$, $w_{IR} = w_G = 45\mu m$ *and a linear polarization. The simulation is carried out with* $M_J^{Li} = -1/2$ *and* $M_J^{Cr} = -3$. *The intensity ratio of the beams, neglecting the gravitational effect, ensures the same potential for Li and Cr atoms (left panel), but including gravity the two potential minima shift one with respect to the other (right panel).*

From Eq. 2.7 one can notice that, if the beam parameters are such that the trap frequency is the same for both Li and Cr atoms ($\omega_{Li} = \omega_{Cr}$), the gravity introduces the same shift in the atomic clouds positions that are still overlapped. If instead one considers the case of equal potential $m_{Cr}\omega_{Cr}^2 = m_{Li}\omega_{Li}^2$, bearing in mind the mass ratio for the isotopes ^{52}Cr and ^{6}Li, i.e. $m_{Cr}/m_{Li} = 8.7$, the gravitational sag of Cr is 8.7 times larger than Li one (see Fig. 2.11).
One possible strategy to compensate this effect, which can substantially reduce the overlap between two atomic clouds at ultralow temperatures, consists in the

introduction of a magnetic field gradient applied along the z axis ($B(z) = bz$) [30]:

$$\frac{\partial(U_d + U_g + U_m)}{\partial z} = \frac{\partial}{\partial z}\left(\frac{1}{2}m_i\omega_i^2 z^2 + m_i g z + \mu_i b z\right) = 0 \rightarrow z_{eq} = -\frac{g + \mu_i b/m_i}{\omega_i^2} \quad (2.8)$$

where $\mu_i = \mu_B M_{Ji} g_J$, μ_B is the Bohr magneton and g_J is the total electronic g factor. In order to ensure a perfect overlap between the two cloud it is required that $z_{eq}^{Li} = z_{eq}^{Cr}$, from which it follows that

$$b = g\left(\frac{1}{\omega_{Li}^2} - \frac{1}{\omega_{Cr}^2}\right)\left(\frac{\mu_{Cr}}{\omega_{Cr}^2 m_{Cr}} - \frac{\mu_{Li}}{\omega_{Li}^2 m_{Li}}\right)^{-1} \quad (2.9)$$

Let us now consider the two cases previously studied, i.e. same frequency trap ($\omega_{Li} = \omega_{Cr}$) and same optical potential ($m_{Li}\omega_{Li}^2 = m_{Cr}\omega_{Cr}^2$). In the case of same frequency trap it is not required any magnetic gradient, because the shift induced by the gravity is equal for Li and Cr atoms. On the contrary, in the case of $m_{Li}\omega_{Li}^2 = m_{Cr}\omega_{Cr}^2$, by considering the initial (ground) states $M_{Ji}^{Li} = -1/2$ and $M_{Ji}^{Cr} = -3$, for which $\frac{\mu_{Cr}}{\mu_{Li}} = \frac{-6\mu_B}{-\mu_B} = 6$, and recalling that $\frac{m_{Cr}}{m_{Li}} = 8.7$ (and thus in this specific case $\frac{\omega_{Li}^2}{\omega_{Cr}^2} = 8.7$), we find that the magnetic gradient that cancels the relative sag is:

$$\begin{aligned} b &= \left(\frac{m_{Cr}/m_{Li} - 1}{|\mu_{Cr}/\mu_{Li}| - 1}\right)\left(\frac{m_{Li} g}{\mu_B}\right) = 1.54\left(\frac{m_{Li} g}{\mu_B}\right) \\ \left[&= \left(\frac{1 - m_{Li}/m_{Cr}}{1 - |\mu_{Li}/\mu_{Cr}|}\right)\left(\frac{m_{Cr} g}{6\mu_B}\right)\right] = 1.06\left(\frac{m_{Cr} g}{6\mu_B}\right) = 1.62\frac{G}{cm} \end{aligned} \quad (2.10)$$

Figure 2.12 shows how the potential changes for an applied magnetic gradient of $b = 4G/cm$, $b = 1.62G/cm$, $b = 0G/cm$ or $b = -4G/cm$. For this model, I chose quite low power value of $P_{IR} = 0.5W$ and $P_G = 0.17W$.
In order to appreciate the small effect that different magnetic field gradients have on Li atoms, Fig. 2.13 focuses on the potential profile for the sole Li in the $M_{Ji} = -1/2$ state, considering the same magnetic field gradients of Fig. 2.12, but lower beam powers ($P_{IR} = 0.25W$ and $P_G = 0.085W$).
We can see that the magnetic gradient which allows the compensation of the gravitational sag is $b = 1.62G/cm$, as predict analytically. The gradient chosen to balance the gravitational potential, being positive, pushes those atomic species that have $\mu_i > 0$ towards lower values of z. In our case, both Li and Cr ground state atoms have $gM_J < 0$ and the gradient lifts the atoms up against gravity. Additionally, from Eq. 2.10 one can notice how such a gradient is essentially the optimum one needed to cancel gravity for Cr (within 6%) and its application results, for Li, in an overall effective gravity of $\sim -0.54g$.

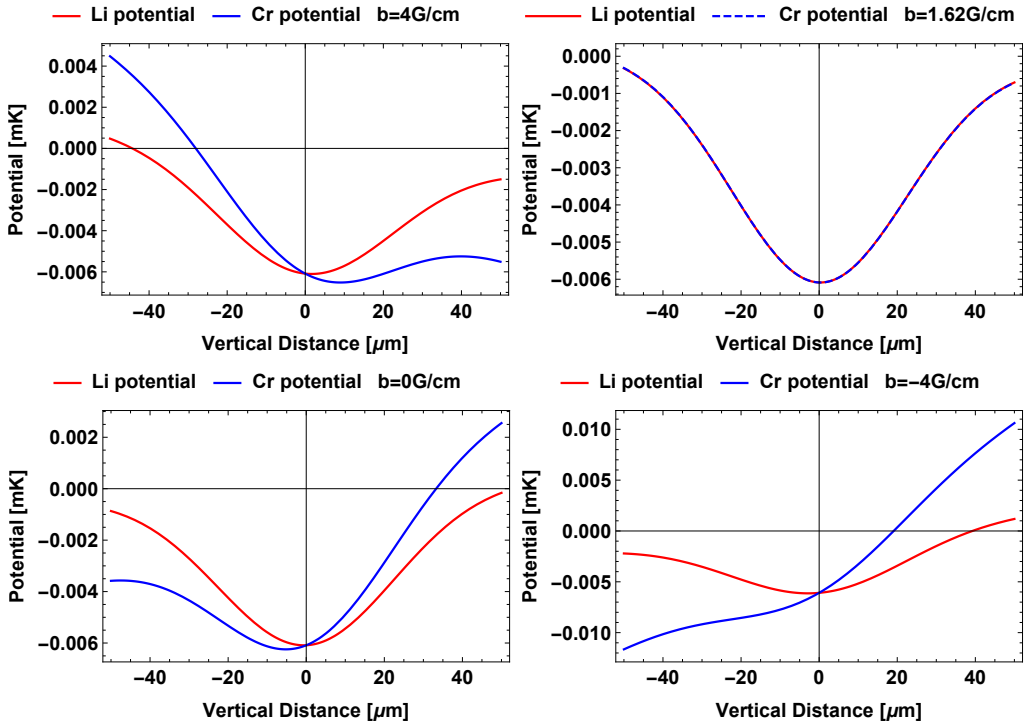

Figure 2.12: *Total potential (optical, gravitational and magnetic) along the vertical direction by considering the following beam parameters:* $P_{IR} = 0.5W$, $P_G = 0.17W$, $w_{IR} = w_G = 45\mu m$ *and a* π *polarization. In the simulation* $M_{Ji}^{Li} = -1/2$, $M_{Ji}^{Cr} = -3$. *The trends shown refer to a magnetic gradient of* $b = 4G/cm$, $b = 1.62G/cm$, $b = 0G/cm$ *and* $b = -4G/cm$.

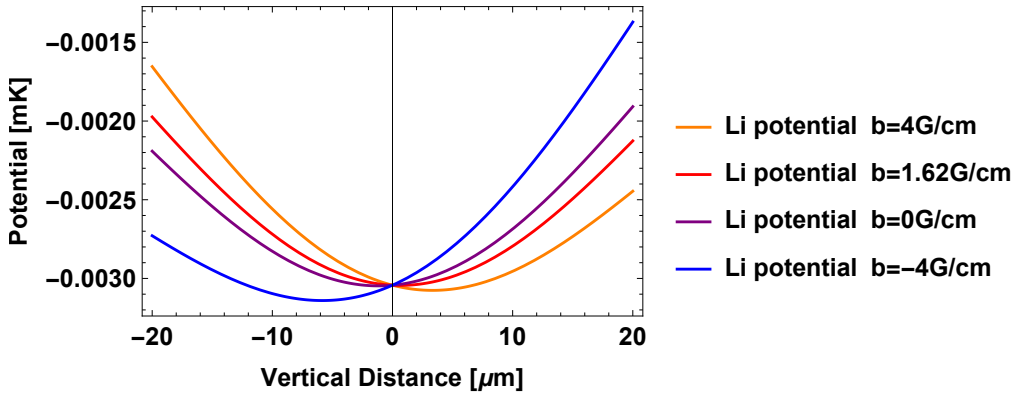

Figure 2.13: *Total potential (optical, gravitational and magnetic) along the vertical direction by considering the following beam parameters:* $P_{IR} = 0.25W$, $P_G = 0.085W$, $w_{IR} = w_G = 45\mu m$ *and a* π *polarization. This simulation focus on the Li atoms in the* $M_{Ji}^{Li} = -1/2$ *state. The trends shown refer to a magnetic gradient of* $b = 4G/cm$ *(orange),* $b = 1.62G/cm$ *(red),* $b = 0G/cm$ *(purple) and* $b = -4G/cm$ *(blue).*

Despite the compensation coils along the z direction switched in anti-Helmholtz configuration generate for $I = 3.5A$ a magnetic field gradient $\simeq 0.34G/cm$, thus not big enough to correct the relative gravitational sag for the Li and Cr atoms, their gradient can be combined with that produced by the MOT coils to efficiently overlap the two atomic clouds.

Chapter 3

Lithium cooling: MOT and D_1 gray molasses

This chapter provides an overview on the whole laser cooling and trapping protocols employed and optimized in this thesis to produce cold Lithium clouds.
We have already mentioned that the last step toward the realization of a degenerate Cr-Li mixture is the evaporative cooling in ODT. In order to optimize the loading in ODT and to make the evaporative cooling efficient it is important to increase the initial phase space density, i.e. increase the number of atoms and decrease their temperature (keeping the cloud volume constant). Therefore, after the stages of MOT and compressed MOT, we developed an additional cooling phase based on the gray molasses [33]. This routine has been already implemented in previous experiments and it greatly improves the phase-space density conditions and the loading efficiency in the ODT, enabling to produce large samples of degenerate Li mixtures [23].
In Sec. 3.1 I briefly describe the optical setup employed for the realization of the MOT and the gray molasses for Li atoms. The whole setup (the spectroscopy breadboard, the setup used for the amplification and the preparation of the lights, as well as the experimental cell) was already prepared at the beginning of my thesis work. Then, in Sec. 3.2 I report the experimental routine and results obtained after optimizing the MOT and the compressed MOT (CMOT) stages. I then focus on the optimization of optical molasses based on the D_1 line (3.3). In particular, after a short characterization of the Fano profile (previously described in Sec. 1.5.1), peculiar of this cooling technique, I discuss the effect of the compensation coils on this laser cooling stage. As we will see in Sec. 3.3.2, these coils, placed in Helmholtz configuration, allow to compensate spurious magnetic fields that detrimentally affect the optical molasses, limiting its efficiency both in terms of final temperature and atom number.

3.1 Optical setup

The optical setup that allows to collect the thermal Li atoms within the vacuum cell and to cool them through the MOT and the gray molasses techniques is quite complex. A block scheme of the optical setup main structure is shown in Fig. 3.1.

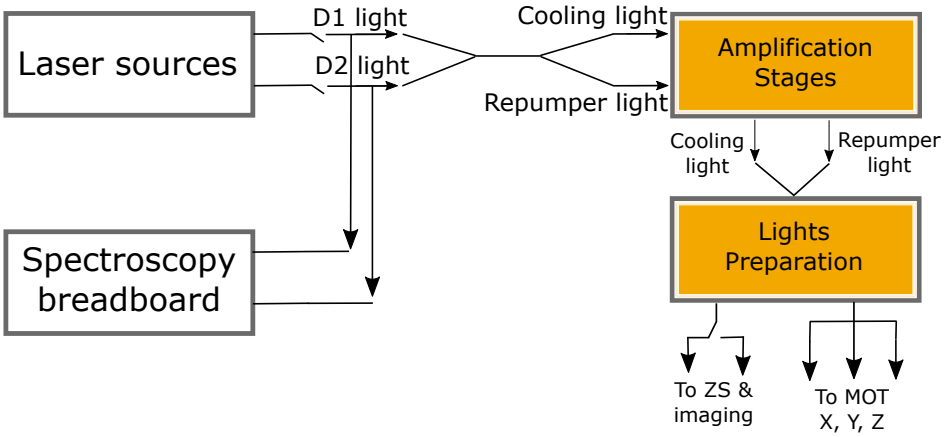

Figure 3.1: *Block scheme of the Li optical setup, taken from [15].*

The light sources are two commercial master lasers[1] at $671nm$, that provide the laser beams for the D_1 and D_2 atomic transition.
A small portion of each beam is sent to the breadboard dedicated to the laser locking setup. Both the lights are frequency locked by means of a modulation transfer spectroscopy (MTS) scheme[2]. This provides a dispersive signal, characterized by a zero crossing in correspondence of the match of the laser frequency with the atomic resonance. In our experiment, the D_2 and D_1 master laser are locked respectively to the line ${}^2S_{1/2}(|F=3/2\rangle) \rightarrow^2 P_{3/2}$ and ${}^2S_{1/2}(|F=3/2\rangle) \rightarrow^2 P_{1/2}$. The detailed description of our locking scheme is available in Sec. 3.2.2 of E. Neri's PhD thesis [15]. Here I only mention the presence of two double-pass acousto-optic modulators (AOMs, both sketched in Fig. 3.8 in the following section) that set the frequency detuning of the D_1 and D_2 master laser respectively at $-2\times100MHz$ and $-2\times140MHz$ with respect to the atomic resonance to which they relate.
The largest parts of the two master lasers lights, prepared with orthogonal polarization, are overlapped on a polarizing beam splitter cube, hence they follow the same optical path on the amplification and preparation breadboard. In order to select the desired light during the experimental routine, two AOMs (both working in single pass at $80MHz$ and depicted in Fig. 3.8) are placed before the beam

[1] Tapared Amplifier High Power Diode Laser (TA-Pro) produced by TOPTICA.
[2] The MTS technique is a standard saturated absorption spectroscopy with an additional modulation on one of the two counter-propagating beams.

splitter cube and act as fast shutters.
The beams are then separated into cooler and repumper lights, which are first amplified by two independent tapered amplifiers (BoosTA) and then recombined on a non-polarizing beam splitter (BS). The laser light runs therefore along two paths: one for the MOT beams and the other for the ZS and the imaging lights.
The optical setup referred to the orange boxes of Scheme 3.1, i.e. the amplification and preparation of the various lights, is depicted in Fig. 3.2.

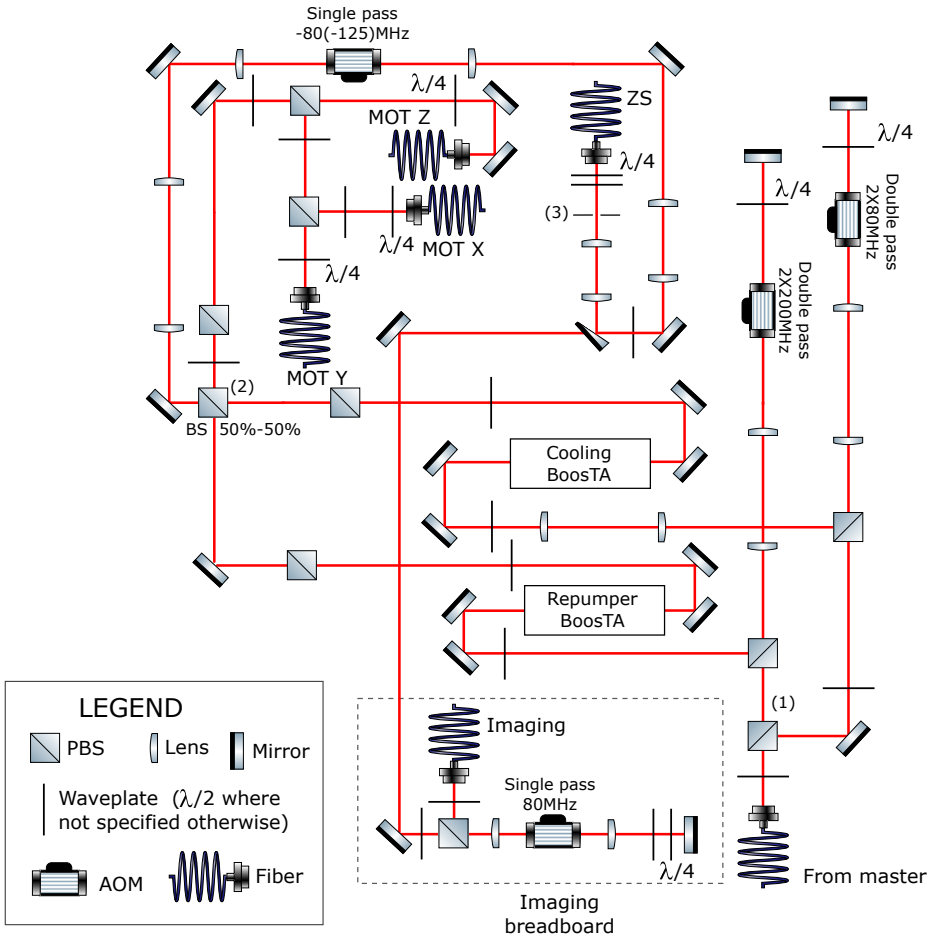

Figure 3.2: *Optical setup developed for the amplification and and the preparation of MOT, ZS and imaging lights.*

At the output of the optical fiber delivering the light produced by the master lasers, the $\lambda/2$ waveplate and the (1) polarizing beam splitter cube (PBS) allow to separate both the D_1 and D_2 lights into the cooler and repumper beams with a $\sim 50-50$ ratio. Both the cooler and the repumper beams pass through a double pass AOMs centered, respectively, at $80MHz$ and $200MHz$. By accurately adjusting the AOMs frequency, it is possible to set a relative detuning between cooler and repumper light of about $228MHz$, that is exactly the hyperfine separation of the level $^2S_{1/2}$ (see Fig. 1.2).

The lights are then independently injected into two Toptica BoosTAs and, after being amplified, they are recombined on a $50-50$ non-polarizing beam splitter cube (2). The transmitted beam is further split into the ZS light and the imaging one, while the reflected beam is exploited for the three MOT beams (MOT X, MOT Y and MOT Z).
Along the ZS and imaging path a single pass AOM is placed: when it is set to about $-80MHz$ the light is coupled into the ZS fiber. If instead it is set to $-125MHz$ the beams is injected into the imaging fiber. A shutter (3) installed in front of the ZS fiber avoids the presence of spurious light into the ZS beam during the imaging routine.
Fig. 3.2 also shows the imaging breadboard. Before entering into the imaging fiber, the beam passes through a double-pass AOM which allows to compensate the previous AOM shift and to tune the light frequency.

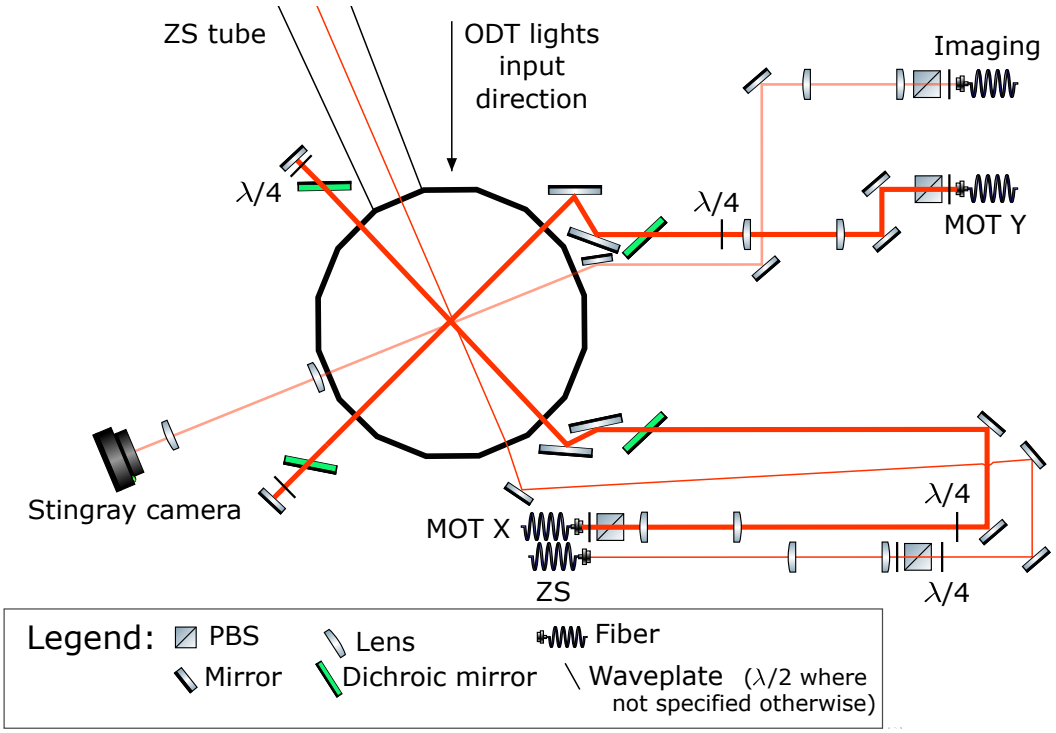

Figure 3.3: *Experimental cell and optical setup exploited for the ZS and the MOT beams. In light red are reported the imaging and the ZS beams, in red are depicted the MOT lights. The image is taken and adapted from Ref. [15]: here I represent only the Li beam paths, together with the dichroic mirrors (in green) onto which Li and Cr lights recombine. In this picture, the vertical MOT beams are not reported.*

The ZS light and the imaging one, as well as the three MOT beams, are brought onto the vacuum table, where the experimental cell is installed. The optical setup on the vacuum table, except the vertical MOT beam path (that is similar to those

designed for the in plane MOT lights), is depicted in Fig. 3.3.
The fiber collimators yield an output beam waist of about $1mm$, which is magnified by means of a $1 \div 6$ telescope. The MOT beams enter in the experimental cell through large viewports ($CF40$ in the plane, $CF100$ along z) and they are retroreflected with a mirror. Typical power values for the D_2 light are $20mW$ and $15mW$ respectively for the cooling and the repumper light on the x-y plane, whereas along the vertical direction, a power of about $15mW$ ($10mW$) is employed for the cooler (repumper) light.
Also the ZS beam waist is magnified with a $1 \div 3$ telescope, which focuses the light on the Li oven. The total power is set by a waveplate and a PBS placed after the fiber output, and it is split between cooler and repumper with a 3:2 ratio.
In Fig. 3.3 I also show the absorption imaging path. The imaging beam has a power of $\sim 2mW$ and a beam waist of $\sim 1cm$. After hitting the atoms at the center of the chamber it is sent to a Stingray camera. A $2 \div 1$ telescope yields a demagnification of 2, which is well suited to characterized the Li clouds collected in the MOT.

3.2 Experimental routine and results of MOT and CMOT stages

At the beginning of my thesis, a MOT of ^{6}Li atoms was already realized and characterized. During my work I participated in the optimization of the two stages of CMOT and in the realization and characterization of the D_1 gray-molasses.
For the data acquisition a Stingray camera is used. The number of cold atoms and their temperature are determined by analyzing the cloud image after variable time of flight .

3.2.1 Absorption imaging

Our imaging system is a CCD camera (Stingray F-145B) composed by a matrix of 1038×1388 square pixels of size $6.45\mu m$. The telescope before the Stingray (depicted in Fig. 3.3 and already mentioned in the previous section) provides a magnification of $M = 0.5$. With the CCD camera we can directly observe the density distribution of the atomic clouds, from which it is possible to extrapolate the temperature of the atoms.
The atomic cloud image is obtained by acquiring three separate pictures: the first detects the cold atoms absorbing the imaging light and the second, taken a few tens of ms after, records the image of the light with no atoms. An additional third image is then taken in order to quantify the background light and it is taken with no atoms nor imaging light.

The atomic density in the CCD plane is given, in the case of $I_l \ll I_{sat}$, by [34]:

$$n(x,y) = \frac{A}{\sigma_{abs} M^2} \ln\left(\frac{I_l(x,y) - I_{bg}(x,y)}{I_a(x,y) - I_{bg}(x,y)}\right) \tag{3.1}$$

where I_a and I_l are the intensity patterns with and without atoms respectively, and I_{bg} is the background intensity distribution. A is the area of a single pixel and σ_{abs} is the resonant absorption cross-section, which for a transition characterized by a wavelength λ_0 reads [32] $\sigma_{abs} = \frac{3\lambda_0^2}{2\pi}$.
Assuming an initial Gaussian distribution of the cold atoms in MOT, it is expected that, once the beams and the magnetic fields are switched off, the initial Gaussian distribution expands into a broader one. Taking a destructive absorption image both *in situ* or during the free expansion, the atomic distribution is therefore fitted, along each direction, with a Gaussian function, as it is possible to see in Fig. 3.4.

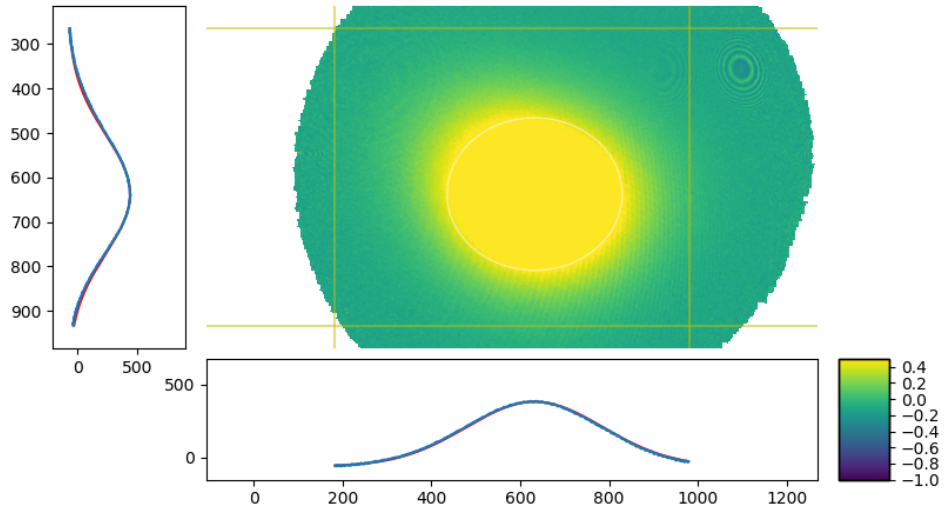

Figure 3.4: *Example of destructive absorption image of the* ^6Li *MOT obtained by means of the Stingray. The atomic cloud is fitted with a* $2D$ *Gaussian distribution. The cloud outlined in this pictures is after the C-MOT stages and it is taken after a free expansion of* $2ms$.

The fit provides the total atom number. Moreover, by monitoring how the cloud expands in different time of flight (t), it is possible to evaluate the atoms temperature by means of the expression [16, 35, 36]:

$$\sigma(t) = \sqrt{\sigma_0^2 + \frac{k_B T}{m} t^2} \tag{3.2}$$

where σ_0 is the width of the distribution *in situ*, namely at zero expansion time, k_B is the Boltzmann constant and m is the atoms mass.

3.2.2 MOT and compressed MOT

With a combination of ZS and MOT techniques a cold ^{6}Li cloud is realized. An iterative optimization procedure, thoroughly described in Sec. 4.1 of Ref. [15], allows to find the best experimental loading settings that provide a MOT composed by $N \sim 4 \times 10^8$ atoms at a temperature of the order of $1-2mK$.
Our MOT loading settings are:

- Loading time = $7s$
- MOT current = $45A \rightarrow$ MOT gradient=$23G/cm$
- ZS current = $2A$
- MOT beams power: MOT X=$30mW$, MOT Y=$27mW$, MOT Z=$25mW$ (cooling and repumper laser ratio $3 \div 2$)
- ZS beam power= $35mW$ (cooling and repumper laser ratio $3 \div 2$)
- MOT detunings: $\delta_{cool} = -7\Gamma$; $\delta_{rep} = -8\Gamma$
- ZS beam detuning $\sim -22\Gamma$

In order to reduce the atoms temperature, a two-step compressed MOT (CMOT) stage is applied. As outlined in Fig. 3.5, the detuning ($\delta_{cool,rep}$) and intensity ($I_{cool,rep}$) of both the cooling and repumper light are gradually decreased.
The first CMOT stage (CMOT-1) lasts 100ms, during which the intensity is reduced to the 70% for the cooling beams and 14% for the repumper ones of their initial values. During this stage the detuning is decreased to -4.5Γ and -6Γ respectively for the cooling and the repumper lights.
After this first CMOT stage, we apply a second shorter one (CMOT-2) lasting $3ms$, in which the intensities and the detunings are further and more strongly reduced: $I_{cool} = 5\%$, $I_{rep} = 4\%$, $\delta_{cool} = -1.5\Gamma$ and $\delta_{rep} = -2.5\Gamma$.
Typical TOF measurements of the atomic cloud temperatures obtained after the single CMOT-1 and after both CMOT-1 and CMOT-2 stages are shown in Fig. 3.6. The uncertainty is evaluated as the standard deviation of several data acquisitions. At the end of the CMOT-2 the cloud has a typical temperature of about $T = 500\mu K$. Lower T values, closer to the Doppler limit, could be attained, but only at the price of a significant reduction of the atomic population.
During the CMOT-1 stage the cloud is adiabatically transferred from the MOT coils quadrupole to the one made by the Feshbach coils, through a $50ms$ long linear ramp of the coils currents. While the gradient of the two quadrupole is

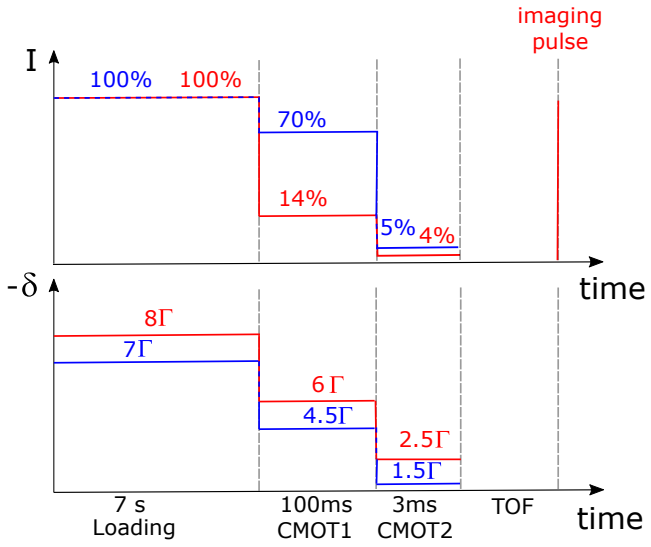

Figure 3.5: *Loading routine of MOT and CMOT stages. Here are illustrated the reduction of the lights intensity and their detunings. The repumper light is represented in red, while the cooling one in blue. Moreover in figure appears the imaging pulse after a variable time of flight (TOF).*

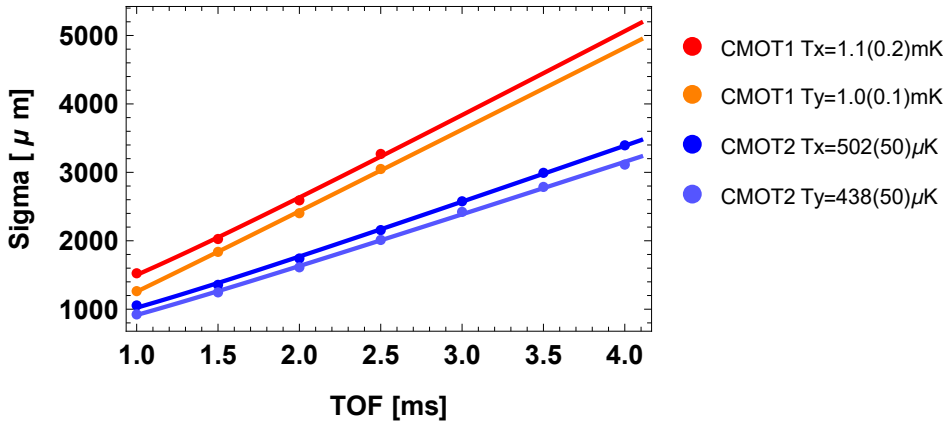

Figure 3.6: *Time of flight expansion measurement, for the horizontal $\tilde{\sigma}_x$ and vertical $\tilde{\sigma}_y$ direction, taken at the end of the CMOT-1(CMOT-2) routine for the red-orange(blue-light blue) dots and lines,which correspond respectively to the experimental data and to the fit.*

identical, hence the cloud is not affected nor modified, this transfer is important to guarantee a fast switch off of the magnetic fields after CMOT-2. Indeed, owing to their large inductance (see E. Neri's PhD thesis for details) the MOT coils field can be turned off completely only after a few ms. In contrast, the Feshbach coils quadrupole field can be turned off within a few $100\mu s$, enabling to implement the D_1 optical molasses stage immediately after the end of the CMOT-2 stage.

3.3 D_1 gray molasses

As already explained in Sec. 1.3.1 temperatures below the Doppler limit ($T_D = \frac{\hbar\Gamma}{2k_B}$) are not achievable by means of the MOT and CMOT techniques. To cool the atomic cloud below this value, that for Li atoms is $140\mu K$, a gray molasses stage is required.
For the implementation of this cooling technique, we followed the procedure successfully devised and discussed in Ref. [23]. The gray molasses is based on the D_1-line, rather than the D_2-line, whose small hyperfine splitting renders the sub-Doppler mechanism completely inefficient. The Λ structure (Sec. 1.5.1 and in particular Fig. 1.10) required for the realization of the molasses (and more specifically for the VSCPT process) is composed by the ${}^2S_{1/2}(|F = 1/2\rangle)$, ${}^2S_{1/2}(|F = 3/2\rangle)$ and ${}^2P_{1/2}(|F' = 3/2\rangle)$ levels.

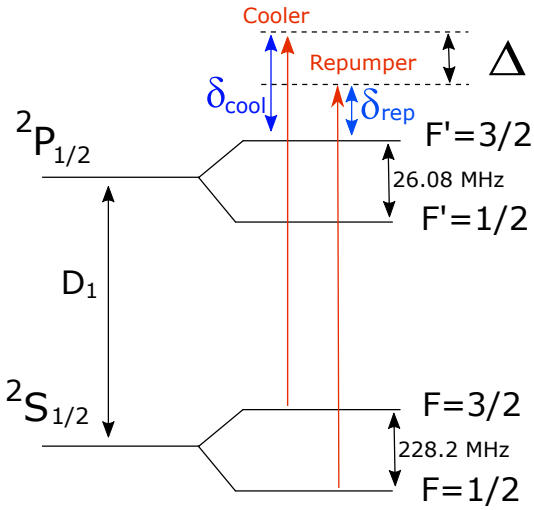

Figure 3.7: *Sketch of the laser configuration on the D_1 transition on ${}^6Li$. The red arrows indicate the cooling and repumper beams, both blue-detuned with respect to the atomic transition of respectively δ_{cool} and δ_{rep}. In figure, Δ represents the relative detuning $\delta_{rep} - \delta_{cool}$.*

In particular, an overview of the laser configuration used for the D_1 gray molasses is shown in Fig. 3.7: both the cooling and the repumper beams frequencies are blue detuned with respect to the atomic transitions to which they refer, i.e. $|F = 3/2\rangle \rightarrow |F' = 3/2\rangle$ for the cooler and $|F = 1/2\rangle \rightarrow |F' = 3/2\rangle$ for the repumper. The relative detuning is $\Delta = \delta_{rep} - \delta_{cool}$ and the Raman condition corresponds to $\Delta = 0$.
As already discussed, the gray molasses mechanism leads to a temperature trend characterized by a Fano profile of typical width $\ll \Gamma$. The temperature features the minimum in correspondence of $\Delta = 0$. It is therefore essential to carefully determine the behavior of the atom number and the temperature as a function

of Δ.
Fig. 3.8 shows a sketch of the optical setup, focusing on the AOM and on the frequency shift they provide.

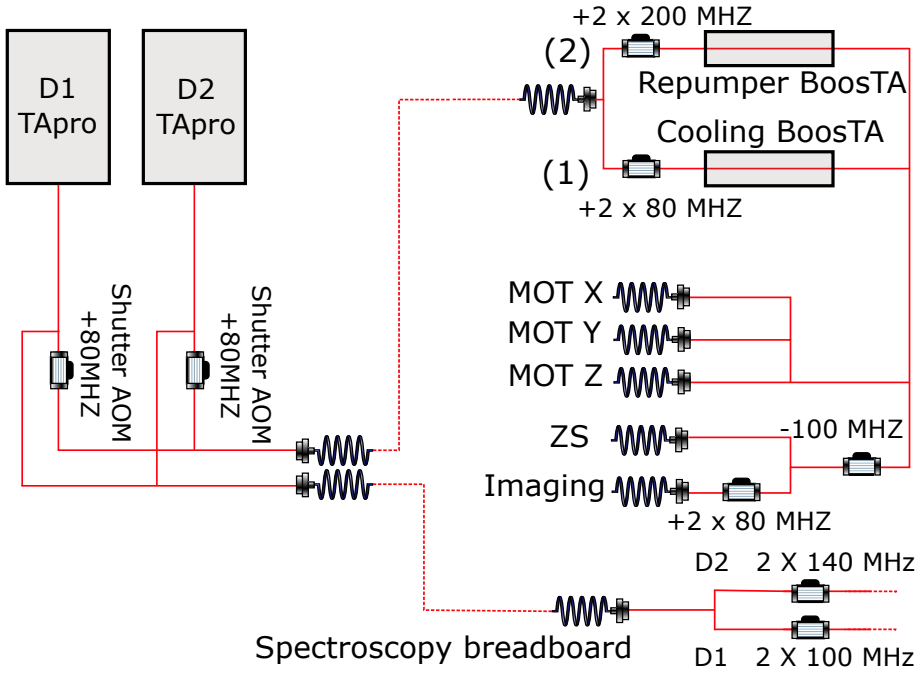

Figure 3.8: *Optical setup showing the AOM and their frequency settings during the D_1 routine.*

By changing the frequency shift produced by the AOM acting on the cooler (1) or on the repumper (2) beam (depicted in figure before the tapered amplifiers), it is possible to accurately tune Δ with a frequency resolution[3] of $0.2MHz$. In this way it is possible to scan a range of detunings of $\sim 8\Gamma$.
Fig. 3.9 outlines the resulting frequency detuning for the cooling and the repumper beams operating on the D_1.
As one can see both in Fig. 3.8 and Fig. 3.9, the laser is locked at a frequency that is red detuned of about 180 MHz with respect to the $|F = 3/2\rangle \rightarrow |F' = 1/2\rangle$ transition. Then, the beam, before being split into cooling and repumper, is shifted to the blue by $80MHz$ by means of the "shutter" AOM. As already discussed, the final detunings δ_{cool} and δ_{rep} are determined by the double-pass AOMs before the tapered amplifier.

[3]The frequency resolution of the AOM is $0.1MHz$, but the double pass configuration leads to a resolution of $0.2MHz$ for Δ.

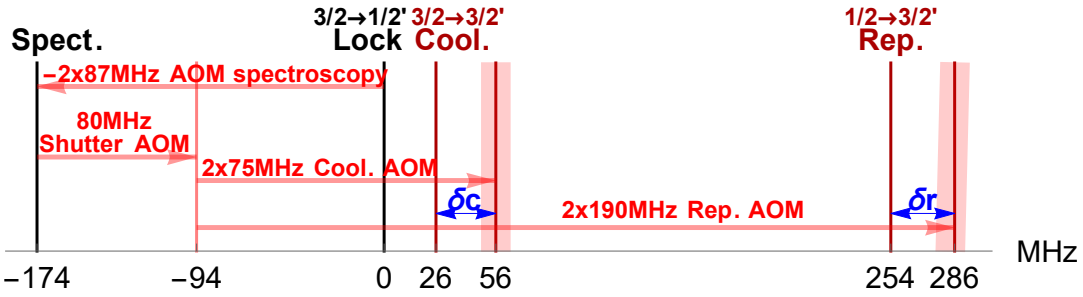

Figure 3.9: *Sketch of the frequency detuning for the D_1 laser beams. The light red arrows show the AOM frequency shift, while the blue arrows refer to the consequent δ_{cool} and δ_{rep} as defined in Fig. 3.7. The light red shadows indicate the possibility of thoroughly tune the final detuning δ_{cool} and δ_{rep} by changing the shift provides by Cool. and Rep. AOM.*

3.3.1 Experimental results

As discussed in Ref. [25] and already experimentally observed, see Ref. [23], a characteristic feature of the D_1 gray molasses is the appearance of a sub-natural linewidth Fano profile in the Δ-dependence of the temperature of an atomic cloud.

In our experimental routine the gray-molasses stage on ^{6}Li atoms starts after the CMOT stages described in Fig. 3.5. The cloud temperature is $\sim 500\mu K$ and the initial atom number[4] is $N_0 \sim 1.6\times10^8$. The quadrupole field and the D_2 lights are then switched off and, after $0.4ms$, the D_1 beams, both cooling and repumper, are switched on. A first characterization allowed to pinpoint the best settings of intensity (I_{cool} and $I_{rep} \ll I_{cool}$), detuning (δ_{rep} and δ_{cool}, both blue detuned) and time duration. In particular, after analysing various configurations, I identify the following best parameters: $I_{cool} = 2.75 I_{sat}$, $I_{rep} = 0.045 I_{cool}$ and $t_{D_1} = 0.6ms$. Even though the t_{D_1} value is quite small, for longer gray-molasses time the atomic temperature increases and the relative atom number N/N_0 decreases.

In Fig. 3.10 I show the trends of the number of captured atoms $\frac{N}{N_0}$ (blue dots) and the cloud temperature (red dots) as a function of the relative detuning $\Delta = \delta_{rep} - \delta_{cool}$, by considering a fixed value $\delta_{cool} = 5.3\Gamma$. When $\delta_{rep} = 5.1\Gamma$, i.e. for a relative detuning $\Delta = -0.2\Gamma$, very close to the Raman condition, the minimum temperature $T \simeq 50\mu K$ is measured.

The temperature is evaluated by simply comparing the size of the atomic distribution at two different TOF of $4ms$ and $6ms$.

The number of atoms is taken after $2ms$ of free expansion and from the pic-

[4]The atom number and the cloud temperature after the CMOT-2 phase is obtained through absorption imaging resonant with the $|F = 1/2\rangle \rightarrow |F' = 3/2\rangle$ transition, after $20\mu s$ of hyperfine pumping in the $|F = 1/2\rangle$ level.

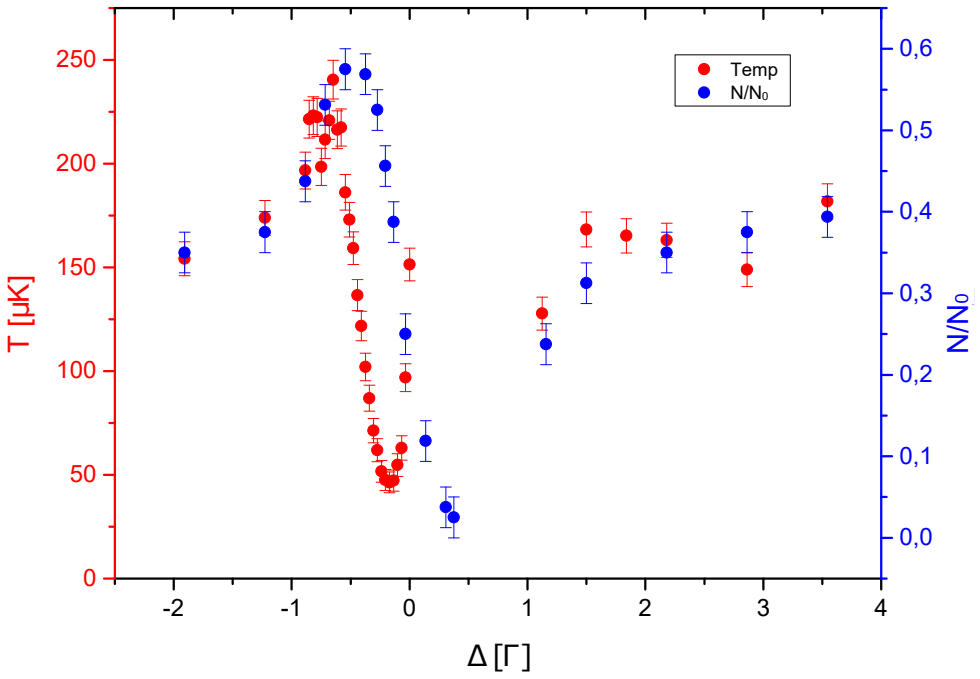

Figure 3.10: *Cloud temperature (red dots) and captured atoms ratio (blue dots) of the* ^{6}*Li cloud after the* D_1 *gray molasses stage. The results are reported as a function of the relative detuning* Δ*, for a fixed* $\delta_{cool} = 5.3\Gamma$*. The lack of data in the range* $0.5\Gamma - 1\Gamma$ *is due to a quick heating process of the cloud for these detuning values.*

ture above one can notice that for $\Delta = -0.2\Gamma$ only 40% of the CMOT-2 atoms are cooled with the gray molasses technique, namely $N \sim 6.5 \times 10^7$. The maximum measured value of $N/N_0 \simeq 0.55 \div 0.6$ (corresponding to $N \sim 9 \times 10^7$) occurs for $\Delta \simeq -0.5\Gamma$.
The atom number ratio reported in Fig. 3.10 is evaluated by means of absorption imaging resonant with the $|F = 1/2\rangle \rightarrow |F' = 3/2\rangle$, but with no hyperfine pumping because it would detrimentally affect the gray molasses[5]. As a consequence, $\frac{N}{N_0}$ is systematically underestimated.

To properly determine the true number (N_{true}) of Li atoms cooled in the molasses an hyperfine pumping in the $|F = 1/2\rangle$ level is carried out. Figure 3.11 shows the trend of N as a function of the hyperfine pumping duration, for different Δ values: $\Delta = 2.2\Gamma$ (red dots), $\Delta = -0.2\Gamma$ (blue dots) and $\Delta = -0.5\Gamma$ (orange dots). All these data are acquired with a fixed value of $\delta_{cool} = 5.3\Gamma$ and a time of flight of $2ms$.
The number of atoms increases with increasing hyperfine pumping duration, but

[5]During the gray molasses the atoms occupy the dark state $|\Psi_D\rangle$ that is a superposition of both $|F = 1/2\rangle$ and $|F = 3/2\rangle$. Therefore, an eventual hyperfine pumping on the $|F = 1/2\rangle$ would decrease the gray molasses performance.

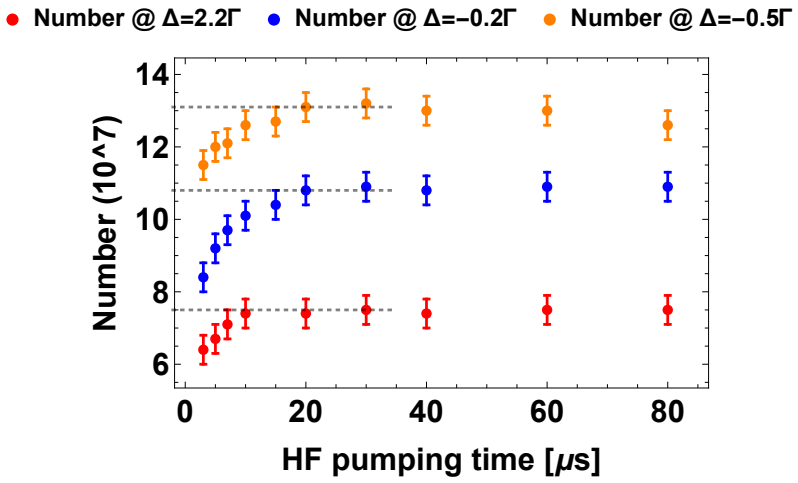

Figure 3.11: *Number of ^{6}Li atoms composing the gray molasses measured after an hyperfine pumping of variable duration. The data correspond to $\Delta = 2.2\Gamma$ (red dots), $\Delta = -0.2\Gamma$ (blue dots) and $\Delta = -0.5\Gamma$ (orange dots). The dashed lines represent the saturated atom number N_{true} for each data set.*

it saturates to N_{true} in $\sim 20\mu s$.
By comparing the saturated number N_{true} obtained from this latter measure with that one provides by Fig. 3.10, we can observe that the atom number recorded with no hyperfine pumping corresponds to $\frac{N}{N_{true}} = \frac{6.5\times10^7}{10.7\times10^7} \sim 60\%$ and $\frac{N}{N_{true}}\frac{9\times10^7}{13\times10^7} \sim 70\%$, respectively for $\Delta = -0.2\Gamma$ and $\Delta = -0.5\Gamma$.
Therefore, it is possible to conclude that the true relative number is $\frac{N_{true}}{N_0} \simeq 67\%$ in correspondence of the lowest temperature value, and it reaches a maximum value of $\frac{N_{true}}{N_0} \simeq 80\%$ at $\Delta = -0.5\Gamma$. These results are in good agreement with those previously reported in Ref. [23].

3.3.2 Optimization of D_1 cooling with compensation coils

Even though the experimental results shown in Fig. 3.10 are consistent with what reported in Ref. [23], the observed large shot-to-shot fluctuations in temperature and atom number, together with the impossibility to apply the D_1 molasses beyond $0.6ms$ without losing substantially in phase-space density, strongly suggest the presence of some residual magnetic field. To this end, I tested the performances of the D_1 cooling stage once a non-zero compensation field was applied by means of the compensation coils setup described in Chapter 2. Examples of such characterization are reported in Fig. 3.12, for $I_{cool} = 2.75 I_{sat}$, $I_{rep} = 0.045 I_{cool}$ and $\Delta = -0.2\Gamma$.
In particular, in the left panels (a and b) I show how the atomic cloud temperature (upper panel) and the atom number (lower panel) change as a function of

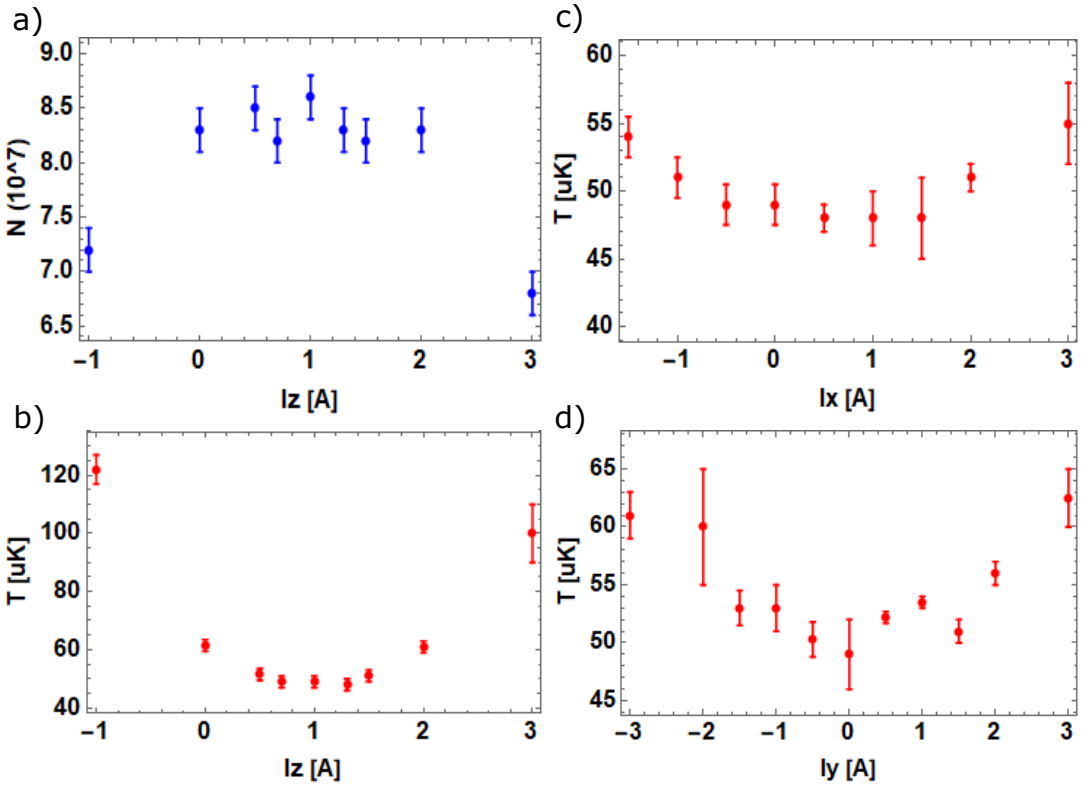

Figure 3.12: *Optimization of the gray molasses by means of the compensation coils. The temperature of the atoms (red dots, b panel) decreases by varying the current flowing in the z coils, while the number of atoms (blue dots, a panel) composing the molasses does not significantly change around the optimum value of* $1A$*. In the right panels is depicted the temperature analysis by varying the current in the x coils (c) and in the y coils (d). The error bars are the maximum deviation from the averaged temperature considering different data set.*

the current value flowing in the vertical compensation coils. Starting from an initial molasses characterized by $T \simeq 60\mu K$, it is possible to decrease its temperature (see Fig. 3.12a) without losing atoms (Fig. 3.12b). By setting $1A$ in the z-coils we measure $T = 50\mu K$ and $N \sim 8.4 \times 10^7$. The temperature is calculated by comparing the size of the Gaussian atomic distribution after $4ms$ and $6ms$ of time of flight, and N is measured by means of an absorption imaging on the $|F = 1/2\rangle \rightarrow |F' = 3/2\rangle$ without hyperfine pumping.

In the right panels of Fig. 3.12 is shown the behavior of the cloud temperature measured by changing the current in the x coils (upper panel) and y coils (lower panel). The data of the x coils are taken by setting $1A$ for the z coils current. Similarly, the data relative to the y coils are taken by setting $I_{zcoils} = 1A$ and $I_{xcoils} = 0.5A$.

This characterization allowed to pinpoint the optimum current configuration and the consequent magnetic field generated by the compensation coils: $I_{zcoils} =$

$1A \rightarrow B_z \simeq 0.6G$, $I_{xcoils} = 0.5A \rightarrow B_x = 0.1G$ and $I_{ycoils} = 0$.
The compensation of the residual magnetic field is confirmed by the characterization of the gray molasses duration: indeed an optimum value $> 0.6ms$ was found in this case. In Fig. 3.13 it is shown the trend of the atom number (blue dots) and of the temperature (red dots) as a function of t_{D_1}.

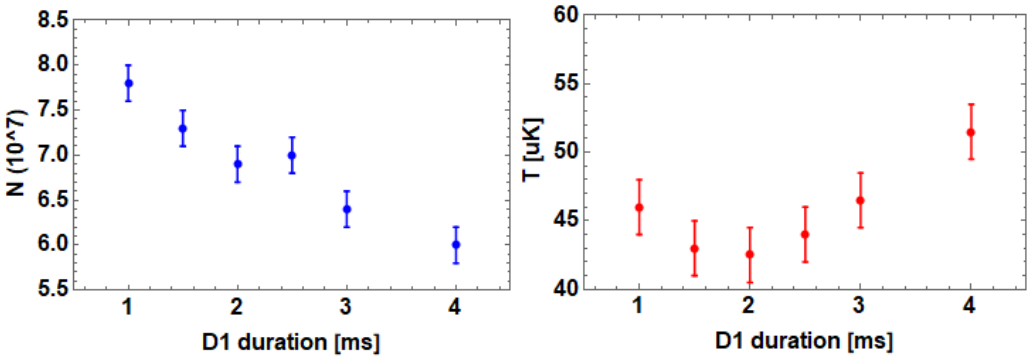

Figure 3.13: *Time characterization of D_1 gray molasses. The blue (red) dots represent the atom number (temperature) as a function of the switching off of the D_1 light. The number is taken after $2ms$ of TOF, while the temperature is evaluated by the size of the atomic cloud after $4ms$ and $6ms$ of TOF.*

The lowest temperature appears for $t_{D_1} = 2ms$, in agreement with previous experiments, see Ref. [23]. In this configuration $N \simeq 6.9 \times 10^7$, measured, as already emphasized, without hyperfine pumping. From previous characterizations, we can assume that for $\Delta = -0.2\Gamma$ the absorption imaging with no hyperfine pumping provides $\sim 60\%$ of the total atom number. It is, therefore, possible to calculate $N_{true} = 1.1 \times 10^8$ and $\frac{N_{true}}{N_0} \simeq 61\%$.
Figure 3.14 shows the temperature measurement of the D_1 gray molasses in this optimized configuration. The fit yields $T_x \simeq T_y \simeq 42\mu K$.

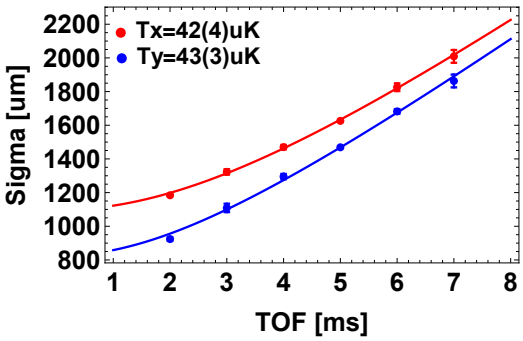

Figure 3.14: *Temperature of Li atoms in the D_1 gray molasses after the compensation of the residual magnetic field and the optimization in time. In red and blue dots is reported the experimentally expansion (and the corresponding fit) of the atomic cloud along the x and the y direction of the imaging camera.*

The same measurement, keeping the same settings and duration but with the compensation coils switched off, leads to a temperature of about beyond $T = 100\mu K$.

Chapter 4

Chromium MOT and simultaneous loading of double-species ^{6}Li-^{52}Cr MOT

We have already stressed the difficulty of achieving the quantum degeneracy of a ^{53}Cr sample. So far, only one laboratory worldwide has been successful in 2015 [37] in realizing small ($< 10^3$ atoms) ^{53}Cr Fermi gases at moderate degeneracy by means of sympathetic cooling with the bosonic isotope (^{52}Cr).
In our experiment we plan to independently create two MOTs of Li and Cr atoms and then to simultaneously load them into the ODT. Successively, we plan to bring Cr to quantum degeneracy by means of a sympathetic cooling stage, where a binary mixture of Li atoms equally populating the two lowest Zeeman atomic states will act as a coolant for Cr atoms. To this end, it is essential to investigate the interspecies Li-Cr collisional properties, completely unknown so far.
Before examining the fermionic ^{53}Cr isotope in the cold regime, a preliminary characterization of the more known bosonic ^{52}Cr MOT has been performed.
Despite I have not been involved in the design of the setup allowing for the realization of the Cr MOT, nor to its first optimization and characterization, during the last part of my thesis work I contributed to the investigation of the metastable state D_3 and D_4 of the bosonic isotopes. Moreover, I participated to the first experimental loading of a double-species MOTs of Cr and Li, and to the characterization of the D_3 and D_4 state lifetimes in presence of Li atoms.
In this Chapter I summarize the experimental routine that allows to perform these studies. In particular, in Sec 4.1 I briefly describe the optical scheme exploited for the main cooling transitions of both ^{52}Cr and ^{53}Cr and for the additional red repumper lights. Sec. 4.2 includes the experimental results attained with the ^{52}Cr setup, with special focus on the characterization of the metastable states (4.2.1) and on the loading of the very first double-species Li-Cr MOT (4.2.2).

4.1 Experimental setup

Fig. 4.1 shows a block scheme of the optical setup employed for the achievement of a cold atomic Cr cloud.

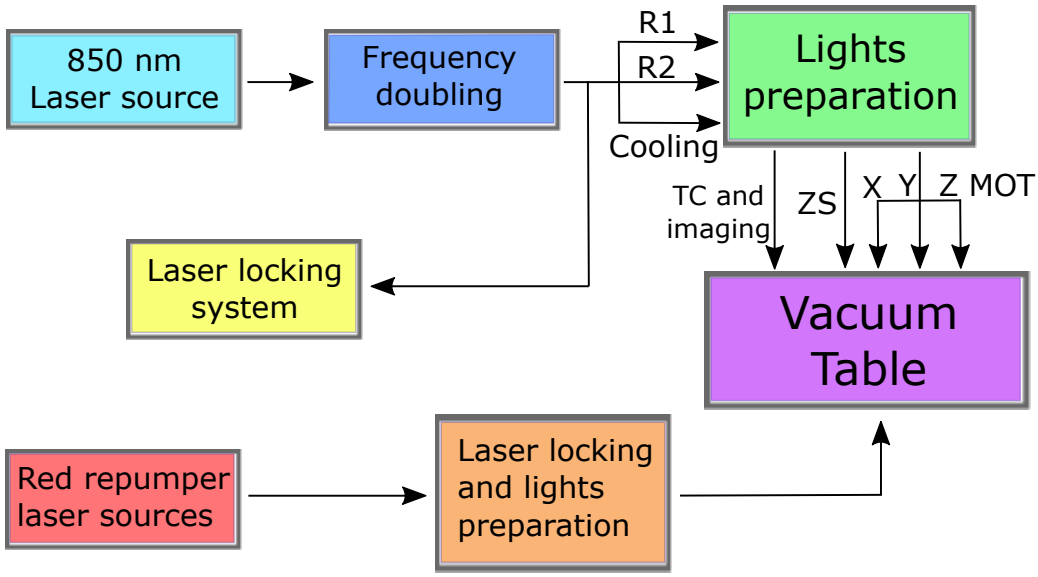

Figure 4.1: *Block scheme of the Cr optical setup.*

The blue light at $425nm$ required for the cooling transition is obtained from a $850nm$ laser source that is subsequently injected into a duplication cavity (light-blue and blue boxes). The master source is a Toptica DL, providing an output power of about $35mW$, plus a home-made TA system which increases the power up to $2W$. The combined action of a collimator and a cylindrical telescope makes the beam collimated with negligible ellipticity and, after passing through an optical isolator, it is injected into the home-made frequency doubling cavity based on a bow-tie configuration. Here the frequency doubling stage is obtained by a BBO crystal which provides the second harmonic generation process. The cavity is locked with a Pound-Drever-Hall (PDH) technique [38], and yields an output beam of $\sim 600mW$ at $425nm$. The light is then split into two optical paths, one devoted to the locking system (yellow block) and the other to the preparation of the trapping and cooling lights (green box).
The atomic spectroscopy cell is a commercial hollow cathode lamp and the locking system is composed by a MTS scheme, as for the Lithium atoms. In order to manipulate both the fermionic and the bosonic isotopes, the light can follow two different optical paths. So, the locking point can be set by two different AOM setups: the ^{52}Cr locking point is defined by a double pass AOM at $-2\times95MHz$ from the boson atomic resonances, whereas the ^{53}Cr locking point is set at $+90MHz$ from the same reference by means of a single pass AOM.

Regarding the light preparation (green block), in order to provide also the manipulation of the ^{53}Cr isotope, the beam is divided into the cooling light and the two repumpers. Indeed, as we can see in Fig. 1.3, while for the bosonic ^{52}Cr the cooling transition is closed, for the fermionic one two repumper lights (R_1 and R_2) are needed. The repumper path is composed by two double pass AOMs in a cascade configuration. The R_1 beam passes through the first AOM ($-140\times 2MHz$), while the R_2 light undergoes an additional frequency shift ($-120\times 2MHz$) provided by the second AOM. Then, both R_1 and R_2 are recombined with the cooling beam on a polarizing beam splitter and, from then on, they follow the same path. Before going to the vacuum table, the light is split into MOT, ZS and transverse cooling (TC) beams. Both the MOT and the TC beams frequencies are set by a double-pass AOM ($2\times 90MHz$ for the TC light, and $2\times 80MHz$ for the MOT beams), while the ZS light passes through a single pass AOM ($80MHz$). Moreover, once on the vacuum table, a portion of the TC beam is employed for the absorption imaging. As we can see from Fig. 1.3, during the cooling cycle both ^{52}Cr and ^{53}Cr can spontaneously decay from the $^{7}P_4$ state into the metastable states $^{5}D_3$ and $^{5}D_4$. Therefore, in order to reintroduce them in the cooling transition, two red repumper lights addressing the transitions $|^{5}D_3\rangle \rightarrow |^{7}P_3\rangle$ and $|^{5}D_4\rangle \rightarrow |^{7}P_3\rangle$ at $654nm$ and $663nm$ respectively, are exploited [9].
The light sources for these two "red repumpers" are two DL Pro Toptical lasers, both locked by means of a transverse confocal cavity scheme on the Lithium spectroscopy reference at $670nm$, modulated by an EOM (red and orange blocks in Fig. 4.1). In particular, in this scheme the primary mode of the cavity is locked to the Li frequency reference, while the laser is locked to a secondary mode of the cavity, distant from the primary mode of $\frac{\Delta_{FSR}}{2}\sim 1.5GHz$.
The frequencies of both the repumper beams are then adjusted by means of a double pass AOM set at $-2\times 210MHz$ for the $663nm$ laser, and $-2\times 216MHz$ for the $654nm$. Finally, the two red repumpers are combined on a polarizing beam splitter and injected into a common fiber whose output is on the vacuum table.
Also all the blue lights are brought to the vacuum table by means of optical fibers, and they are directed and aligned on the experimental cell, similarly to what already explained for the Li lights in Sec. 3.1 and Fig. 3.3. Both the MOT and the ZS beams are magnified and collimated with a $1\div 2$ telescope, yielding a final beam waist of $\sim 5mm$. The MOT light is realized by three independent retroreflected beams. The Z MOT and the Cr imaging beams setups, as well as the TC one, are placed on two separated vertical breadboards. More details about the whole Cr optical setup are in E. Neri's PhD thesis [15].

4.2 Experimental results

As for the ^{6}Li case, also the bosonic ^{52}Cr MOT was characterized and, after a thorough optimization process, the optimum settings configuration was found. In particular, I report the current values and the beam powers and detunings that allows for the realization of a cold ^{52}Cr MOT composed by $N \sim 7.4 \times 10^6$ atoms.

- MOT current = $55A \rightarrow$ MOT gradient$\sim 30G/cm$
- ZS current = $14A$
- MOT beams power: MOT X=$3.8mW$, MOT Y=$3.8mW$, MOT Z=$2.0mW$
- ZS beam power= $60mW$
- TC beam power= $20mW$
- MOT detunings -4Γ
- ZS beam detuning $\sim -19\Gamma$
- TC beam detuning 1.2Γ
- Loading time $< 3s$

The experimental routine implemented includes an additional $2ms$ CMOT stage at the end of the loading time. As shown in Fig. 4.2, the cooling beam detuning is decreased from -4Γ to -2Γ while its power is lowered down to 10% of its initial value.

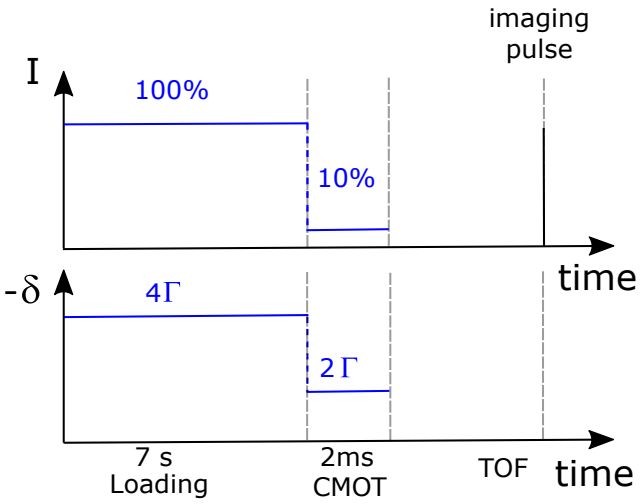

Figure 4.2: *Experimental routine of Cr MOT and CMOT stages. Here are illustrated the reduction of the cooling lights intensity and of its detunings. In figure appears the imaging pulse after a variable time of flight (TOF).*

The measurement of the cloud expansion, obtained with a typical destructive

absorption imaging (Sec. 3.2.1), taken at the end of the CMOT routine, yields a temperature for the Cr atoms of $T \simeq 200(10)\mu K$.
As explained for the Li atoms, during the MOT loading we adiabatically transfer the Cr cloud from the MOT coils quadrupole into the Feshbach coils quadrupole, to ensure a fast switch-off of the fields and to guarantee a free-fall TOF.

4.2.1 Characterization of Cr metastable state $|D_3\rangle$ and $|D_4\rangle$

As we have already explained, during the cooling stage the Cr atoms can decay into the metastable $|D_{3,4}\rangle$ states, which can be trapped with the quadrupole gradient themselves, thanks to their high magnetic moment. In contrast with the Cr MOT, the lifetime of these magnetically trapped states is considerably longer, and thus their presence allows to accumulate in the magnetic quadrupole trap a number of Cr atoms substantially higher than that attainable within the blue MOT. The two additional red repumpers that, as already mentioned, are characterized by a wavelength of $654nm$ and $663nm$, are employed to repump D-state atoms back into the cooling cycle.
The optimum parameters of the red-repumper lights are pinpointed by monitoring the number of the collected Cr atoms as a function of the repumper frequencies (set by the AOM in double pass, as outlined in the previous section), and of their powers and pulse duration. In particular, we load the Cr MOT for $7s$ with only the blue light, let the accumulation of atoms within the D states take place, and then the cold cloud is illuminated with a $30ms$ long repumper pulse and monitored with absorption imaging at $425nm$. By scanning both red repumper frequencies and powers, as well as the illumination time, we could pinpoint the optimum parameters of the red lights. In particular, the atom number is saturated for a beam power of $\sim 15mW$ and $\sim 2mW$, corresponding to $2.4\frac{mW}{mm^2}$ and $0.3\frac{mW}{mm^2}$ for the $|D_3\rangle \rightarrow |P_3\rangle$ and $|D_4\rangle \rightarrow |P_3\rangle$ transition, respectively. Moreover, by considering a loading time of $7s$, the best repumping efficiency is found for a repumper pulse duration ranging from $\sim 15ms$ to $\sim 30ms$.
We can now selectively characterize the number of atoms that are trapped in each D state. The result is summarized in the histogram shown in Fig. 4.3, where the atom number observed in absence of red-repumper lights (blue) is compared with the atom number measured by applying a $30ms$ pulse at $663nm$ (red), $654nm$ (orange), and both $654nm$ and $663nm$ together (purple). This measurement was carried out with a pulse of $30ms$ and a beam power of $\simeq 14mW$ ($\simeq 15mW$) for the $654nm$ ($663nm$) light.
The number of atoms trapped in the $|D_4\rangle$ state greatly exceeds the $|D_3\rangle$ one, in agreement with the relative branching ratio of $\sim 75\%$ and $\sim 25\%$ associated to the decay from the $|P_4\rangle$ state. The total number observed with both the repumper

lights is in good agreement with the sum of the individual contribution from each D state. Moreover, this value depends on the loading time and it saturates at $N_{max} \simeq 7.5 \times 10^7$ within a few seconds, in contrast to the MOT contribution that instead saturates within hundreds of ms, owing to the strong light-assisted collisions [9] and decay to the metastable states.

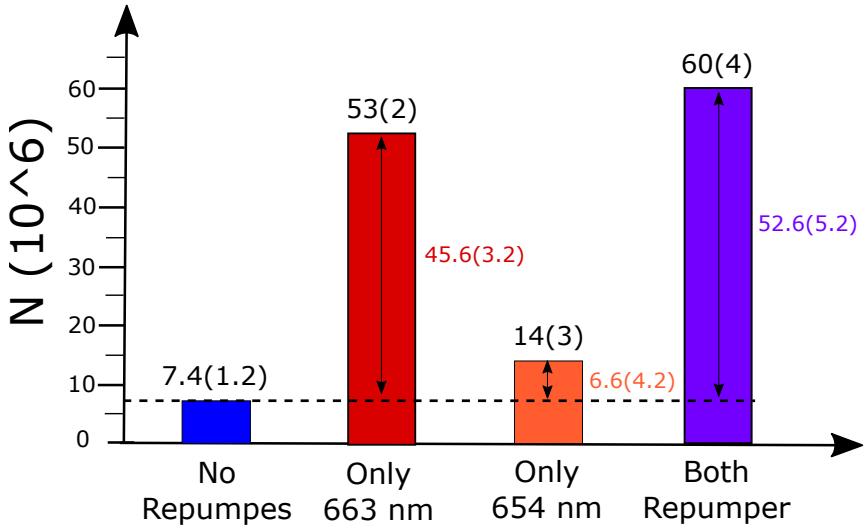

Figure 4.3: *Atom number observed without red-repumpers, with only the* $663nm$ *(*$654nm$*) pulse and with both the repumper lights, after* $7s$ *of loading.*

The rate equations associated to the atom number trapped in the MOT N_M and into the quadrupole N_D, neglecting two-body loss contributions, read

$$\dot{N}_D(t) = \alpha\Gamma_{M\to D}N_M(t) - \Gamma_D N_D(t) \tag{4.1a}$$

$$\dot{N}_M(t) = +L - (\Gamma_{M\to D} + \Gamma_M)N_M(t) \tag{4.1b}$$

where L is the MOT loading rate, $\Gamma_{M\to D}$ is the decay rate of the MOT atoms towards the metastable states, Γ_M is the single particle loss rate of the MOT atoms, Γ_D is the single particle decay rate of atoms occupying the D states, and α is the collection efficiency of the quadrupole trap for the metastable states.
From Eq. 4.1, we obtain

$$N_D^\infty = N_{max} - N_M^\infty = \frac{\alpha\Gamma_{M\to D}N_M^\infty}{\Gamma_D} \tag{4.2}$$

Given that $N_{max} = 7.5 \times 10^7$ and $N_M^\infty = 7.4 \times 10^6$, and considering $\Gamma_D \sim 0.1s^{-1}$ (as we will see below), then $\alpha\Gamma_{M\to D} \simeq 0.9s^{-1}$. Moreover, if we suppose a uniform distribution of the atoms among the 16 Zeeman sublevel of the D_3 and D_4 states, and the ideal case in which all the atoms in the 7 high-field-seeker sub-

levels are captured in the quadrupole gradient, then $\alpha = 7/16$. As a consequence, $\Gamma_{M\to D} \simeq 2s^{-1}$, i.e. of the same order of magnitude of $\Gamma_M \sim 5.7s^{-1}$.

A second important result is the characterization of the metastable state lifetime. The decay rate of the D_3 (D_4) state is measured as it follows. The MOT (plus quadrupole trap) is loaded for $7s$, after which both the ZS magnetic field and the ZS light are switched off. The Cr cloud is continuously illuminated by the cooling beams plus the $663nm$ ($654nm$) light: the atoms are therefore pumped into the D_3 (D_4) state, which is dark for the applied light. Then, after a variable time, the cloud is illuminated with a $30ms$ long pulse of $654nm$ ($663nm$) repumper light, that brings the D-state atoms back into the cooling cycle. Right after the end of the repumping pulse, we acquire an absorption image (at $425nm$) of the cloud.

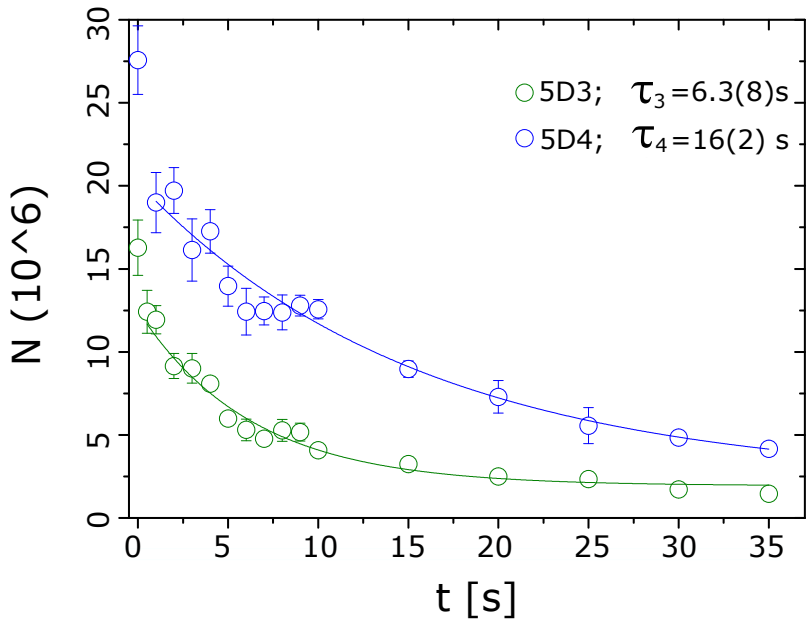

Figure 4.4: *Atom number in the D_3 (green circles) and D_4 (blue circles) states as a function of the decay time. The solid lines are the result of the fit, performed with a single exponential decay: $N_{D_i}(t) = N_{D_i}(0)e^{-t/\tau_i}$, where i=3,4.*

Both trends reported in Figure 4.4 for the two D-states feature the expected fast decay ($t < 0.5s$) contribution due to the MOT atom population. Neglecting the MOT decay, the data follow a single exponential decay characterized by a time constant $\tau_3 = 6.3(8)s$ and $\tau_4 = 16(2)s$ (from which we calculate $\Gamma_D = 1/\tau_i \sim 0.1s^{-1}$). By comparing the initial total atom number of this measurement with those obtained in Fig. 4.3, we can notice a mismatch. We attribute this effect to the

non-negligible light-assisted atomic losses due to the interaction with the red repumpers light, which is switched on during the whole routine.

4.2.2 Simultaneous loading of ^{6}Li and ^{52}Cr MOT

This section reports the outcome of the realization of a preliminary double-species MOT of ^{6}Li and ^{52}Cr atoms. In particular, the lifetime of a coexisting Li-Cr cloud is characterized. This investigation is of great interest in view of the implementation of a simultaneous loading of Li and Cr atoms in ODT.
During this characterization, we focus on the lifetime of the Cr atoms trapped in the D states, which, as we can notice from Fig. 4.3, represent about the 90% of the whole trapped Cr sample. Even though the presence of Li atoms perturbs both the loading efficiency and the lifetime of the Cr sample, this measurement proves the possibility to produce a double-species MOT.
Fig. 4.5 shows an example of simultaneous loading of a Li-Cr double-species MOT.

Figure 4.5: *Picture of the Li (red cloud)-Cr (blue cloud) cold sample, not perfectly overlapped.*

Fig. 4.6 shows the lifetime of the Cr atoms in the D states in absence of the Li cloud (already analysed in Fig. 4.4 and here reported in green and blue circles for the atoms in D_3 and D_4 respectively), compared with the trend of the atom number associated to the same state in presence of a Li MOT of about $N_{Li} \sim 10^8$ atoms (blue and green dots for the D_4 and D_3 state).
For the acquisition of these data we simultaneously loaded the Li and the Cr MOT for $7s$. Then the Li and Cr ZS currents and beams were switched off and the Cr shutter oven was closed. Selective accumulation of Cr atoms in D_3 (D_4) was obtained by continuously addressing during the loading time the $D_4 \rightarrow P_3$ ($D_3 \rightarrow P_3$) transition. Finally, we illuminated the cloud with a $30ms$ long $654nm$ ($663nm$) repumping pulse before performing the imaging with the $425nm$ light.

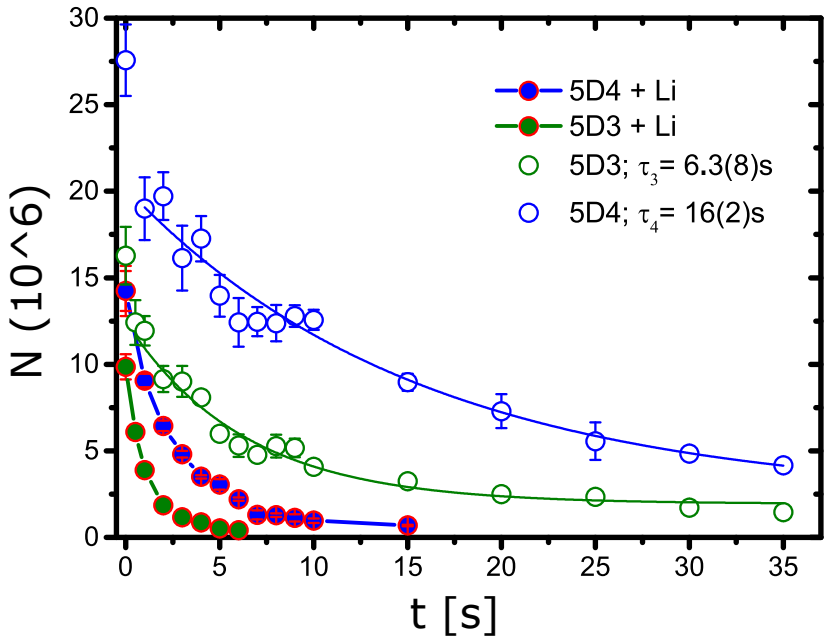

Figure 4.6: *Trend of the atom number as a function of the decay time. In green are represented the data for the atoms trapped in the D_3 state, while in blue are reported the data relative to the atoms in the D_4 state. Circles and dots refer respectively for the Cr cloud in absence and presence of Li atoms.*

From Fig. 4.6 we can notice two important features. First, by comparing the atom number at $t = 0$ one can see how the atoms trapped within the D state is reduced of a factor ~ 2 by the presence of the Li MOT. Second, the presence of Li atoms diminishes the lifetime of the metastable states.
Since we have checked that the presence of Cr atoms does not affect the Li MOT atom number, nor its size, and given that the trend of the Li atom number after the loading is well fitted by a single exponential decay with $\tau_{Li} = 17.5s$ [15], we can easily solve the rate equation for the D-state population:

$$\dot{N}_{D_i}(t) = -\beta_{D_i} N_{Li}(t) N_{D_i}(t) - \frac{1}{\tau_i} \alpha N_{D_i}(t) \tag{4.3}$$

Indeed, assuming that these populations are mainly limited by inelastic two-body Cr-Li processes characterized by a rate constant β_{D_i} (i.e. $\tau_i \gg (\beta N_{Li})^{-1}$), one can neglect the second term in Eq. 4.3 and obtain an expected trend of $N_{D_i}(t)$ that reads as

$$N_{D_i}(t) = N_{D_i}(0) e^{(N_{Li}(0)\beta_{D_i}\tau_{Li}(e^{-t/\tau_{Li}}-1))} \tag{4.4}$$

Fig. 4.7 shows the results obtained by fitting the quadrupole decay curves with Eq. 4.4. The fit was only applied to the data-points at $t > 1s$ since, as already discussed, the evolution of the Cr atom number at $t < 0.5s$ accounts for both the

contributions from those atoms confined in the MOT and within the quadrupole field. The value of β_{D_i} is extracted from the fit and rescaled to the constant volume featured by the Li MOT cloud ($\beta[1/s] \rightarrow \tilde{\beta}[cm^3/s]$) yielding $\tilde{\beta}_{D_3} = 1.6(4) \times 10^{-10} cm^3 s^{-1}$ and $\tilde{\beta}_{D_4} = 8(2) \times 10^{-11} cm^3 s^{-1}$ for the $|D_3\rangle$ and D_4 state, respectively.

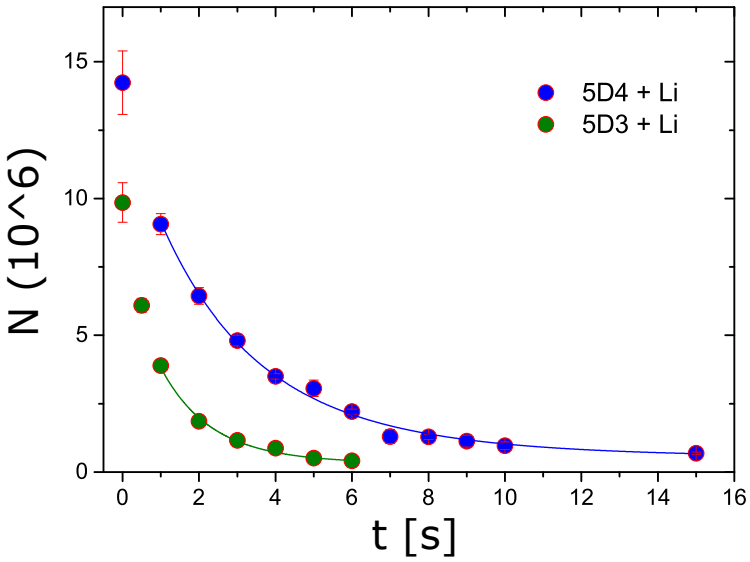

Figure 4.7: *Atom number in the D_3 (green dots) and D_4 (blue dots) state as a function of the decay time. The solid lines represent the fit performed with Eq. 4.4.*

Even though Eq. 4.4 matches well the experimental data, we cannot determine the specific mechanisms which cause the Cr losses from the quadrupole, because of the low resolution of the N_{Li} measurements. Indeed, the experimental uncertainty of the Li MOT atom number is 10%, that is comparable with the Cr atom number trapped in the quadrupole.
The experimental results reported above demonstrate the possibility to simultaneously produce cold Cr and Li samples within our experimental apparatus. Indeed, in spite of a less efficient accumulation of D state Cr atoms in the magnetic quadrupole of the MOT, the presence of $\sim 10^8$ Li atom MOT does not prevent the loading of Cr sample comprising up to $\sim 2.5 \times 10^7$ atoms at about $200\mu K$ within a few seconds of experimental cycle. This appears as an extremely promising starting point for the loading of the mixture in the ODT, and for the successive evaporative and sympathetic cooling steps.

Finally, Fig. 4.8 shows the very first signal of a MOT of fermionic ^{53}Cr atoms observed during the very last days of my thesis work. The picture is taken with a fluorescence imaging with an integration time of $5s$. The atom number is $N \sim 10^4$, consistently with a significantly smaller ZS flux expected for the fermion, when

compared with the boson [9]. Moreover, since the detuning is very small ~ 1Γ, also the volume of the MOT is very small.

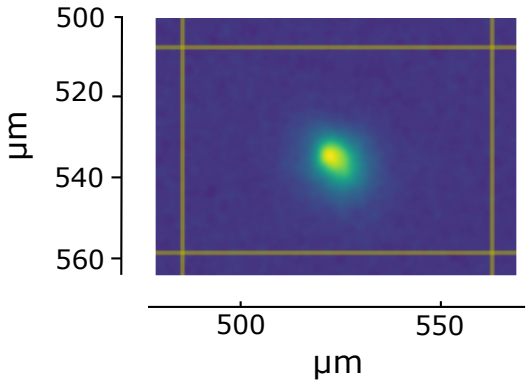

Figure 4.8: *Fluorescence imaging of our first ^{53}Cr MOT.*

In the lab we are currently focusing our work on the characterization and optimization of the fermionic ^{53}Cr MOT.

Chapter 5

Compensation of thermal lensing effects in the optical trapping setup

In this Chapter I present a study that was carried out in the lab during my thesis period in order to implement a high-power ODT setup free from thermal lensing (TL) effects. TL effects, as it will be explained in the following, modify the position of a focused beam by an amount which depends upon the laser power and wavelength. As such, they are detrimental if one wants to perform all-optical evaporative cooling, since the trap location will vary during the evaporation ramp. In particular, TL should be minimized in the specific case of a bichromatic ODT that combines, as in our setup, two high power laser sources at different wavelengths. At the beginning of my thesis, the characterization of TL introduced by the employed optical components was already started, as well as the realization of the optical setup utilized for the TL compensation. During my thesis work I participated in the data acquisition and analysis of the thermal effects and I contributed to test the efficacy of our configuration by monitoring the ODT focused on a cold Lithium sample. The outcome of this investigation is available as a publication in Optic Express [7].
The chapter is organized as it follows: Section 5.1 provides a theoretical introduction to the thermal lensing effect, and discusses the possibility of its cancellation. Sec. 5.2 presents a characterization of the thermal lensing effect introduced by each optical element employed in our experimental setup for the IR laser ODT. Finally, Section 5.3 outlines the optical scheme utilized in order to eliminate the TL, and describes how it operates on an atomic trapped cloud.

5.1 Theory of thermal lensing

The thermal lensing phenomenon originates from the modification of the light path caused by the propagation of high-power radiation through a partially absorbing material. When a Gaussian beam impinges on an optical element, this latter absorbs part of the light and, consequently, it heats up. In particular, due to the non-uniform beam intensity profile, the heating of the material is inhomogeneous. According to the dependence of the refractive index on the temperature [39,40], this heating leads to a local alteration of the optical path experienced by the beam. As a consequence, the optical element acts as a lens for the beam, and both the size and the position of the beam waist acquire a dependence on the illumination time[1] and on the beam intensity.
Fig. 5.1 schematically shows this effect.

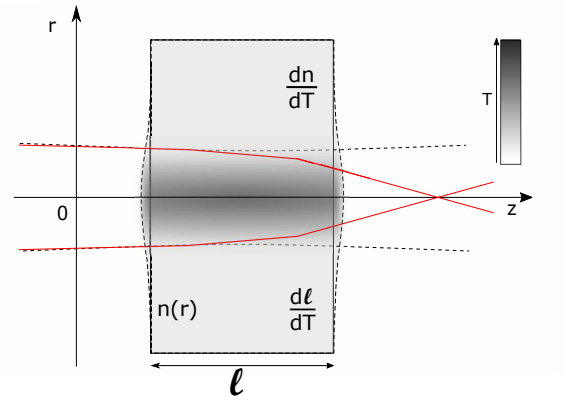

Figure 5.1: *Schematic view of thermal lensing caused by a Gaussian beam impinging an optical material with thickness ℓ. The Gaussian profile induce a temperature gradient that changes both the refractive index (dn/dT) and the local material dimension ($d\ell/dT$). These two effects modify the wave propagation.*

Despite TL is negligible at low intensities, it may become relevant in those experiments that require the implementation of a $\sim mK$ deep potential with large trapping volumes, such that high-power lasers (up to a few hundreds of Watts) focused down to few tens of micron are needed. Additionally, even though thermal lensing may not be a major problem as long as monochromatic ODTs and samples composed by a single atomic species are considered, TL can strongly reduce the efficiency of bichromatic traps, and of sympathetic cooling between two different atomic species. For these reasons, it is extremely important in our setup to minimize TL effects.

[1] The analysis of the dynamic TL effect go beyond this work, because of a restriction due to the minimum time resolution of our sensor.

Generally, a theoretical description of TL is difficult, owing to the different mechanisms from which it can originate (thermal expansion of the material, strain, temperature dependence of the refractive index). However, for common optical materials, we can associate thermal lensing to the sole temperature dependence of n, and we can quantify its effects by defining the thermal focal length [41] as:

$$f_{th} = \frac{2\pi\kappa}{1.3b(dn/dT)\ell}\frac{w^2}{P} = \frac{1}{m_0}\frac{w^2}{P} \tag{5.1}$$

where P is the laser power, w the beam waist, κ the material thermal conductivity and b is its absorption coefficient. From Eq. 5.1 we can see that the thermal focal length is inversely proportional to the laser intensity with a proportionality constant m_0 that depends only on the material properties.
In order to figure out how to eliminate the thermal lensing effect it is useful to recall how a lens modifies the beam propagation. When a Gaussian beam impinges on a thin lens of focal length f_{th} positioned at a distance s from the beam waist w_0 (see Fig 5.2), the lens creates a new real (virtual) waist w_0' at a distance $s' > 0$ ($s' < 0$).

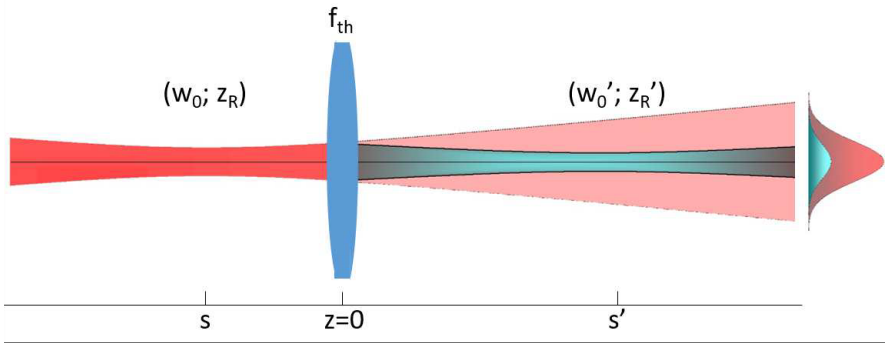

Figure 5.2: *Sketch of a Gaussian beam impinging on a thin lens.*

According to the propagation of a Gaussian beam through a thin lens [42], it is clear that, if $f_{th} \to \pm\infty$, then $s' = -s$ and $w_0' = w_0$, hence the beam propagation is not modified. If instead f_{th} has a finite value, a new beam waist w_0' is created at a distance s'. In this latter case, also the radius of curvature of the beam changes:

$$R(z) = (z+s)\left(1+\left(\frac{z_R}{z+s}\right)^2\right) \to R'(z) = (z-s')\left(1+\left(\frac{z_R'}{z-s'}\right)^2\right) \tag{5.2}$$

By monitoring the consequent variation of the beam intensity behind the thermal lens as a function of the incident power it is therefore possible to quantify the thermal lens associated with any optical component.
An important observation is that, when the beam waist position coincides exactly with the thermal lens plane ($s = 0$), the subsequent light propagation is described

by:

$$s' = \frac{z_R^2/f_{th}}{1 + z_R^2/f_{th}^2} \qquad \frac{w_0'}{w_0} = \frac{1}{\sqrt{1 + \left(z_R/f_{th}\right)^2}} \tag{5.3}$$

where $z_R = \pi w_0^2/\lambda$.
Namely, for $|f_{th}| \gg z_R$ (condition usually met in a typical cold atom trapping setup), the variation of the beam propagation is detectable only very close to the lens, the outgoing beam being almost unaffected by the lens. This simple observation suggests that, in order to remove[2] TL effects at all distances, it is sufficient to place the optical element responsible for the thermal lens within a focus of the incoming beam.

5.2 Source of thermal lensing in optical setup

In order to realize an optical setup free from thermal lensing it is essential to first pinpoint the elements that mostly contribute to this effect by estimating their f_{th}. Indeed, each optical component introduces some degree of TL (it is therefore convenient to minimize the number of elements in a high-power optical setup), and it is crucial to identify those whose contribution onto the final focus position of the ODT is non-negligible with respect to the axial trap dimension (few millimeters considering our ODT).
As we have already mentioned in the previous section, a measure of TL effects can be made by monitoring the beam axial intensity profile behind a thermal lens versus the incident power. Fig 5.3 presents a sketch of the typical setup employed for this measurement: after crossing various optical elements which could introduce TL (in the sketch are shown all components of the final setup, i.e. f_1, f_2 and the AOM), the beam is split into a high-power part, sent to a beam dump, and a low-power part, that is focused (via f_3) onto a CCD camera. By moving the CCD camera through a micrometric translational stage and recording the intensity profile, it is possible to pinpoint the focus position for every incoming power value. In this way we can estimate the focus shift (Δz_{th}) with respect to the focus position at low power and quantify, therefore, the thermal lensing effect.
Our laser source is a multimode fiber laser with central emission wavelength of $1070nm$ and output waist of about $2.2(2)mm$. The AOM, realized by a TeO_2 crystal, has an optimum diffraction efficiency around 85% for an incoming beam waist of 550 μm, hence two lenses ($f_1 = 200mm$ and $f_2 = 50mm$) are employed to demagnify the output beam. In order to avoid the CCD camera saturation

[2] Aside for correction of the order of $O\left(\frac{z_R^2}{|f_{th}|}\right)$

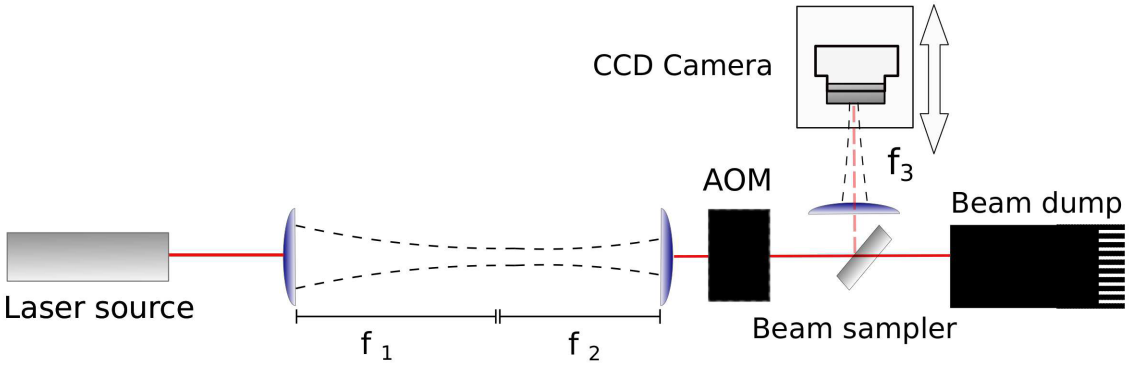

Figure 5.3: *Setup for thermal lensing measurements.*

without introducing systematic TL effects we employed first a beam sampler[3] that reflects a small portion ($P < 10W$) of the radiation exiting the AOM. Then, a second attenuation without significant thermal effects is obtainable with a high-reflection mirror. Finally, the beam is focused on the camera (with $w \simeq 45\mu m$) by a third lens $f_3 = 250mm$, which does not produce further thermal effects, since the small incoming power.

Fig. 5.4 shows the trend of Δz_{th} as a function of the laser power for various elements. It is easy to notice that both the single lens f_1 and the $f_1 - f_2$ telescope configuration lead to a very small shift[4] of the focus position up to power of $280W$. In both cases $\Delta z_{th} \leq 100\mu m$, that is negligible compared with the ODT axial size. Moreover, the additional presence of a quartz window, identical to the viewport of the science chamber, on the optical path causes only a minimal change (in Fig. 5.4 black squares and red circles). The thermal shift measured with the AOM after the telescope is instead two orders of magnitude larger than the ones observed with the lenses (and window) alone. In conclusion, from this characterization it is clear that the AOM crystal is the only relevant source of thermal lensing within our ODT setup.

The predicted shifts Δz_{th} (dashed and solid lines in Fig. 5.4), obtained by a Gaussian beam propagation analysis simulation and by relying on the m_0 values of the different materials available in literature, match the experimental data apart from the single lens measure (yellow circles). This discrepancy is likely due to the TL effect of the filtering stage, only sizable for the single lens measurement. In fact, in this case the beam impinging on the beam sampler is focused, rather than collimated, and for this reason the thermal lens associated with the filtering

[3] Within the considered range of powers, TL effects introduced by reflective components are negligible.

[4] The results of the two dataset are not directly comparable due to the different measurement setup.

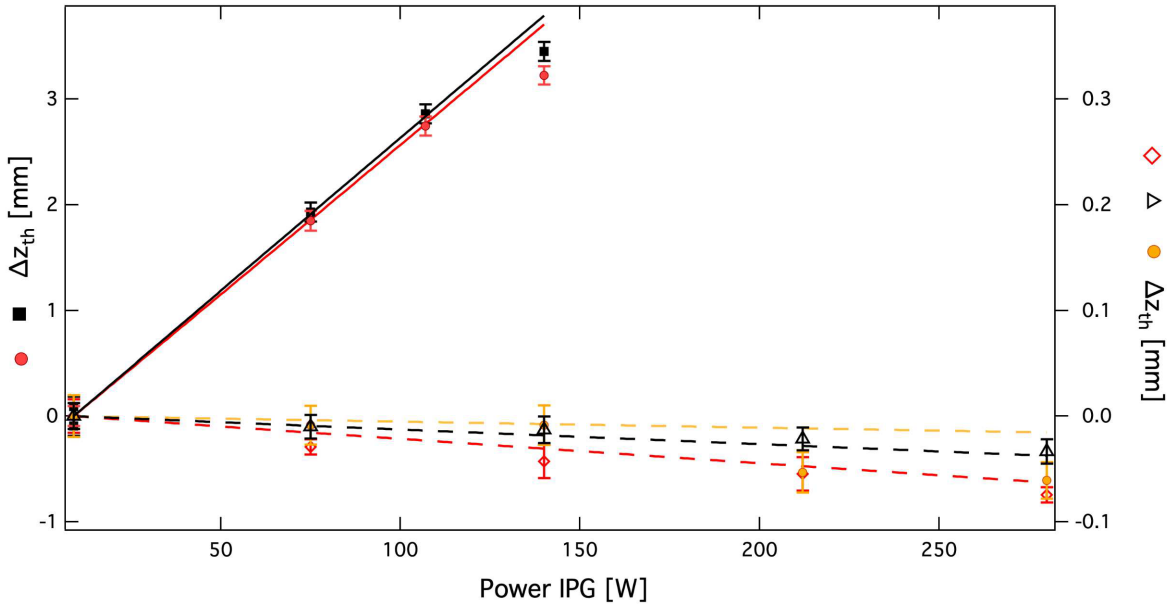

Figure 5.4: *Thermal shift Δz_{th} as a function of the laser power recorded for different combinations of optical elements. Right axis: Δz_{th} due to the $f_1 - f_2$ telescope with $f_2 = 50mm$ in Suprasil®3001 (black triangles) or UV fused silica (red diamonds). The shift of the $f_1 = 200mm$ fused silica lens alone (yellow circles) has been tested directly by measuring its focus shift versus the beam power. For each data set, the dashed line is the corresponding shift calculated by Gaussian beam propagation analysis, assuming each element to represent an additional lens with f_{th} given by Eq. 5.1 and characterized by the corresponding m_0 value found in literature (more details in [7]). Left axis: thermal shift of the optical setup with inclusion of the AOM crystal, with (black squares) or without (red circles) quartz window in the beam path. The AOM was placed at $d_{AOM,2} = 3(1)cm$ behind the second lens f_2, the last lens f_3 at $d_{3,AOM} = 58(2)cm$ from the AOM, whereas the window (if present) was at $d_{win,3} = 12(1)cm$ after f_3. Solid lines (same color code) show the focus shift calculated by Gaussian beam propagation analysis, assuming the AOM thermal lens to be described by Eq. 5.1 with the m_0 value found in literature and listed in [7].*

stage is substantially increased, relative to all other measurements.

5.3 Compensation of the thermal lensing effect

From the characterization described in the previous section we have identified the AOM crystal as the major and only relevant source of TL within our setup. Moreover, as anticipated in Sec. 5.1 and in particular in Eq. 5.3, the impact of one thermal lens on a propagating beam can be minimized by positioning the thermal element within a focus along the optical path. We have therefore char-

acterized how the focus produced by f_3 on a CCD camera shifts as a function of the position δz_{AOM} of the AOM crystal relative to the focus of the $f_1 - f_2$ telescope, for two different values of the incident power (see details in caption of Fig. 5.6). Fig. 5.5 shows the setup employed for this measurement.

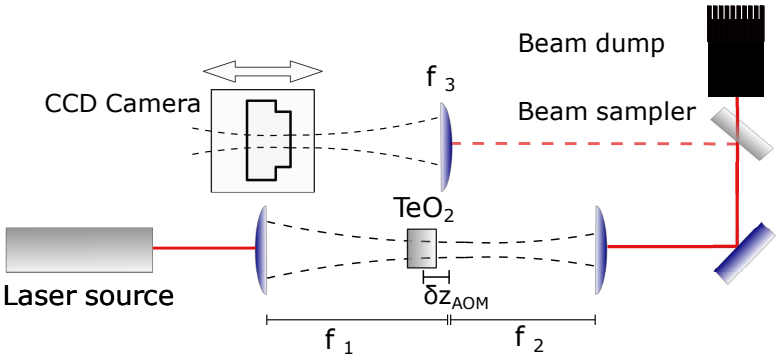

Figure 5.5: *Schematic view of the optical scheme employed for the characterization of the AOM thermal lens, as a function of the crystal position. A TeO_2 crystal is placed at a variable distance δz_{AOM} from the focus within the $f_1 - f_2$ telescope as shown in the picture. For this measure, $f_1 = 300mm$ and $f_2 = 75mm$. The f_3 lens is placed at $d_{3,2} = 47(2)cm$ from the second lens f_2, and the focus location is monitored for different levels of incident laser power through a CCD camera.*

Given that f_1 focuses the incident beam down to waist of $\sim 45\mu m$, in this configuration the power level was kept below $60W$. However, this corresponds to an intensity on the AOM crystal about 40 times higher than the one reached within standard operating conditions, yielding $f_{th} \sim 30cm$.
Fig. 5.6 shows the acquired data (red diamonds) and the simulated curves (black lines) obtained from the analysis of Gaussian beam propagation. From Fig. 5.6 it is easy to see that a small variation in the AOM position is sufficient to produce big changes in the beam propagation, but also that there are two AOM locations at which the thermal lensing effect is zeroed (i.e. $\Delta z_{th} = 0$). The first position is the expected $\delta z_{AOM} = 0$, when the AOM is within the focus of the telescope, while the second is $\delta z_{AOM} \simeq 30mm$. From the Gaussian beam propagation analysis, this latter case corresponds to a configuration in which the radius of curvature of the perturbed beam coincides with that of the unperturbed one only on the plane of f_3. While also this second configuration enables to strongly suppress thermal lensing, it is however less robust than the $\delta z_{AOM} = 0$ one. Given that in this case the radii of curvature associated with different power levels coincides only at the f_3 plane, rather than throughout the whole optical path, the beam magnification due to f_{th} at the f_3 plane may significantly differ from unity. As a consequence, although the position of the focus produced by f_3 will only weakly depend upon the specific value of f_{th} (i.e. of incident power), the beam waist may sizable vary,

relative to the $|f_{th}| = \infty$ case.
Although this measurement has represented an excellent proof-of-principle check that indeed TL can be suitably canceled by placing the AOM within a focus of the beam, in the actual configuration of Fig. 5.5, the f_1 focuses the beam on the AOM with a waist of about $45\mu m$. This small beam waist value drastically reduces the diffraction efficiency of the TeO_2 crystal, and yields at the highest power level of our laser source an intensity exceeding the AOM damage threshold.

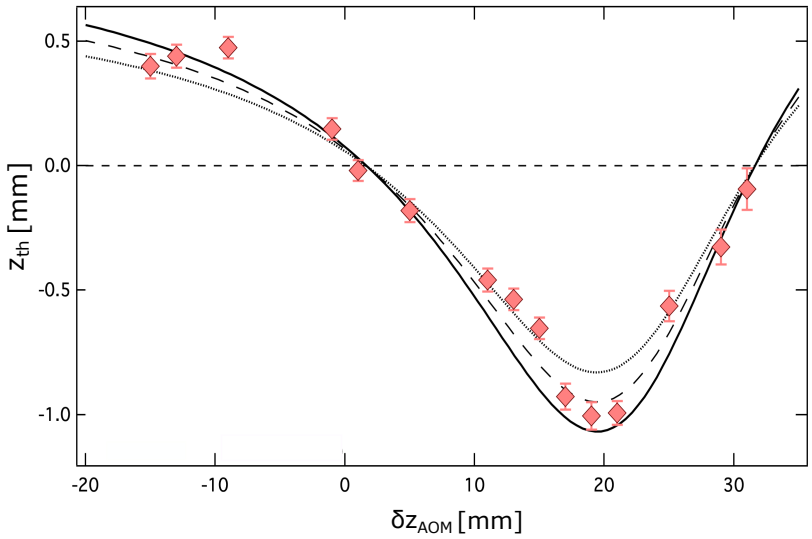

Figure 5.6: *Thermal-induced shift Δz_{th} of the f_3 focus position experimentally determined (red diamonds), as a function of the AOM distance from the f_1 focus. Δz_{th} is obtained by comparing high and low power data acquired at $P = 50(1)W$ and $P = 9.0(5)W$, respectively. The shift predicted by the Gaussian beam propagation analysis is shown as black lines for $P = 55W$ (solid), $P = 50W$ (dashed) and $P = 45W$ (dotted).*

In order to overcome this issue, among different solutions, we opted for a scheme based on the same elements depicted in Fig. 5.5, with the first two lenses no longer in a telescope configuration but rather acting as an equivalent lens with effective focal length $f_{1,2}^{eq}$, that generally depend upon the parameter $\delta z = L_2 - L_1 - (f_1 + f_2)$. Here L_i and f_i denote the position and the focal length of the i-th lens, respectively. The first lens was mounted on the translation stage with resolution of $10^{-2} mm$, and the position of the focus produced by $f_{1,2}^{eq}$ was determined by Gaussian beam matrices as a function of the L_1 position, hence of δz. From our theoretical analysis we found that there exist various L_1 configurations, all for small and positive δz values, yielding a focus at relatively short distances from the second lens f_2, with the beam waist ranging between 550 and $500\mu m$. Therefore, as in the previous case, the thermal effect associated to the AOM is quantified

by monitoring the shift of the f_3 focus for two values of incident power. In this measurement the AOM is kept in a fixed position and the shift is observed as a function of δz, by varying L_1 by means of a translational stage.
Fig. 5.7 presents the results for this latter characterization for two positions of the AOM crystal, namely for two different distances $d_{AOM,2}$ from the second lens f_2: $d_{AOM,2} = 23(2)mm$ and $d_{AOM,2} = 3(1)mm$ for panel a) and b), respectively.

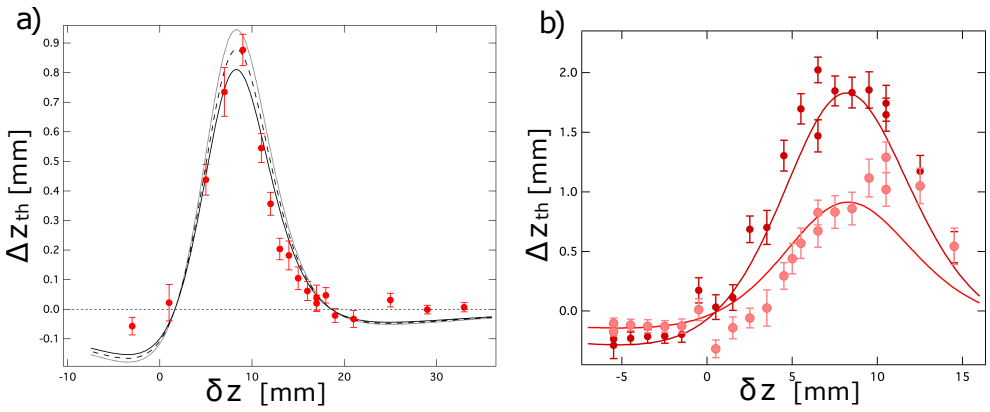

Figure 5.7: *The two panels show the measured thermal shift Δz_{th} (red circles) of the focus created by the last lens f_3 as a function of the parameter δz for the two different AOM locations, i.e. for two different distances $d_{AOM,2}$ from the second lens f_2. a) The AOM was positioned at $d_{AOM,2} = 23(2)cm$ relative to the plane of the second lens. Δz_{th} was obtained by comparing the focus position measured at $P = 75(1)W$ and $P = 9.0(5)W$, respectively. Black lines show the simulated Δz_{th} for different high power levels: $80W$ (dotted lines), $75W$ (dashed lines) and $70W$ (solid lines). b) Experimentally measured thermal shift as in panel a), but with the AOM positioned at $d_{AOM,2} = 3(1)cm$. Two high power values have been checked, relative to the low power reference at $P = 9.0(5)W$: $80(1)W$ (light red circles) and $150(2)W$ (dark red circles). Solid lines show the simulated trend expected for the two power levels. For both data sets, $f_1 = 300mm$ and $f_2 = 75mm$, and the las lens f_3 was kept fixed at $d_{3,2} = 155(2)cm$.*

The uncertainties in both panels of Fig. 5.7 are the combination of the standard error of the axial intensity profile fitted with $I(z,z_0) = I_0(\frac{w_0}{w(z)})^2 = \frac{I_0}{1+(\frac{z-z_0}{z_R})^2}$ for the high and low power data sets.
Aside for slight quantitative changes, the observed trends of Δz_{th} qualitatively agree with the one obtained when moving the TeO_2 crystal within the focus of the $f_1 - f_2$ telescope (see Fig. 5.6), and, despite the accessible δz range is experimentally limited[5], also in this configuration it is possible to find two L_1 positions that cancel the TL effect.

[5]On one side from the AOM diffraction efficiency and on the other from the AOM crystal size.

5.3.1 Thermal lensing on atoms

We finally tested the efficacy of our scheme by directly monitoring the axial position of a cold atomic cloud confined within the high power beam, employing a configuration of the optical setup analogous to the one considered in Fig. 5.7, with $d_{AOM,2} = 3(1)cm$. The setup employed for this last measurement is sketched in Fig. 5.8.
We produced a Li cold cloud of $\sim 2.0(2) \times 10^8$ atoms at $T \simeq 80\mu K$, which we subsequently illuminated (for $400ms$) with the ODT beam. The position of the cloud along the ODT was obtained by a Gaussian fit of the atomic density profiles acquired by means of *in situ* absorption imaging (see Fig. 5.8). The axial barycenter of the atomic cloud, corresponding to the energy minimum of the optical potential, reflects the waist position of the ODT beam for any value of incident power and of δz.

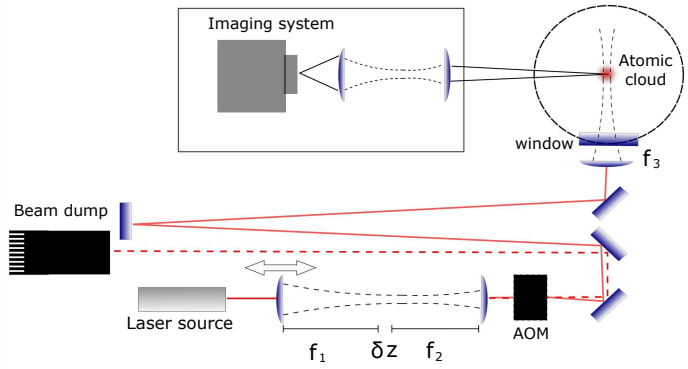

Figure 5.8: *Sketch of the setup employed to investigate thermal lensing by monitoring an atomic cloud trapped in the ODT. Typical atom number in the ODT after* $400ms$ *illumination time ranges from* 1×10^5 *(*$P = 40W$*) to* 7×10^5 *(*$P = 220W$*). For this measurements,* $f_1 = 200mm$ *and* $f_2 = 50mm$ *while the last lens* f_3 *is placed at* $d_{3,AOM} = 200(5)cm$.

Fig. 5.9 shows examples of the experimentally determined shifts of the cloud position along the beam axis, relative to the one obtained at the lowest possible power enabling to capture a detectable atomic fraction ($P = 40(1)W$), as a function of the power level for different δz values. Also these data show that one can adjust the δz parameter to induce either positive or negative thermal shifts of variable magnitude and, most importantly, to cancel them out.
Fig. 5.10 shows Δz_{th} as a function of δz, comparing the cloud position recorded for high- ($P = 220(2)W$) and low- ($P = 40(1)W$) power conditions.
Despite the qualitative agreement with the trend presented in Fig. 5.7, the data do not match well the simulated curves in Fig. 5.10. In particular, our theoretical model systematically underestimates the measured shifts (black squares) around the region of maximum Δz_{th}, even when allowing for a ±35% uncertainty in the

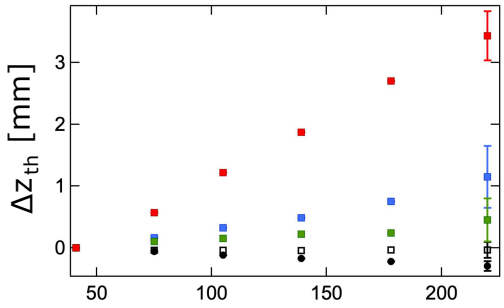

Figure 5.9: *Thermal shift Δz_{th} of the focus position as a function of the beam power P for different values of the parameter δz: $\delta z = 1.7(1)mm$ (red squares), $\delta z = 1.2(1)mm$ (blue squares), $\delta z = 0.45(1)mm$ (green squares), $\delta z = 0.0(1)mm$ (white squares) and $\delta z = -2.3(1)mm$ (black circles).*

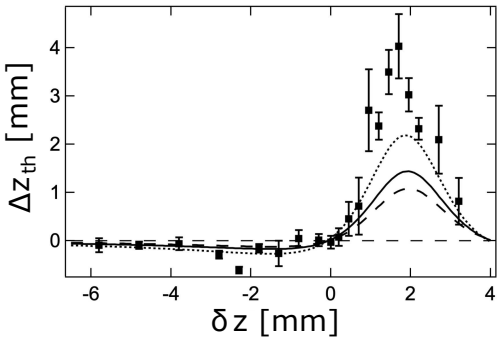

Figure 5.10: *Thermal shift Δz_{th} as a function of the parameter δz at a fixed power $P = 220(2)W$. The solid line shows the thermal shift expected from the Gaussian beam matrices calculation considering the f_{th} of the AOM crystal given by Eq. 5.1 with the m_0 value listed in [7]. The dashed (dotted) line shows the expected thermal shift for $f_{th} + \Delta f_{th}$ ($f_{th} - \Delta f_{th}$) where Δf_{th} is our estimate of f_{th}'s uncertainty of around 35%. Error bars combine the statistical uncertainties of the high and low power reference data sets on the atomic cloud barycenter, obtained for each point from an average of 4 independent measurements.*

determination of the AOM thermal lens (dashed and dotted curves). We ascribe this mismatch to some degree of astigmatism that affected the trapping beam for this specific δz range, likely caused by a non-perfect centering of the beam on the AOM crystal. Most importantly, both Fig. 5.9 and 5.10 validate the possibility to cancel thermal lensing effects from a high power optical trapping setup by properly adjusting the AOM position with respect to the beam waist.

Conclusions

In this thesis I have reported my contributions to a new experimental platform for the realization of an ultracold mixture of Lithium and Chromium atoms.
In particular, I have described the design of the compensation coils setup and I have tested its effects on a cold Lithium sample, proving that these coils can be employed in order to controllably shift the cold atomic clouds with respect to the initial position of the quadrupole. Moreover through a simulation I have shown how the compensation coils switched in anti-Helmholtz configuration produce a magnetic gradient that, combined with that one of the MOT coils, may allow to balance the gravitational sag experienced by Cr and Li atoms in ODT.
In this work I have also presented the characterization of the gray molasses cooling stage operating on the D_1 atomic transition, which enables the achievement of sub-Doppler temperatures within the Li atomic sample. Additionally, I have optimized the gray molasses stage minimizing residual magnetic fields by means of the compensation coils. This has enable to routinely produce Li clouds of $N \sim 10^8$ atoms at $T \simeq 40\mu K$.
Regarding the Chromium atomic species, in this thesis I have presented the analysis of the loading and the decay rates associated to the metastable D_3 and D_4 states. This characterization has been carried out both for the single species Cr MOT and for the Cr atoms in presence of Li MOT. The main and very important outcome of this experimental survey is the demonstration of the possibility to simultaneously load, within a few seconds, up to $\sim 3 \times 10^7$ ^{52}Cr atoms together with large MOT clouds of about 2×10^8 Li atoms.
Within the very last days of my thesis, the first signal of a MOT of ^{53}Cr atoms has been observed, and it is currently characterized and optimized in the lab.
Finally, in this work I have described the thermal lensing effects and I have discussed a thorough characterization of this effect within a standard ODT setup. This study has led to the design and the implementation of a totally passive and inexpensive scheme allowing to realize high-power bichromatic optical dipole traps free from thermal lensing effects.

The work discussed in this thesis paves the way to interesting prospectives: once the fermionic ^{53}Cr MOT will be optimized, we will characterize the collisional

stability of the Fermi-Fermi ^{53}Cr-^{6}Li mixtures in the cold regime by following the same approach adopted already (and described in this thesis) for the Bose-Fermi ^{52}Cr-^{6}Li mixtures. This will allow to devise the best strategy to efficiently load the laser cooled Cr-Li mixture within our bichromatic ODT. Parallel to this, we will start a thorough Feshbach spectroscopy study that will allow to identify both inter- (Cr-Li) and intra- (Cr-Cr) species resonances, totally unknown so far. From this investigation we will be able to pinpoint the most favorable inter-species resonances, that will be firstly employed to ensure an efficient thermalization during the evaporative and sympathetic cooling stages.
On a longer timescale, the availability of heteronuclear Feshbach resonances will facilitate the attainment of double-degeneracy for the Cr-Li mixture, and it will pave the way to the experimental investigation of few- and many-body regimes with such a novel system.

Bibliography

[1] Stefano Giorgini, Lev P. Pitaevskii, and Sandro Stringari. Theory of ultracold atomic fermi gases. *Reviews of Modern Physics*, 80(4):1215–1274, oct 2008.

[2] Immanuel Bloch, Jean Dalibard, and Wilhelm Zwerger. Many-body physics with ultracold gases. *Reviews of Modern Physics*, 80(3):885–964, jul 2008.

[3] O I Kartavtsev and A V Malykh. Low-energy three-body dynamics in binary quantum gases. *Journal of Physics B: Atomic, Molecular and Optical Physics*, 40(7):1429–1441, mar 2007.

[4] B. Bazak and D. S. Petrov. Five-body efimov effect and universal pentamer in fermionic mixtures. *Physical Review Letters*, 118(8), feb 2017.

[5] D. S. Petrov. Three-body problem in fermi gases with short-range interparticle interaction. *Physical Review A*, 67(1), jan 2003.

[6] Edmund C. Stoner. LXXX.atomic moments in ferromagnetic metals and alloys with non-ferromagnetic elements. *The London, Edinburgh, and Dublin Philosophical Magazine and Journal of Science*, 15(101):1018–1034, may 1933.

[7] C. Simonelli, E. Neri, A. Ciamei, I. Goti, M. Inguscio, A. Trenkwalder, and M. Zaccanti. Realization of a high power optical trapping setup free from thermal lensing effects. *Optics Express*, 27(19):27215, sep 2019.

[8] M. E. Gehm. *Properties of 6Li*. PhD thesis, 2003.

[9] R. Chicireanu. *Studies of cold Chromium atoms in magnetic and optical trap: steps towards Bose-Einstein Condensation*. PhD thesis, Université Paris-Nord XIII, 2007.

[10] Peter van der Straten Harold Metcalf. *Laser Cooling and Trapping*. Springer-Verlag GmbH, 1999.

[11] Massimo Inguscio and Leonardo Fallani. *Atomic Physics: Precise Measurements and Ultracold Matter*. OUP Oxford, 2013.

[12] William D. Phillips. Nobel lecture: Laser cooling and trapping of neutral atoms. *Reviews of Modern Physics*, 70(3):721–741, jul 1998.

[13] Paul D. Lett, Richard N. Watts, Christoph I. Westbrook, William D. Phillips, Phillip L. Gould, and Harold J. Metcalf. Observation of atoms laser cooled below the doppler limit. *Physical Review Letters*, 61(2):169–172, jul 1988.

[14] Milena Guevara-Bertsch, Lena Salfenmoser, Andrés Chavarría-Sibaja, Esteban Avendaño, and Óscar Andrey Herrera-Sancho. Design and characterization of a zeeman slower. 2016.

[15] Elettra Neri. *Mass imbalanced Fermi mixtures with 2- and 3- resonant interactions*. PhD thesis, University of Florence, 2019.

[16] Giacomo Valtolina. Development of an experimental apparatus for the production and study of ultracold atomic gases of fermionic lithium. Master's thesis, University of Milan, 2012.

[17] Christian Dornes. 3d-focusing spectrometer for a reaction microscope. Master's thesis, University of Heidelberg, 2011.

[18] Steven Chu. Nobel lecture: The manipulation of neutral particles. *Reviews of Modern Physics*, 70(3):685–706, jul 1998.

[19] Claude N. Cohen-Tannoudji. Nobel lecture: Manipulating atoms with photons. *Reviews of Modern Physics*, 70(3):707–719, jul 1998.

[20] L. Gabardos, S. Lepoutre, O. Gorceix, L. Vernac, and B. Laburthe-Tolra. Cooling all external degrees of freedom of optically trapped chromium atoms using gray molasses. *Physical Review A*, 99(2), feb 2019.

[21] D. R. Fernandes. *Trapping and cooling of fermionic alkali atoms to quantum degeneracy. Sub-Doppler cooling of Potassium-40 and Lithium-6 in gray molasses*. PhD thesis, UNIVERSITÉ PARIS VI, 2014.

[22] D. Rio Fernandes, F. Sievers, N. Kretzschmar, S. Wu, C. Salomon, and F. Chevy. Sub-doppler laser cooling of fermionic40k atoms in three-dimensional gray optical molasses. *EPL (Europhysics Letters)*, 100(6):63001, dec 2012.

[23] A. Burchianti, G. Valtolina, J. A. Seman, E. Pace, M. De Pas, M. Inguscio, M. Zaccanti, and G. Roati. Efficient all-optical production of largeLi6quantum gases usingD1gray-molasses cooling. *Physical Review A*, 90(4), oct 2014.

[24] C. L. Satter, S. Tan, and K. Dieckmann. Comparison of an efficient implementation of gray molasses to narrow-line cooling for the all-optical production of a lithium quantum gas. *Physical Review A*, 98(2), aug 2018.

[25] B. Lounis and C. Cohen-Tannoudji. Coherent population trapping and fano profiles. *Journal de Physique II*, 2(4):579–592, apr 1992.

[26] Rudolf Grimm, Matthias Weidemüller, and Yurii B. Ovchinnikov. Optical dipole traps for neutral atoms. 1999.

[27] Johannes Vrana. Towards atom-photon entanglement: State selective detection of a single atom, 2004.

[28] Anders H. Hansen, Alexander Y. Khramov, William H. Dowd, Alan O. Jamison, Benjamin Plotkin-Swing, Richard J. Roy, and Subhadeep Gupta. Production of quantum-degenerate mixtures of ytterbium and lithium with controllable interspecies overlap. *Physical Review A*, 87(1), jan 2013.

[29] Rianne S. Lous, Isabella Fritsche, Michael Jag, Bo Huang, and Rudolf Grimm. Thermometry of a deeply degenerate fermi gas with a bose-einstein condensate. *Physical Review A*, 95(5), may 2017.

[30] Yuqing Li, Guosheng Feng, Rundong Xu, Xiaofeng Wang, Jizhou Wu, Gang Chen, Xingcan Dai, Jie Ma, Liantuan Xiao, and Suotang Jia. Magnetic levitation for effective loading of cold cesium atoms in a crossed dipole trap. *Physical Review A*, 91(5), may 2015.

[31] A. Burchianti, C. D'Errico, S. Rosi, A. Simoni, M. Modugno, C. Fort, and F. Minardi. Dual-species bose-einstein condensate of k41 and rb87 in a hybrid trap. *Physical Review A*, 98(6), dec 2018.

[32] Christopher J. Foot. *Atomic Physics*. OXFORD UNIV PR, 2005.

[33] G. Salomon, L. Fouché, P. Wang, A. Aspect, P. Bouyer, and T. Bourdel. Gray-molasses cooling of39k to a high phase-space density. *EPL (Europhysics Letters)*, 104(6):63002, dec 2013.

[34] Tadas Pyragius. Developing and building an absorption imaging system for ultracold atoms. 2012.

[35] Wolfgang Ketterle and Martin W. Zwierlein. Making, probing and understanding ultracold fermi gases.

[36] W. Ketterle, D. S. Durfee, and D. M. Stamper-Kurn. Making, probing and understanding bose-einstein condensates.

[37] B. Naylor, A. Reigue, E. Maréchal, O. Gorceix, B. Laburthe-Tolra, and L. Vernac. Chromium dipolar fermi sea. *Physical Review A*, 91(1), jan 2015.

[38] Eric D. Black. An introduction to pound–drever–hall laser frequency stabilization. *American Journal of Physics*, 69(1):79–87, jan 2001.

[39] J. P. Gordon, R. C. C. Leite, R. S. Moore, S. P. S. Porto, and J. R. Whinnery. Long-transient effects in lasers with inserted liquid samples. *Journal of Applied Physics*, 36(1):3–8, jan 1965.

[40] S. J. Sheldon, L. V. Knight, and J. M. Thorne. Laser-induced thermal lens effect: a new theoretical model. *Applied Optics*, 21(9):1663, may 1982.

[41] Christina Bogan, Patrick Kwee, Stefan Hild, Sabina H. Huttner, and Benno Willke. Novel technique for thermal lens measurement in commonly used optical components. *Optics Express*, 23(12):15380, jun 2015.

[42] Sidney A. Self. Focusing of spherical gaussian beams. *Applied Optics*, 22(5):658, mar 1983.